Delft University of Technology

Lithospheric reflection imaging by multidimensional deconvolution of earthquake scattering coda

Hartstra, Iris

**Important note**
To cite this publication, please use the final published version (if applicable).
Please check the document version above.

# Lithospheric Reflection Imaging by Multidimensional Deconvolution of Earthquake Scattering Coda

# Lithospheric Reflection Imaging by Multidimensional Deconvolution of Earthquake Scattering Coda

**Proefschrift**

ter verkrijging van de graad van doctor

aan de Technische Universiteit Delft,

op gezag van de Rector Magnificus prof. dr. ir. T. H. J. J. van der Hagen,

voorzitter van het College voor Promoties,

in het openbaar te verdedigen op dinsdag 19 juni 2018 om 10.00 uur

door

**Iris Eline Hartstra**

Master of Science in Applied Earth Sciences, Technische Universiteit Delft,
the Netherlands
Master of Science in Applied Geophysics, ETH Zürich, Zwitserland
and RWTH Aachen, Germany

geboren te Seria, Brunei.

Dit proefschrift is goedgekeurd door de

promotor: prof. dr. ir. C. P. A. Wapenaar

Samenstelling promotiecommissie:

| | |
|---|---|
| Rector Magnificus, | voorzitter |
| Prof. dr. ir. C. P. A. Wapenaar | Technische Universiteit Delft, promotor |

*Onafhankelijke leden:*

| | |
|---|---|
| Prof. dr. J. O. A. Robertsson, | ETH Zürich |
| Prof. dr. J. A. Trampert, | Universiteit Utrecht |
| Prof. dr. W. A. Mulder, | Technische Universiteit Delft |
| Dr. ir. G. G. Drijkoningen, | Technische Universiteit Delft |
| Dr. I. Pires de Vasconcelos, | Universiteit Utrecht |
| Drs. A. Verdel, | TNO Utrecht |

The cover of this thesis was designed with `fdelmodc` and `Matlab`

# CONTENTS

# SUMMARY

Seismic interferometry (SI) for body waves offers the opportunity to utilize high-frequency scattering coda from local earthquakes to obtain a detailed reflectivity image of the lithosphere. In this thesis it is demonstrated that classical SI methods are seriously affected by circumstances that are typical of field data and that multiple scattering poses a complex trade-off for SI performance. Therefore, we propose an alternative method by multidimensional deconvolution (MDD) that proves to be more resilient under realistic circumstances and properly utilizes the scattering coda: full-field MDD. The main advantage of this method over classical MDD methods is that the kernel of its governing equation is exact, which allows for an optimal use of the multiple scattering coda to obtain virtual primary reflections of the lithosphere.

With a simple acoustic model of the lithosphere containing a discontinuous Moho boundary, it is demonstrated how SI by crosscorrelation, the original MDD method (ballistic MDD) and full-field MDD perform under full and limited illumination conditions. Different from crosscorrelation, the full-field MDD is not affected by the varying peak frequencies and orientations of the implemented passive sources nor by interferometric ghosts. Although ballistic MDD proves resilient against the varying passive source mechanisms, the accurate interpretation of the virtual reflection response is challenged by the interferometric ghost. The limited illumination experiment confirms that what the theory predicts: full-field MDD utilizes the illumination provided by the scattering coda in an effective way, while the other methods break down under these circumstances.

The elastic modeling regime is employed in order to implement quadrupole sources and investigate the resilience of the SI methods to the complexity caused by PS converted waves. The quadrupole radiation pattern simulates the effect of slip along fault-planes that generates the double-couple source mechanism typical of an earthquake hypocenter. In the elastic regime, MDD methods require a different formulation and an improved approximation of the required passive wavefield recording without free-surface multiples. We show that full-field MDD is significantly less sensitive to this required approximation than ballistic MDD. Additionally, we assess the performance in the elastic regime of the ANSI-MDD method: an adaptation of ballistic MDD that was originally developed for ambient-noise SI (ANSI). This method intrinsically differs from other MDD methods in that the point-spread

function (PSF) is extracted from the crosscorrelation gathers. We find that this posterior selection of the PSF necessitates a careful calibration and involves an instable inverse problem, which make this method relatively unreliable for field-data applications.

The elastic regime also paves the way for a more detailed analysis of the effect of multiple scattering on SI methods. The scattering radiation patterns are very different in the elastic domain, because the angle-dependent conversion between the P- and S-waves is complex. The numerical results show that when the passive sources provide a directly incident wavefield containing only high wavenumbers, crustal scatterers can help to improve the necessary low wavenumber illumination. However, multiple scattering also has a negative impact on the illumination of the array. Multiple scattering gives rise to certain wavefield complexities that imprint the virtual source radiation pattern, inevitably leading to artefacts. Crosscorrelation, ballistic MDD and ANSI-MDD hardly correct for these scattering-induced illumination irregularities. Since the kernel of full-field MDD encodes all scattering effects, the results show that this method still shows visible primaries under the strongest scattering conditions.

The scattering potential of the lithosphere can be estimated by determining the diffusivity of the medium by fitting the diffusion equation to the calculated average intensity in time. This makes it possible to assess the scattering properties of the medium as a function of frequency. On the one hand, a scattering analysis may allow to determine beforehand which SI method is likely to yield reliable results in a certain configuration. Moreover, by analyzing the changes in scattering potential as a function of frequency, it is possible to estimate the average size of the dominant heterogeneities that generate the observed scattering coda. The real data example is used to demonstrate this 'frequency-dependent scattering analysis'.

A common problem for body-wave interferometry is posed by the occurrence of surface waves in the data, that, if not handled correctly, will likely obscure the desired virtual reflections. The elastodynamic simulations include passive sources that generate surface waves, which manifest as virtual surface-waves in the results obtained by crosscorrelation and ANSI-MDD. Full-field MDD results do not show any sign of virtual surface waves, indicating that the surface waves are inherently removed. This is in accordance with the theory that dictates that full-field MDD obtains the reflection response without free surface and therefore also without surface waves.

Finally, real particle-velocity recordings from Peloponnesus, Greece, are used to demonstrate the applicability of elastodynamic full-field MDD and compare it to crosscorrelation. The results estimated with full-field MDD indicate specific features that are in accordance with previous studies of the area. These features are hardly visible in the crosscorrelation result. A synthetic experiment that simulates

the real data scenario confirms the difference in image quality between the two methods. It is concluded that full-field MDD proves to be an effective alternative to other SI methods that utilizes scattering coda in a physically correct way. When receiver coverage allows it, this method can yield a reliable high-resolution image of the lithosphere even under limited illumination conditions.

# Samenvatting

Seismische interferometrie (SI) maakt het mogelijk om een afbeelding met hoge resolutie van de ondergrond te verkrijgen door gebruik te maken van de natuurlijk aanwezige seismische volume golven. In deze thesis wordt geobserveerd dat bestaande SI methoden negatief beinvloed worden door omstandigheden die kenmerkend zijn voor echte data. Ook blijkt uit de resultaten van dit onderzoek dat meervoudige reflecties van het gemeten passieve seismische golfveld een tweestrijdig effect heeft op SI. Deze bevindingen vormen de voornaamste motivatie om een alternatieve SI methode te ontwikkelen: *full-field* multidimensionele deconvolutie (MDD). *Full-field* MDD blijkt aanzienlijk beter bestand tegen de natuurlijk omstandigheden in het veld en maakt op effectievere wijze gebruik van de verstrooiingscoda. Het belangrijkste voordeel van deze methode ten opzichte van de klassieke MDD methodes is dat de kernel van de vergelijking exact geformuleerd kan worden. Vanwege deze definitie van de kernel kan *full-field* MDD optimaal gebruik maken van de informatie die vergendeld is in de verstrooiingscoda om daarmee de gewenste virtuele primaire reflecties van de lithosfeer te construeren.

De verschillende SI methoden, SI d.m.v. kruiscorrelatie, conventionele MDD (hier aangeduid met 'ballistische MDD') en *full-field* MDD, worden met elkaar vergeleken met een eenvoudig akoestisch model van de lithosfeer, dat een discontinue Moho reflector bevat. Hierbij worden twee verschillende belichtingssituaties vergeleken: volledige belichting, waarbij de seismische bronnen de ontvangers vanuit voldoende hoeken belichten, en beperkte belichting, waarbij de seismische bronnen de ontvangers slechts vanuit de zijkanten belichten. Anders dan kruiscorrelatie, valt het op dat *full-field* MDD geen negatieve effecten ondervindt van de variërende piek frequenties en orientaties van de geïmplementeerde seismische bronnen en bovendien ook bestand is tegen de vervuiling van specifieke interferometrische artefacten die worden veroorzaakt door het neerwaarts passieve bronveld. Alhoewel ballistische MDD hetzelfde voordeel heeft als full-field MDD ten opzichte van de variërende specificaties van de passieve seismische bronnen, zijn de resultaten daarentegen wel vervuild door de hierboven beschreven interferometrische artefacten. Het experiment met beperkte belichting bevestigt wat de theorie voorspelt: *full-field* MDD maakt effectief gebruik van de meervoudige reflecties, terwijl de andere SI methoden onder deze omstandigheden tegenvallende resultaten geven.

Een vergelijkbaar experiment wordt vervolgens in het elastische domein uitgevoerd

om ook de effecten van PS conversies en van het complexe elastische quadrupool brontype op de verscheidene SI methoden te testen. De quadrupool is een benadering van het stralingspatroon van het seismische haardmechanisme welk door schuiving langs breukvlakken wordt veroorzaakt. In het elastische domein geldt een andere formulering van de MDD methodes en daarbij ook een meer geraffineerde benadering van het benodigde passieve golfveld dat zonder intereferenties van het vrije oppervlak. De resultaten laten zien dat *full-field* MDD significant minder gevoelig is voor afwijkingen in deze benadering dan ballistische MDD. Eveneens analyseren we de prestatie in het elastische domein van nog een MDD methode (hier aangeduid als ANSI-MDD) die oorspronkelijk was ontwikkeld om de MDD applicatie mogelijk te maken voor toepassingen met omgevingsruis data. ANSI-MDD verschilt wezenlijk van andere MDD methoden, omdat de benodigde virtuele bron functie (PSF) uit de kruiscorrelatie functies geselecteerd dient te worden. De resultaten van deze elastische experimenten laten zien dat ANSI-MDD sterk afhankelijk is van callibratie en dat de inversie van deze methode een stuk minder stabiel is vergeleken met de andere MDD methoden die we hier behandelen. Deze bevindingen maken de methode minder geschikt voor toepassingen met echte data.

Het elastische modelleringsdomein is daarnaast ook meer geschikt voor het testen van het effect van verstrooiing op de verschillende methodes. Wegens de complexe hoekafhankelijke conversie tussen P- en S-golven, zijn de stralingspatronen veroorzaakt door verstrooiing significant anders in het elastische domein dan in het akoestische domein. Deze verstrooiingsexperimenten laten zien dat in het geval van beperkte belichting, waarbij de passieve bronnen door hun positie alleen hoge golfgetallen leveren, de heterogeniteiten duidelijk de aanwezigheid van lage golfgetallen verbeteren. Desalniettemin laten de resultaten zien dat verstrooiing ook een negatieve impact heeft op de belichtingscondities, omdat het een complexe verstoring van het golfveld tot gevolg heeft. Deze verstoring kan leiden tot extra artefacten in het uiteindelijke resultaat, omdat het ook de virtuele bronfuncties negatief beïnvloed. Kruiscorrelatie, ballistische MDD en ANSI-MDD beschikken niet of nauwelijks over de mogelijkheid om voor dit negatieve effect van verstrooiing te corrigeren. Full-field MDD daarentegen presteert zelfs nog onder de sterkste verstrooiingscondities die hier getest zijn. Dit is te verklaren vanuit het feit dat de verstoringseffecten van verstrooiing zijn gecodeerd in de kernel van *full-field* MDD. Het verstrooiingspotentieel van de lithosfeer kan geschat worden door de frequentie-afhankelijke diffusiviteit van het medium te bepalen: door middel van een manuele curvenaanpassing van de diffusiviteitsvergelijking aan de gemiddelde intensiteitsverandering van de seismische tijdsregistratie is het mogelijk een schatting te krijgen van die diffusiviteit. Op deze wijze is het mogelijk om van te voren het verstrooiingspotentieel te bepalen en met die informatie te besluiten welke SI methode geschikt is voor de configuratie. Daarbij is het ook mogelijk door bij wijze

van een frequentie-afhankelijke verstrooiingsanalyse een schatting te maken van de gemiddelde afmeting van de dominante heterogeniteiten die de verstrooiing voor de gekozen frequentie genereren. We gebruiken een echt data voorbeeld om de potentie van deze 'frequentie-afhankelijke verstrooiingsanalyse' te demonstrerern.

Oppervlakte golven zijn een veelvoorkomend probleem voor volume-golf interferometrie. Wanneer geen extra stappen worden genomen kan hun aanwezigheid de gewenste virtuele reflecties flink maskeren. Dit effect is duidelijk zichtbaar in de elastische resultaten van kruiscorrelatie en ANSI-MDD, omdat de elastische experimenten passive bronnen bevatten die in de buurt van het oppervlak zitten. Echter, de elastische resultaten van *full-field* MDD bevatten geen teken van de aanwezigheid van oppervlakte golven. Dit impliceert dat de *full-field* MDD methode in staat is oppervlakte golven inherent te verwijderen. Dit is volledig in overeenstemming met de theorie die dicteert dat *full-field* MDD de reflectie responsie verkrijgt in het medium zonder vrij oppervlak.

Tot slot wordt gebruik gemaakt van deeltjessnelheidsregistaties van twee aardbevingen in Peloponnesus, Griekenland, om de echte data toepassing van elastische *full-field* MDD en kruiskorrelatie te vergelijken. Specifieke aspecten, die zichtbaar zijn in de resultaten verkregen met *full-field* MDD, zijn in overeenstemming met voorgaande seismische studies die in dit gebied zijn uitgevoerd. Echter, in de kruiscorrelatie resultaten zijn deze aspecten niet goed zichtbaar. De uitvoering van een synthetisch experiment dat dit scenario simuleert bevestigt dit verschil in kwaliteit tussen deze twee methoden. De resultaten in deze thesis leidt tot de conclusie dat de *full-field* MDD methode een goed alternatief is ten opzichte van conventionele SI methoden die effectief gebruik maakt van verstrooiingscoda op fysisch correcte wijze. Wanneer de bedekkingsgraad van ontvangers het toe laat, kan met deze methode een beeld van hoge resolutie verkregen worden. Zelfs wanneer de belichtingscondities beperkt zijn.

# 1

## INTRODUCTION

The lithosphere forms the most complex and heterogeneous layer of the Earth (Sato et al., 2012). It carries a long record of the geological processes that shaped this uppermost layer over the past billions of years. Though geological outcrops reveal more than one would expect at the first glance, crucial information is covered kilometers below the surface. Fortunately, seismic waves can take over to probe the subsurface structure where visible electromagnetic waves cannot continue.

A myriad of sources prevail that generate natural seismic waves: e.g. earthquakes, volcanic activity and oceanic microseisms. As this natural seismic wavefield propagates through the lithosphere, the higher-frequency waves interact with the heterogeneities by multiple scattering to generate a complex train of scattering coda that is ultimately recorded by seismographs employed at the surface. This coda is not random, in fact, the details of the lithospheric structure are encoded in it. Lithospheric images can be constructed by using the traveltime recordings of the natural seismic waves to estimate the propagation velocity. By tomographic inversion of the traveltimes between distant earthquakes and receivers, a smooth image of the subsurface structure can be estimated (Kennett, 1998, Nolet, 2008). Since traveltime tomography uses the first arrival of the wavefield, the higher frequency content of the seismic recordings is left unused, resulting in images that lack high resolution. This led to the development of full-wavefield inversion methods, that aim to resolve a model of the lithosphere that not only honors the first arrival, but the scattering coda as well (Bostock et al., 2001, Fichtner et al., 2010). However, these methods do rely on an accurate estimate of the location and timing of the earthquake that generated the coda. In this thesis we aim to develop methods that allow us to optimally decipher the complex lithospheric structure from natural scattering coda

**1**

without knowledge of the local earthquakes' location nor timing.

Seismic interferometry (SI) for body waves aims to transform scattering coda into a reflection response by transforming receivers into a virtual sources (Claerbout, 1968, Baskir & Weller, 1975, Schuster, 2001, Derode et al., 2003, Wapenaar, 2004, Snieder, 2004, Larose et al., 2006). Therewith, SI effectively redatums the natural passive source location to a receiver position of choice. This virtual source has the advantage over a natural earthquake source that its location and timing are known. When SI is effective, an array of receivers yields a complete virtual reflection survey that forms an input for controlled-source imaging techniques to generate subsurface images of high resolution and accuracy. However, in many cases SI by crosscorrelation is not suitable to yield a virtual reflection survey of acceptable quality.

The natural seismic illumination of the array typically has an anisotropic character. This causes the virtual source radiation pattern to be anisotropic as well, which leads to the appearance of artefacts in the crosscorrelation result that can obscure the virtual reflections. Earthquake source distributions usually are confined to active plate boundaries and fault zones. Therefore, earthquakes show a sparse and far from smooth distribution throughout the subsurface, which has a negative impact on the virtual source isotropy. Furthermore, earthquakes are caused by complex fault-slip mechanisms. The frequency, magnitude and P-S radiation can vary significantly between earthquake focal mechanisms, because these factors depend on the fault-geometry and mechanical properties of the surrounding rock (Stein & Wysession, 2003).

It is possible to estimate the radiation pattern of a virtual source and subsequently correct for it. One approach is to estimate the natural illumination of the array and use this information to apply appropriate weights such that the virtual source radiation becomes more isotropic (Curtis et al., 2009, Almagro Vidal et al., 2014). Alternatively, it is possible to select the radiation pattern with a time-window from the correlation gather, the so-called point-spread function (PSF), and subsequently deconvolve the same correlation gathers by their corresponding PSFs (van der Neut, 2012) . This method is one example of the group of methods that obtain the virtual reflections by the process known as multi-dimensional deconvolution (MDD), signifying that all receiver recordings are involved in the deconvolution simultaneously. Since the method was originally developed for ambient-noise seismic interferometry (ANSI), we refer to this specific form of MDD as ANSI-MDD throughout this thesis. The ANSI-MDD method does have some shortcomings in practice, which are primarily caused by the user-dependent selection procedure of the PSF from the correlation gathers and the relatively high instability of its inversion process.

Wapenaar et al. (2008b) introduced the original MDD method that is founded on the reciprocity theorem of the convolution type (de Hoop, 1995). Instead of estimating the PSF from the correlation gathers, this MDD method obtains an estimate of the PSF beforehand by approximating it with the directly incident wavefield from the natural earthquakes: the ballistic field. Due to its theoretical basis on convolution-type reciprocity relations, ballistic MDD inherently corrects for varying source radiation patterns, irregular source distributions and is also not affected by intrinsic attenuation. However, this method cannot make effective use of illumination provided by passive multiple scattering coda and, conversely, does not correct for irregularities that may be caused by this part of the recorded passive field. This is caused by the fact that the PSF is inexact: it is estimated by the ballistic field of the passive recordings. This also means that the method can only benefit of first order free-surface multiples that are initiated by the ballistic field to construct the desired virtual primaries. Since we are interested in utilizing all scattered events contained in the high-frequency scattering coda of local earthquakes, ballistic MDD method is not ideal for our purpose.

We propose to employ an alternative MDD method that is specifically designed to correctly utitilize the scattering coda: full-field MDD. Almagro Vidal (2017) introduced the original form of full-field MDD for one-way wavefields, and showed that this method obtains the reflection response of the medium without free surface and involves a more stable inversion than ballistic MDD. Though one-way wavefield decomposition has many advantages, it can also create artefacts when the medium varies laterally at the receiver level. Therefore, we develop the method here for two-way wavefield applications (Hartstra et al., 2017). The fundamental advantage of full-field MDD over other MDD methods is that the kernel of the equation no longer needs to be obtained by an approximation: the point-spread function (PSF) is constructed by the full earthquake recordings. This allows full-field MDD to utilize the entire scattering coda to yield the virtual reflection response. Unlike ballistic MDD, full-field MDD exploits free-surface multiples of all available orders in the scattering coda to construct the virtual primaries of all possible angles.

In Chapter 2 we compare SI by crosscorrelation, ballistic MDD and full-field MDD in the case of a full illumination and a limited illumination scenario by using acoustic numerical modelling (Thorbecke & Draganov, 2011). The limited illumination case allows to examine the performance of the methods when the scattering coda is the only source of illumination. We implement passive dipole sources with varying peak frequencies and orientations, and investigate the effect of random noise contamination on each of these methods. Here we also address the Achilles' heel of MDD methods: they require an estimate of the earthquake recordings without free-surface multiples. Unfortunately, MDD methods also have a weakness: they require

**1**

an estimate of the earthquake recordings without free-surface multiples. Since it is very challenging to remove free-surface multiples from earthquake recordings, we estimate this input by the direct wavefield instead (Wapenaar et al., 2008b). By extending the methods and the modeling to the elastic regime in Chapter 3, we are able to analyze the effect of the direct wave approximation when the passive recordings contain both direct P- and S-waves that are followed by scattering coda of P-SV conversions.

Especially in the case of local earthquakes, we can expect that the complex radiation patterns generated by the focal mechanisms of the passive sources will have a significant imprint on the virtual souce radiation pattern. The use of elastic models in Chapter 3 gives us the opportunity to implement a more realistic source type that simulates the effect of slip along a fault plane: the double-couple (Aki & Richards, 2002). In this chapter we simulate double-couple recordings in a 2D subduction zone model that is based on an actual geological setting of the Cascadia subduction zone (Chen et al., 2015). This allows us to evaluate the performance of crosscorrelation, ANSI-MDD, ballistic MDD and full-field MDD in a more realistic setting.

Sparse source illumination is one of the main problems that stand in the way for the successful practical application of SI. Previous studies have shown that in this case multiple scattering enhances the Green's function retrieval by crosscorrelation (Campillo & Paul, 2003, Derode et al., 2003, van Tiggelen, 2003, Larose et al., 2004b, Malcolm et al., 2004). However, scattering also increases the complexity of the wavefield that increases the likelihood of artefacts to manifest in the interferometry results (Hartstra & Wapenaar, 2015).

Furthermore, scattering poses an ambiguous case for the MDD methods as well, because a higher scattering potential implies that the direct-wave approximation of the passive recording without free-surface multiples becomes less reliable. These considerations generated the motivation to investigate the effect of the scattering potential on the performance of the SI methods in the case of limited illumination in Chapter 4. Since P-S conversions play an important role in the multiple scattering regime (Snieder, 2002), we generate elastodynamic recordings due to passive sources that generate both P- and S-waves. This analysis serves to explain the apparent trade-off between scattering potential and the performance of each different SI method.

Finally, a field data application is considered by using an array that was part of the MEDUSA project in Peloponnesus, Greece (Suckale et al., 2009). Crosscorrelation is the most tried method in the case of field data applications concerning body-wave retrieval. This includes ambient-noise applications (Roux et al., 2005, Draganov et al., 2007, Nishida, 2013, Lin et al., 2013, Boué et al., 2014) and local earthquake

scattering coda applications (Tonegawa et al., 2009, Almagro Vidal, 2017, Ruigrok, 2012). The ANSI-MDD method was applied to P-wave scattering coda recorded by the Mallargue array (Nishitsuji et al., 2016). Nakata et al. (2014) estimated virtual body-wave reflections with ballistic MDD for one-way wavefields. In Chapter 5 we demonstrate the first real data example to obtain body-wave reflections by using full-field MDD for two-way wavefields. We complement the real data results with a synthetic example using a model and configuration that aims to simulate the real case scenario.

# 2

# FULL-FIELD MULTIDIMENSIONAL DECONVOLUTION TO RETRIEVE BODY-WAVE REFLECTIONS FROM SPARSE PASSIVE SOURCES

*Our objective is to complement lithospheric seismic tomography with an interferometric method to retrieve high-resolution reflectivity images from local earthquake recordings. The disadvantage of using local earthquakes for the retrieval of reflected body-waves is their usual sparse distribution. We propose an alternative formulation of passive seismic interferometry by multidimensional deconvolution (MDD) which uses the multiples in the full recordings to compensate for missing illumination angles. This method only requires particle-velocity recordings at the surface from passive transient sources and retrieves body-wave reflection responses without free-surface multiples. We conduct an acoustic modelling experiment to compare this formulation to a previous MDD method and Green's function retrieval by crosscorrelation for different source distributions. We find that in the case of noise-contaminated recordings obtained under severely limited and irregular illumination conditions, the alternative MDD method introduced here still retrieves the complete reflection response without free-surface multiples where the other inter-*

*ferometric methods break down.*

**2**

## 2.1. INTRODUCTION

Seismic tomography is used extensively to obtain information about the complex low-frequency structures of the lithosphere (Nolet, 2008). Reflection imaging could complement tomography by providing a well-constrained image of impedance contrasts with a high spatial resolution. A densely sampled reflection survey with controlled high-frequency sources placed at the surface could yield this desired image. However, conducting this type of survey at a lithospheric scale is very expensive and invasive for the natural environment.

Seismic interferometry (SI) represents a set of less expensive and noninvasive methods that can be applied to a regular and densely sampled receiver array at the surface to retrieve virtual body-wave reflection responses from passive recordings (Schuster, 2009). These methods have the potential to give accurate results when specific requirements are met. For example, they rely on sufficient and isotropic illumination by naturally occurring seismic sources. Local earthquakes have the potential to provide waves with high-frequency content. However, the range of illumination angles provided by these sources strongly depends on their relative position and orientation to the imaging target and the receiver array. Multiple reflections could compensate for the missing illumination angles, but the currently employed SI methods are not designed to utilize higher order scattering events in a physically correct way to construct body-wave reflections.

SI by crosscorrelation retrieves any type of Green's function response between two receivers, by effectively turning one of the receivers into a virtual source. In practice, this method has proven to yield body-wave reflections under specific circumstances (Draganov et al., 2007, Tonegawa et al., 2009, Poli et al., 2012, Boué et al., 2014). However, there are several drawbacks to consider when using crosscorrelation for the retrieval of body waves. First of all, the method requires a well-sampled boundary of passive sources to enclose the receiver array. In addition, the source mechanisms and radiation patterns should ideally be the same for all passive sources. Violation of these requirements leads to irregular illumination of the array, which in turn causes the radiation patterns of the virtual sources to be anisotropic. This inevitably leaves its imprint on the retrieved reflection responses by causing inaccurate reconstruction of amplitudes as well as a less effective destructive inter-

ference of artifacts. Finally, SI by crosscorrelation assumes the input wavefields to be reversible in time, which only holds in lossless media. This implies that for the case of field data the reliability of this method is compromised since it is unlikely that all these conditions are met.

Multidimensional deconvolution (MDD) offers an alternative to crosscorrelation for retrieving reflection responses from passive recordings (Wapenaar et al., 2008b). This method does not rely on time-reversibility, because it is based on reciprocity relations of the convolution type. Intuitively, MDD can be compared to a 'deblurring' procedure whereby artifacts caused by anisotropic illumination or variations in passive-source mechanisms are corrected for by deconvolving with a 'point-spread function' (PSF). This PSF is constructed from the wavefields of the kernel in the original reciprocity formulation and ideally contains spectral information of the virtual-source radiation patterns (van der Neut, 2012). The kernel of the reciprocity formulation of the MDD method described in Wapenaar et al. (2008b) is, in theory, composed of the direct wave and the internal multiples from the recorded wavefield. However, when the subsurface reflectivity is unknown, it is in practice only feasible to extract the direct wave (which can include possible short-period multiples) from the recordings, because separating internal multiples from surface-related multiples is not a trivial task. The resulting approximation of the kernel limits the PSF to wavenumbers provided by the directly incident field: the 'ballistic field' (Nakata et al., 2014). Inverting this ballistic PSF likely produces errors, because the function is inexact and affected by time-window procedures. These disadvantages are expected to be most apparent when the passive-source illumination from approximately vertically below the receiver array is absent and the retrieval of virtual reflections relies on low-wavenumber illumination from scattered events in the passive coda wavefield. In such a case, a purely ballistic PSF does not suffice to compensate for irregularities in the virtual-source radiation patterns. In fact, the PSF would require spectral information of the coda wavefield as well in order to enable the appropriate illumination balancing and thus enhance the sought-after virtual reflection responses.

The need for a more extensive PSF led to the development of an alternative reciprocity relation which contains an exact full-field kernel, instead of an approximated ballistic one (Almagro Vidal, 2017). Here, the term 'full-field' indicates that the kernel consists of the entire recorded passive wavefield containing both the ballistic and coda field. The full-field MDD method thus conducts the 'deblurring' operation using a full-field PSF, which has encoded the maximum available spectral information to correct the virtual-source radiation patterns. Consequently, in cases when the retrieval of virtual reflections relies primarily on illumination from

the passive coda field, this full-field PSF is expected to perform better than the ballistic PSF. Moreover, the full-field PSF avoids inversion of an approximated and time-windowed function (as is the case in ballistic MDD).

In order to validate the above-mentioned advantages of full-field MDD over ballistic MDD and crosscorrelation, we conduct an effective comparison of these SI methods. The experiments are carried out using acoustic synthetic data, which allows for a controlled analysis of the performance of each of these methods under various passive-source illumination conditions as well as noise contamination.

## 2.2. Methods

In Wapenaar et al. (2011), a systematic comparison is given of SI methods, including ballistic MDD and crosscorrelation, for retrieving the reflection response from active and passive-source recordings. The passive SI methods are addressed for the case of transient-source recordings as well as for ambient noise recordings, which requires an adapted form in the case of the MDD application (van der Neut, 2012). Here we focus only on the passive transient-source scenario, because this corresponds to earthquake recordings. We review the theory of ballistic MDD and crosscorrelation and introduce our new formulation for retrieving multicomponent reflection responses at the free surface.

### 2.2.1. Ballistic MDD

We formulate the reciprocity relation of the convolution type for a passive transient-source configuration to study the interaction quantities of wavefields in two independent states, A and B (Wapenaar et al., 2008b). The respective wavefields in each state are considered in the same arbitrary inhomogeneous anisotropic dissipative medium in which we define a domain $\mathbb{D}$ enclosed by a boundary $\partial\mathbb{D}$. We divide boundary $\partial\mathbb{D}$ into a horizontal part at the level of the acquisition array, defined by the receiver positions $\mathbf{x}_R \in \partial\mathbb{D}_R$, and an arbitrarily shaped part $\partial\mathbb{D}_M$ inside the medium (Figure 2.1). Boundary $\partial\mathbb{D}_M$ has absorbing boundary conditions in both states A and B, while the boundary conditions of $\partial\mathbb{D}_R$ differ between states. The measurement state A represents the actual medium in which the passive wavefields can be recorded. This medium contains a free surface at the level of the acquisition array. Instead of a free surface, state B has absorbing boundary conditions at $\partial\mathbb{D}_R$. Hence, inside reference state B, fields do not have free-surface interaction and are denoted by the superscript '$o$'. Sources in state A are introduced immediately below the boundary $\partial\mathbb{D}_R$ at positions $\mathbf{x}_A$. However, by invoking source-receiver reciprocity, sources at $\mathbf{x}_A$ function as receivers. In state B the source locations, $\mathbf{x}_B$,
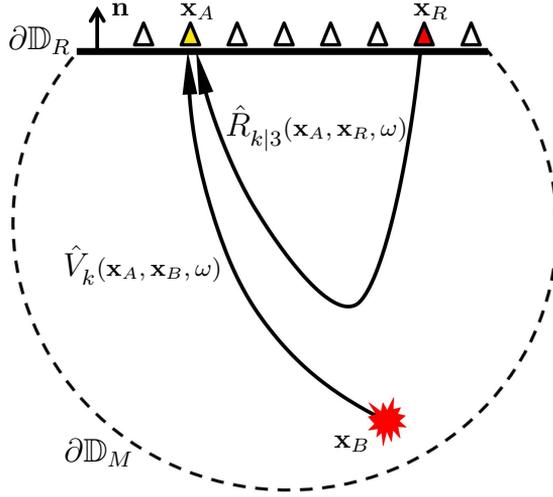
(a) State A
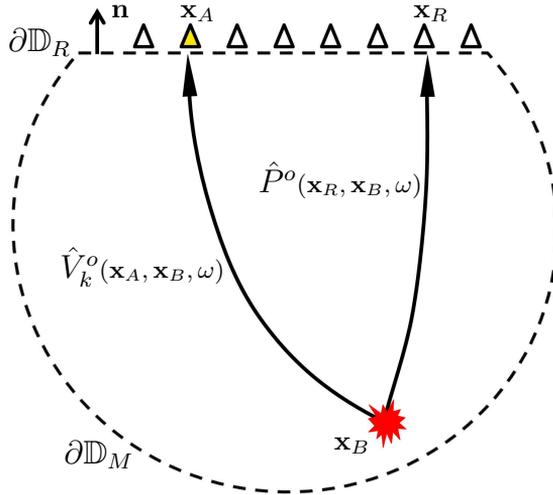


(b) State B

Figure 2.1: *State definitions for ballistic MDD. (a) State A in the medium with free surface: the boundary of the domain, $\partial\mathbb{D}$, consists of a half-sphere, $\partial\mathbb{D}_M$, with infinite radius and a horizontal free surface (thick continuous line), $\partial\mathbb{D}_R$, with normal vector $\mathbf{n}$. The receivers at boundary $\partial\mathbb{D}_R$ are denoted by triangles: red indicates the position of the virtual source and yellow its corresponding receiver. $\hat{R}_{k|3}(\mathbf{x}_A,\mathbf{x}_R)$ is the reflection response at $\mathbf{x}_A$ to a virtual vertical traction source at $\mathbf{x}_R$ and contains free-surface multiples. $\hat{V}_k(\mathbf{x}_A,\mathbf{x}_B,\omega)$ is the particle-velocity response at receiver position $\mathbf{x}_A$ due to an arbitrary passive source at $\mathbf{x}_B$ (red star) and contains free-surface multiples. (b) State B in the medium without free surface: here the acquisition boundary $\partial\mathbb{D}_R$ has absorbing boundary conditions (dotted line). $\hat{P}^o(\mathbf{x}_R,\mathbf{x}_B,\omega)$ and $\hat{V}_k^o(\mathbf{x}_A,\mathbf{x}_B,\omega)$ are the pressure response at $\mathbf{x}_R$ and particle-velocity response at $\mathbf{x}_A$, respectively, due to an arbitrary passive source at $\mathbf{x}_B$ (red star).*

are anywhere inside the domain. Using these state definitions, the reciprocity theorem of the convolution type for acoustic wavefields in 3D media yields a Fredholm integral of the first kind:

$$\int_{\partial \mathbb{D}_R} \hat{R}_{k|3}(\mathbf{x}_A, \mathbf{x}_R, \omega) \hat{P}^o(\mathbf{x}_R, \mathbf{x}_B, \omega) d^2 \mathbf{x}_R = \hat{V}_k^o(\mathbf{x}_A, \mathbf{x}_B, \omega) - \hat{V}_k(\mathbf{x}_A, \mathbf{x}_B, \omega). \qquad (2.1)$$

This relation is expressed in the space-frequency domain, where $\omega$ denotes the angular frequency. $\hat{R}_{k|3}(\mathbf{x}_A, \mathbf{x}_R, \omega)$ is the desired impulsive particle-velocity reflection response at $\mathbf{x}_A$ caused by a vertical-traction source at $\mathbf{x}_R$ at the free surface. This response is defined in the measurement state A with free surface and therefore contains free-surface multiples. The lower-case subscript on the left side of the vertical bar, with possible values 1, 2 or 3, denotes the receiver component of the field, while the subscript on the right side denotes the component of the virtual source. The kernel of the Fredholm integral, $\hat{P}^o(\mathbf{x}_R, \mathbf{x}_B, \omega)$, is the passive pressure-field response at $\mathbf{x}_R$ due to a source at $\mathbf{x}_B$ in the reference state without free surface. $\hat{V}_k(\mathbf{x}_A, \mathbf{x}_B, \omega)$ and $\hat{V}_k^o(\mathbf{x}_A, \mathbf{x}_B, \omega)$ represent the passive particle-velocity responses for the situation with and without free surface, respectively, at $\mathbf{x}_A$ due to a source at $\mathbf{x}_B$. The source at $\mathbf{x}_B$ does not require a subscript, because the relation holds for any kind of source mechanism. Note that $\hat{V}_k(\mathbf{x}_A, \mathbf{x}_B, \omega)$ represents the actual measurements, from which $\hat{V}_k^o(\mathbf{x}_A, \mathbf{x}_B, \omega)$ and the kernel, $\hat{P}^o(\mathbf{x}_R, \mathbf{x}_B, \omega)$, need to be extracted. The integral boundary is defined by the receiver positions of the passive measurements at the horizontal acquisition level $\partial \mathbb{D}_R$. We let the remaining part of the closed boundary, $\partial \mathbb{D}_M$, extend to infinity such that its contribution to the integral vanishes due to Sommerfeld's radiation condition. Note that the multiplication inside the integrand represents a convolution in the time domain. In order to solve for the reflection response, $\hat{R}_{k|3}(\mathbf{x}_A, \mathbf{x}_R, \omega)$, we need to invert equation (2.1). However, in case we only have the recordings of a single passive source in a 2D or 3D medium, this inverse problem is severely ill-posed (Arfken & Weber, 2005). We can constrain the problem by taking into account many passive source recordings. Employing the wavefield matrix notation (Berkhout, 1982), equation (2.1) becomes:

$$\hat{\mathbf{R}}_{k|3} \hat{\mathbf{P}}^o = \hat{\mathbf{V}}_k^o - \hat{\mathbf{V}}_k, \qquad (2.2)$$

where boldface symbolizes the matrix form of the wavefields. A field matrix ($\hat{\mathbf{P}}^o$, $\hat{\mathbf{V}}_k^o$ and $\hat{\mathbf{V}}_k$) contains the independent non-overlapping recordings of passive sources, whereby each row represents a receiver position and each column a passive source in the subsurface. The reflection response $\hat{\mathbf{R}}_{k|3}$ is similar, except that it is a square matrix and its columns correspond to independent virtual sources at the surface. The

normal form (van der Neut et al., 2011) of equation (2.2) for the particle-velocity reflection response is given by:

$$\hat{\mathbf{R}}_{k|3}\hat{\mathbf{P}}^o\hat{\mathbf{P}}^{o\dagger} = \left(\hat{\mathbf{V}}_k^o - \hat{\mathbf{V}}_k\right)\hat{\mathbf{P}}^{o\dagger}, \tag{2.3}$$

where $^\dagger$ denotes transposition and complex conjugation. To solve for the unknown reflection response we implement regularized least-squares inversion:

$$\hat{\mathbf{R}}_{k|3} = \left[\left(\hat{\mathbf{V}}_k^o - \hat{\mathbf{V}}_k\right)\hat{\mathbf{P}}^{o\dagger}\right]\left[\hat{\mathbf{P}}^o\hat{\mathbf{P}}^{o\dagger} + \epsilon^2\mathbf{I}\right]^{-1}, \tag{2.4}$$

where the first term in square brackets on the right-hand side represents the 'correlation function', while the second term in square brackets is the inverse matrix: it contains the 'point-spread function' (PSF) and the regularization matrix, which is composed of a stabilization parameter, $\epsilon^2$, and the identity matrix $\mathbf{I}$ (van der Neut, 2012). This operation represents a multidimensional deconvolution (MDD), which implies that the reflection response is retrieved for all virtual sources and receivers simultaneously. This makes MDD distinctly different from Green's function retrieval by crosscorrelation, which obtains the response independently for each virtual-source position. The reference-state fields without free-surface interaction, $\hat{\mathbf{P}}^o$ and $\hat{\mathbf{V}}_k^o$, could be obtained by removing all surface-related multiples from the passive recordings, but in practice this is an extremely challenging procedure. Therefore, we estimate the field $\hat{\mathbf{V}}_k^o$ by extracting the only event we can distinguish from other events with considerable certainty: the direct arrival of the passive recording $\hat{\mathbf{V}}_k$ (which can include possible short-period multiples). We multiply the direct arrival by a factor $\frac{1}{2}$ to account for the absence of the free surface in the reference state. This estimate is quite reliable for the implementation of MDD when the medium is weakly scattering. Since measurements are usually obtained at the free surface, $\hat{\mathbf{P}}^o$ can be estimated from the vertical particle-velocity recordings by an additional far-field approximation: $\hat{P}^o \approx -\rho c \hat{V}_3^o$, where $\rho$ and $c$ are the mass density and P-wave velocity, respectively, at the receiver locations. Equation (2.4) thus becomes:

$$\hat{\mathbf{R}}_{k|3} \approx \frac{1}{\rho c}\left[\left(\hat{\mathbf{V}}_k - \hat{\mathbf{V}}_k^D\right)\hat{\mathbf{V}}_3^{D\dagger}\right]\left[\hat{\mathbf{V}}_3^D\hat{\mathbf{V}}_3^{D\dagger} + \epsilon^2\mathbf{I}\right]^{-1}, \tag{2.5}$$

where the superscript '$D$' indicates that the wavefield is the direct wave of the particle-velocity recording multiplied by the factor $\frac{1}{2}$. Note that the $\epsilon$ in this equation is a scaled version of the $\epsilon$ in equation (2.4). The direct-wave approximation

will cause errors in both the correlation function and the inverse matrix, which inevitably propagate into the solution $\hat{\mathbf{R}}_{k|3}$. Physically speaking, this approximation means that the PSF in the inverse matrix, $\hat{\mathbf{V}}_3^D \hat{\mathbf{V}}_3^{D\dagger}$, is now only constructed by the direct incident wavefield of the passive particle-velocity recordings: the ballistic wavefield. This is why we have designated this MDD method as 'ballistic MDD'. The fact that the PSF is estimated by ballistic wavefields limits this MDD method to use only the wavenumbers provided directly by the passive-source distribution. Moreover, the ballistic PSF can only correct for anisotropy in the virtual-source radiation patterns caused by irregular source distributions and mechanisms, but not for anisotropy resulting from scattering inside the medium.

An approximation to the reflection response $\hat{R}_{k|3}$ can alternatively be obtained from the reciprocity relation of the correlation type, as presented in Wapenaar & Fokkema (2006):

$$\Re\left[\hat{R}_{k|3}(\mathbf{x}_A, \mathbf{x}_R, \omega)\right] \langle \hat{S}(\omega) \rangle \approx \int_{\partial \mathbb{D}_S} \rho(\mathbf{x}_B) c(\mathbf{x}_B) \hat{V}_3^*(\mathbf{x}_R, \mathbf{x}_B, \omega) \hat{V}_k(\mathbf{x}_A, \mathbf{x}_B, \omega) d^2\mathbf{x}_B. \quad (2.6)$$

The integral is along the distribution of passive sources at locations $\mathbf{x}_B \in \partial \mathbb{D}_S$ in the subsurface, where $\rho(\mathbf{x}_B)$ and $c(\mathbf{x}_B)$ denote the mass density and P-wave velocity of the medium, respectively, at these same locations. $\hat{V}_3(\mathbf{x}_R, \mathbf{x}_B, \omega)$ and $\hat{V}_k(\mathbf{x}_A, \mathbf{x}_B, \omega)$ are particle-velocity recordings at receiver positions $\mathbf{x}_R$ and $\mathbf{x}_A$, respectively, due to a passive source at $\mathbf{x}_B$. Note that superscript '$*$' denotes complex conjugation, which implies that the integrand product represents a crosscorrelation in the time-domain. The left-hand side denotes the causal and the acausal impulsive particle-velocity reflection response at receiver $\mathbf{x}_A$ due to a vertical-traction source at $\mathbf{x}_R$. $\langle \hat{S}(\omega) \rangle$ is the average power spectrum of the passive sources. Although equation (2.6) retrieves the same response as equation (2.1), their underlying solution methods differ significantly. Equation (2.6) is solved explicitly, which explains the relative robustness of the method. However, due to the formulation of the integral, it does require a well-sampled enclosing boundary of passive sources: a condition unlikely to be met by earthquake sources, which are generally sparse. Equation (2.1) is implicit and hence requires inversion. However, a concomitant advantage of inversion is that it corrects for the imprint of the irregular passive-source illumination. Moreover, since the integral of equation (2.1) is along the positions of the receivers instead of the passive sources, it still works when the source distribution is sparse, as long as the receivers form a well-sampled and sufficiently extended array.
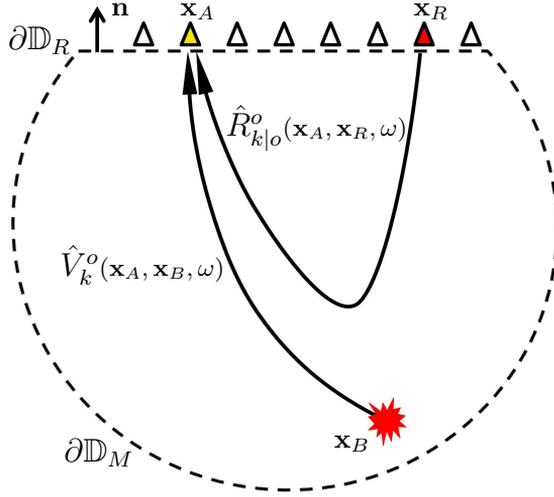
(a) State A
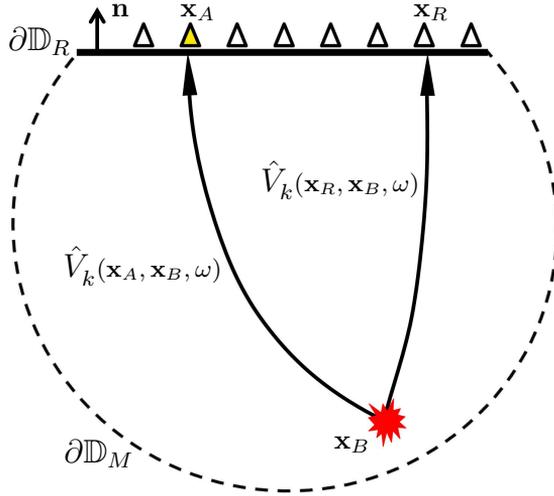


(b) State B

Figure 2.2: *State definitions for full-field MDD. (**a**) State A in the medium without free surface: the boundary of the domain, $\partial\mathbb{D}$, consists of a half-sphere, $\partial\mathbb{D}_M$, with infinite radius and a horizontal surface, $\partial\mathbb{D}_R$, with normal vector $\mathbf{n}$. The receivers at boundary $\partial\mathbb{D}_R$ are denoted by triangles: red indicates the position of the virtual source and yellow its corresponding receiver. $\hat{R}^o_{k|0}(\mathbf{x}_A, \mathbf{x}_R, \omega)$ is the reflection response at $\mathbf{x}_A$ to a monopole virtual source at $\mathbf{x}_R$ and is without free-surface multiples. $\hat{V}^o_k(\mathbf{x}_A, \mathbf{x}_B, \omega)$ is the particle-velocity response at receiver position $\mathbf{x}_A$ due to an arbitrary passive source at $\mathbf{x}_B$ (red star) without free-surface multiples. (**b**) State B in the medium with free surface: here the acquisition boundary $\partial\mathbb{D}_R$ forms a free surface (thick continuous line). $\hat{V}_k(\mathbf{x}_R, \mathbf{x}_B, \omega)$ and $\hat{V}_k(\mathbf{x}_A, \mathbf{x}_B, \omega)$ are the particle-velocity responses with free-surface multiples at $\mathbf{x}_R$ and $\mathbf{x}_A$, respectively, due to an arbitrary passive source at $\mathbf{x}_B$ (red star).*

### 2.2.2. FULL-FIELD MDD

We now introduce our formulation for the alternative MDD method, which uses both the ballistic and coda (or scattered) wavefield of the data: the full field. We use the same setting as for ballistic MDD, but we change the boundary conditions: we appoint state B as the measurement state with free surface, while state A is the reference state without free surface (denoted by superscript '$o$') of which we aim to determine the reflection response (Figure 2.2). This switch of the boundary conditions at $\partial \mathbb{D}_R$ between states ensures that the kernel now contains the measured data (which avoids the need to extract the direct wave to build the kernel) and allows us to retrieve a reflection response without free-surface multiples. Note that the source locations $\mathbf{x}_A$ and $\mathbf{x}_B$ remain the same as for ballistic MDD. The acoustic representation in 3D media is presented in the space-frequency domain as:

$$\int_{\partial \mathbb{D}_R} \hat{R}^o_{k|0}(\mathbf{x}_A, \mathbf{x}_R, \omega) \hat{V}_3(\mathbf{x}_R, \mathbf{x}_B, \omega) d^2\mathbf{x}_R = \hat{V}_k(\mathbf{x}_A, \mathbf{x}_B, \omega) - \hat{V}^o_k(\mathbf{x}_A, \mathbf{x}_B, \omega). \quad (2.7)$$

For the derivation in elastic 3D media, refer to Appendix A. Note that in this formulation the unknown particle-velocity reflection response $\hat{R}^o_{k|0}$ is caused by a monopole source and does not contain free-surface multiples. The monopole source is indicated by subscript zero '0', because it is a scalar. The kernel, $\hat{V}_3(\mathbf{x}_R, \mathbf{x}_B, \omega)$, is the full recording of the vertical particle-velocity at receiver $\mathbf{x}_R$ at the free surface of the actual medium due to an arbitrary passive source at $\mathbf{x}_B$. The source type, signature and location of the passive sources at $\mathbf{x}_B$ do not need to be known. Similar to equation (2.1), this equation is a Fredholm integral of the first kind, but with a different solution $\hat{R}^o_{k|0}(\mathbf{x}_A, \mathbf{x}_R, \omega)$ and a kernel which does not require approximations. Equation (2.7) presents an inverse problem, which also requires to be constrained by considering many passive source recordings. We express equation (2.7) using wavefield matrix notation:

$$\hat{\mathbf{R}}^o_{k|0} \hat{\mathbf{V}}_3 = \hat{\mathbf{V}}_k - \hat{\mathbf{V}}^o_k. \quad (2.8)$$

The normal form of equation (2.8) for the particle-velocity reflection response is given by:

$$\hat{\mathbf{R}}^o_{k|0} \hat{\mathbf{V}}_3 \hat{\mathbf{V}}^\dagger_3 = \left(\hat{\mathbf{V}}_k - \hat{\mathbf{V}}^o_k\right) \hat{\mathbf{V}}^\dagger_3, \quad (2.9)$$

and we solve by regularized least-squares:

$$\hat{\mathbf{R}}^o_{k|0} = \left[ (\hat{\mathbf{V}}_k - \hat{\mathbf{V}}^o_k)\hat{\mathbf{V}}^\dagger_3 \right] \left[ \hat{\mathbf{V}}_3\hat{\mathbf{V}}^\dagger_3 + \epsilon^2\mathbf{I} \right]^{-1}. \tag{2.10}$$

Note that in this case, the evaluation of the PSF in the regularized inverse matrix does not require any approximations: it is constructed by the full recordings of the particle-velocity response of the medium. Hence, we refer to this MDD method as 'full-field MDD'. The term 'full-field' originates from the fact that the PSF is constructed by the full passive recordings, containing both the ballistic and the coda wavefields. Note that this means that this MDD effectively uses the wavenumbers provided by the ballistic as well as all scattered events in the data (this includes the free-surface multiples). Therefore, this full-field PSF also corrects for anisotropic illumination caused by both the ballistic field and the scattering inside the medium.

In order to solve for the reflection response in equation (2.10), $\hat{\mathbf{V}}^o_k$ in the right-hand side needs to be estimated in the same way as we did for equation (2.5): by extracting the direct field from each passive recording and multiply by a factor $\frac{1}{2}$. However, we do not require the additional far-field approximation here. The equation thus becomes:

$$\hat{\mathbf{R}}^o_{k|0} \approx \left[ (\hat{\mathbf{V}}_k - \hat{\mathbf{V}}^D_k)\hat{\mathbf{V}}^\dagger_3 \right] \left[ \hat{\mathbf{V}}_3\hat{\mathbf{V}}^\dagger_3 + \epsilon^2\mathbf{I} \right]^{-1}. \tag{2.11}$$

It is important to remark that in the case of full-field MDD the direct-wave approximation only occurs in the correlation function. The wavefields in the PSF however, do not require any approximations.

We have discussed two essentially different MDD methods. Ballistic MDD retrieves the reflection response with free-surface multiples, while full-field MDD retrieves the response without free-surface multiples. The kernel of the latter is constructed by the full passive data and thus governs a wide spectrum of wavenumbers, while the kernel of the former is limited to the wavenumbers of the passive ballistic field. As a consequence, the full-field PSF takes into account additional wavenumber illumination provided by the recorded scattered field and consequently corrects for the irregular illumination it may cause. These points lead us to hypothesize that full-field MDD applies a better constrained inversion and yields a more accurate retrieval of the reflection response than ballistic MDD. Nevertheless, we still expect the retrieval of the reflection response to be contaminated by some artifacts, since the correlation function of full-field MDD does contain the approximated $\hat{\mathbf{V}}^D_k$ field.

## 2.3. NUMERICAL RESULTS

We conduct an effective comparison of retrieving the particle-velocity reflection response by crosscorrelation (equation (2.6)), ballistic MDD (equation (2.5)) and full-field MDD (equation (2.11)). Here we choose to analyze only the vertical-component particle-velocity reflection response by setting subscript $k$ to 3, but we emphasize that we can equally well obtain the horizontal components when the input data provides them. To simulate the input recordings, we perform independent 2D numerical experiments using acoustic finite-difference wavefield simulation (Thorbecke & Draganov, 2011).

We use a lithospheric model with a Moho reflector at 50 km depth with a discontinuity, which is characterized by a downward vertical displacement of 10 km (Figure 2.3a). The P-wave velocities of the crust and upper mantle are 6 km s$^{-1}$ and 9 km s$^{-1}$, respectively, and the respective densities are 2700 kg m$^{-3}$ and 3400 kg m$^{-3}$ (Dziewonski & Anderson, 1981). We generate independent passive recordings by modelling dipole sources which we orient approximately tangential to the alignment of the source locations, with some random directional deviation. This has the purpose to approximate the effect of slip occurring along an irregular listric fault system. For each passive-source signature we use a different Ricker wavelet with a peak frequency varying between 0.3 and 1.1 Hz. In Figure 2.3a, the orientation and location of the passive dipole sources are indicated by arrows: the color defines their peak frequency. The 200 multi-component receivers are placed 0.2 km beneath the free surface with an inter-receiver spacing of 1 km. However, the receivers can be considered to be approximately at the free-surface level, because 0.2 km is less than 4% of the smallest central wavelength in the upper layer. We model the passive recordings for a total time of 170 seconds to ensure that free-surface multiples of higher orders are present in the data. The experiment is conducted for the comparison of two different irregular source distributions: the first provides full coverage (Figure 2.3a), while the second provides only limited illumination from the sides (Figure 2.4a).

### 2.3.1. COMPLETE ILLUMINATION

We use the three interferometric methods to retrieve a reflection response to a virtual source at the position of the middle receiver (position 0 km) for the case of sufficient passive-source illumination (Figure 2.3). To enable a visual analysis of the quality of the retrieved reflection responses, we directly model the reflection response by placing a monopole source at the position of the middle receiver with a peak frequency of 1.1 Hz, depicted in Figure 2.3b. This modelled response is characterized by four distinct events: the direct wave, the primary Moho reflection,

the diffraction of the Moho discontinuity and the first free-surface multiple reflection. We focus on the body-wave reflections: the primary and the first free-surface multiple, which at position 0 km have two-way traveltimes of approximately 17 and 34 seconds, respectively. The visible jump in the body-wave reflections and the corresponding diffractions are caused by the Moho discontinuity.

We first compare the reflection retrieved by crosscorrelation in Figure 2.3c to the modelled response in Figure 2.3b. The resolution of the crosscorrelation result is significantly lower, which makes it difficult to distinguish the primary or the free-surface multiple reflection. This low resolution is caused by the variation in spectra between individual passive sources. In spite of the low resolution, the primary reflection can be distinguished at positions -100 to -50 km and 50 to 100 km. Between positions -50 and 50 km, the primary reflection becomes more obscured by the presence of artifacts, which makes it difficult to detect the Moho discontinuity. The artifacts are a result of the anisotropic illumination of the array due to the variations in passive-source radiation patterns.

The result of ballistic MDD is shown in Figure 2.3d. The resolution of this reflection retrieval is comparable to the modelled response in Figure 2.3b. The primary is retrieved for each receiver position and it is possible to detect the jump caused by the Moho discontinuity. However, the primary is not very distinct, because its amplitude is not significantly higher than most of the artifacts. At about 4 seconds after the primary an erroneous 'ghost' of the primary is clearly visible, which, in the realistic case when the medium parameters are not known, could result in an incorrect interpretation of a reflectivity contrast. This interferometric ghost is caused by crosscorrelations between direct waves and primaries in the correlation function. The ballistic PSF cannot correct for this, because it only contains the spectral information of the direct waves (see Figure 2.5a). In addition to this predominant artifact, the retrieved primary reflection is slightly obscured by steep-dipping artifacts around the center of the array, near position 0 km. The free-surface multiple is significantly weaker than in the modelled response. This is not in accordance with the theory, which states that ballistic MDD retrieves the reflection response with free-surface interaction.

In Figure 2.3e the reflection response retrieved by full-field MDD is shown. The resolution is of the same quality as the modelled reflection response. The primary reflection is retrieved completely and is distinctly stronger than the artifacts in the background. The free-surface multiple is expected to be absent, but we can still see some remnants of it. The diffraction caused by the upper corner of the Moho discontinuity is, though obscured by artifacts, partially retrieved by full-field MDD.

When we compare results of ballistic and full-field MDD, we see that the latter

**2**
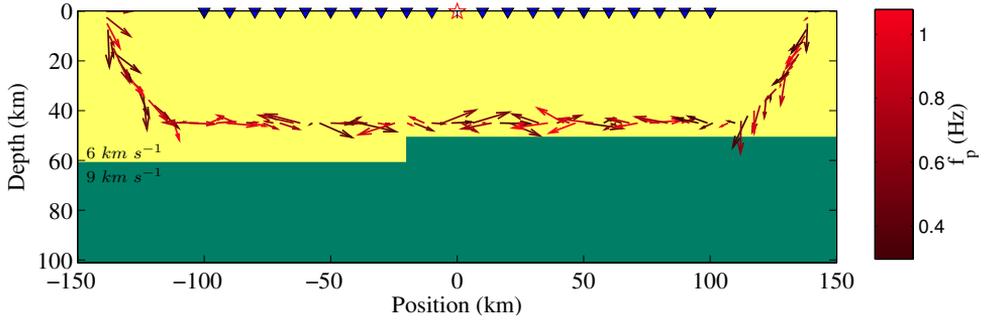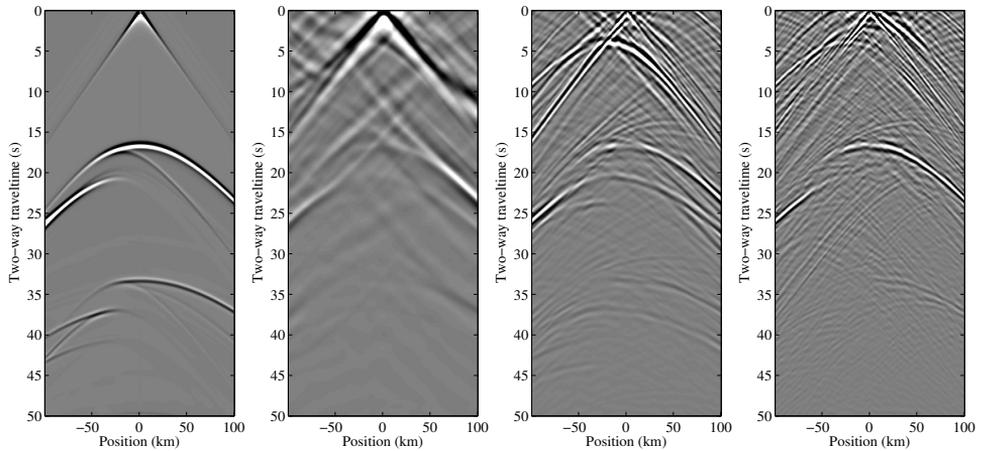


(a) Model



(b) Reference      (c) Crosscorrelation      (d) Ballistic MDD      (e) Full-field MDD

Figure 2.3: *Complete illumination scenario.* **(a)** *P-wave speed model ($km\ s^{-1}$) for the full illumi-nation scenario. The orientation and location of the passive dipole sources are denoted by arrows and the receivers by blue triangles. The color of the arrows indicates the peak frequency ($f_p$) of the passive-source signatures as specified by the color bar. The position along the horizontal axis corresponds with the horizontal axis of the modelled and retrieved shot gathers.* **(b)** *Modelled ver-tical particle-velocity reflection response to a vertical dipole-source placed at the the position of the middle receiver.* **(c)** *Vertical particle-velocity reflection response obtained by crosscorrelation.* **(d)** *Vertical particle-velocity reflection response obtained by ballistic MDD.* **(e)** *Vertical particle-velocity reflection response obtained by full-field MDD.*

gives a more distinct reflection response and is not as obscured by artifacts as the former. Full-field MDD does not contain the erroneous primary ghost we see in the result of ballistic MDD. This indicates that the full-field PSF is more effective in correcting for artifacts (see Figure 2.5b). Moreover, ballistic MDD required a stabilization parameter two orders of magnitude larger than full-field MDD.
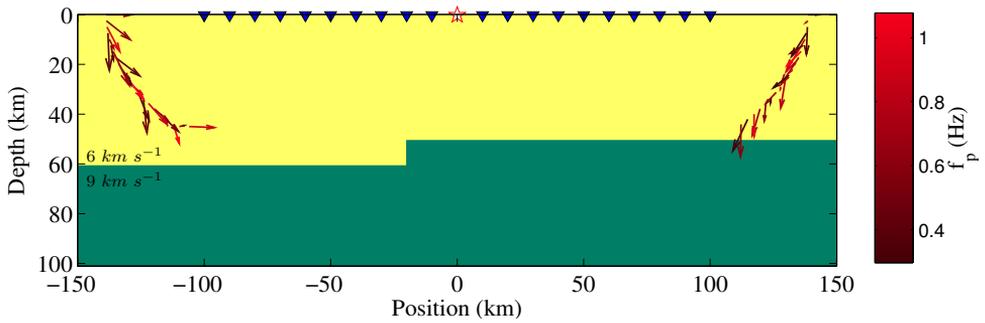
### 2.3.2. LIMITED ILLUMINATION

In Figure 2.4 we compare all three interferometric methods for the case of having passive sources positioned at the far sides of the model. In this challenging configuration, low-angle reflections at the center of the array can only be retrieved from the multiply scattered waves contained in the coda field of the input recordings.

The crosscorrelation result in this illumination scenario differs from the complete illumination case (Figure 2.3c) in that it does not show any sign of the Moho primary between positions -50 and 50 km (Figure 2.4c). This implies that for this situation, crosscorrelation only profits effectively from first order and not from higher order multiples, because only the latter could yield a retrieval of the Moho reflection at the positions between -50 and 50 km. This makes it impossible to detect the Moho discontinuity.

In Figure 2.4d the ballistic MDD result is shown, which is severely contaminated by artifacts and does not show a reflection retrieval. These artifacts are caused by the ballistic PSF, which is designed to correct for irregularities in virtual shot gathers which are entirely retrieved from the ballistic passive field, which is here constructed from high-angle events only (see Figure 2.5c). However, in this scenario, the retrieved virtual reflections can only be constructed from the scattered events contained in the passive recordings and thus the ballistic PSF will only introduce artifacts.

Figure 2.4e shows that full-field MDD does yield a visible reflection for all receiver positions. This is due to the fact that full-field MDD uses diffractions and multiples of different orders, contained in the coda field, to construct the reflection response for all available wavenumbers. The full-field PSF is designed to correct for illumination irregularities caused by both the ballistic and the coda wavefield (see Figure 2.5d). However, there is a noticeable decrease in amplitude for the lower wavenumbers, which makes it slightly more difficult to distinguish the primary from artifacts when compared to the case of complete illumination in Figure 2.3e. In spite of this, full-field MDD is the only method which can still obtain a reflection response under these severely limited illumination conditions and allows for a reasonably accurate interpretation of the Moho discontinuity.

(a) Model
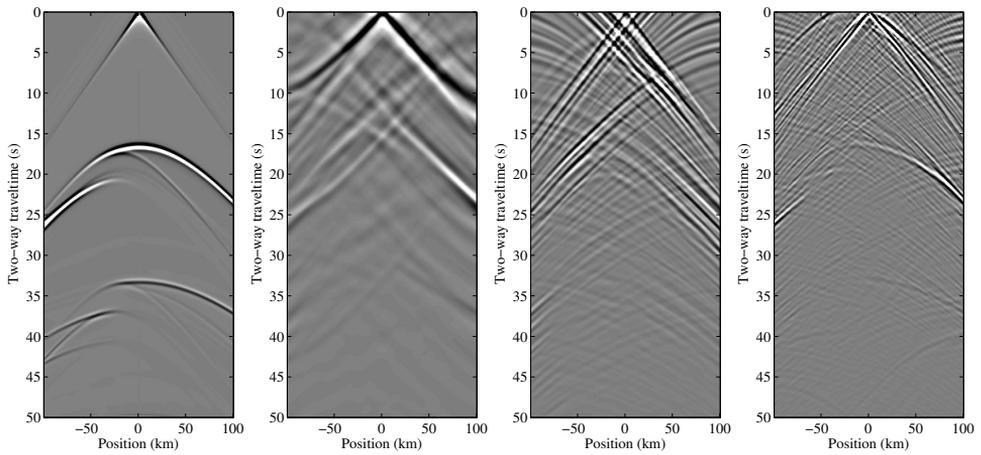


(b) Reference    (c) Crosscorrelation    (d) Ballistic MDD    (e) Full-field MDD

Figure 2.4: *Same as in Figure 2.3, but for limited illumination (high angles only).*

**COMPLETE ILLUMINATION**        **LIMITED ILLUMINATION**



(a) Ballistic PSF   (b) Full-field PSF   (c) Ballistic PSF   (d) Full-field PSF



(e) Ballistic PSF   (f) Full-field PSF   (g) Ballistic PSF   (h) Full-field PSF
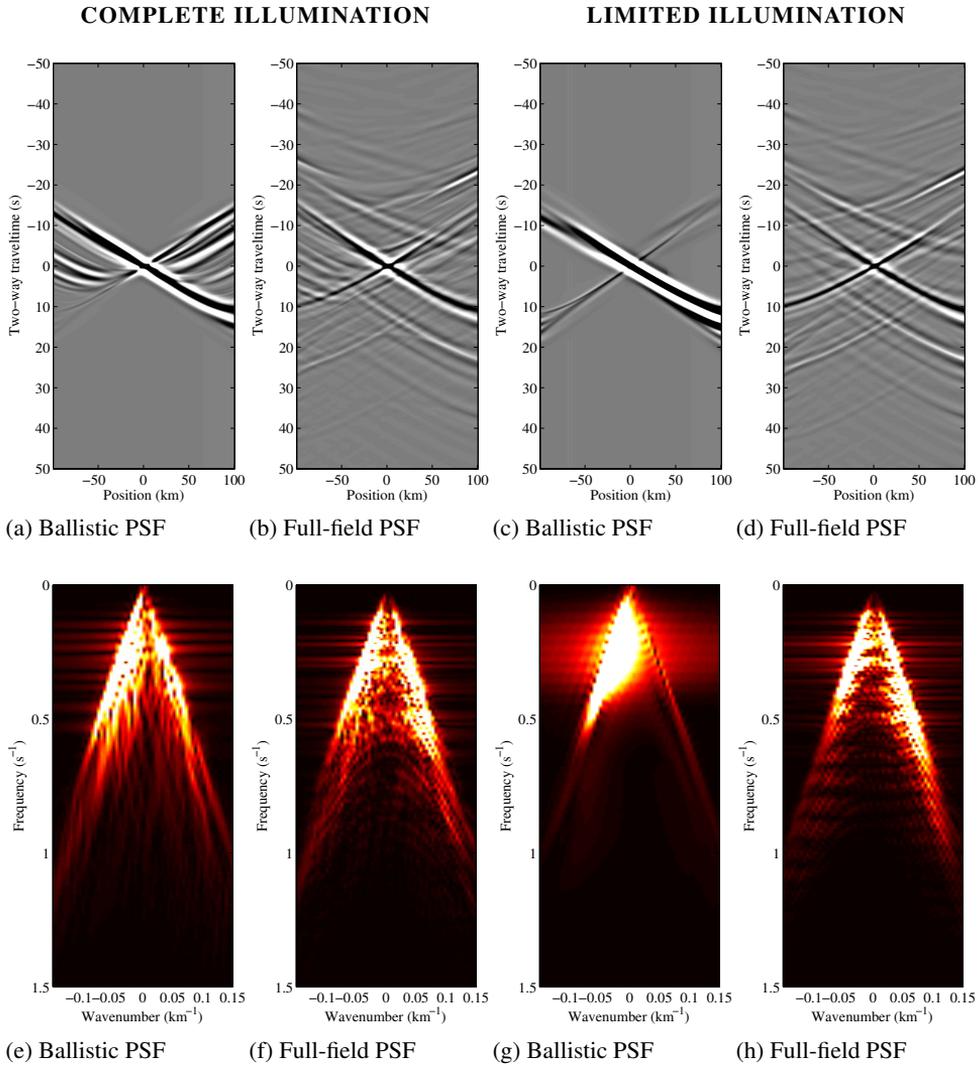
Figure 2.5: *Ballistic and full-field PSF's of the virtual source at position 0 km for the complete (Figure 2.3a) and limited (Figure 2.4a) illumination scenarios. (a) Ballistic PSF in the t-x domain for complete illumination. (b) Full-field PSF in the t-x domain for complete illumination. (c) Ballistic PSF in the t-x domain for limited illumination. (d) Full-field PSF in the t-x domain for limited illumination. (e)-(h) show the f-k spectra of (a)-(d).*

### 2.3.3. PSF ANALYSIS

Conventionally, the function of the PSF is to properly balance the virtual-shot gathers, such that each virtual source resembles an isotropic source mechanism. From the theory, as well as the numerical results, we have learned that the ballistic PSF achieves this by balancing the irregular illumination caused by the directly incident passive wavefields. On the other hand, the full-field PSF balances the irregular illumination associated with the full passive recording and additionally uses the scattered passive events to convert free surface multiples into primaries in the resulting reflection response. To gain insight into the differences in illumination characteristics, we compare the full-field and ballistic PSF in the time-space and frequency-wavenumber domains.

Firstly, the time-space plots in Figures 2.5a and 2.5c show that the ballistic PSF is constructed of the directly incident fields only, while Figures 2.5b and 2.5d show that the full-field PSF includes all scattered events as well. Note that the apparent difference between the full-field PSF in the case of complete and limited illumination is not significant. The frequency-wavenumber spectrum of the ballistic PSF (Figure 2.5e) shows that for complete illumination (Figure 2.3a), the ballistic fields provide a broad range of wavenumbers. This is in stark contrast with the case of limited illumination from the sides (Figure 2.4a), where the ballistic fields of the passive sources only provide high wavenumbers (Figure 2.5g). Moreover, the application of the tapered time-window for selecting the ballistic fields causes smearing, which introduces artificial low wavenumbers between 0.1 and 0.4 Hz.

Figures 2.5f and 2.5h show the corresponding full-field PSF's for the two illumination scenarios, which appear to be similar in spectral content even though the directional balancing is different for each scenario. In both cases, the full-field PSF clearly displays distinct features which indicate the presence of spectral information due to the coda wavefield, which is necessary to balance the virtual-source radiation and is responsible for converting free-surface multiples into primaries.

### 2.3.4. DIRECT-WAVE APPROXIMATION SENSITIVITY

Equations (2.5) and (2.11) both rely on the direct wave to approximate the reference-state response to the passive sources. This approximation will inevitably cause errors in retrieved reflections. To analyze this error, we additionally compute the reflection retrievals using equations (2.4) and (2.10), which are without the direct-wave approximation. This required numerical simulation of the actual reference-state responses by using the model setting in Figure 2.3a with absorbing boundary conditions at the top. This allows us to compare reflection responses obtained using

(a) Ballistic, eq (2.5)     (b) Ballistic, eq (2.4)     (c) Full-field, eq (2.11)     (d) Full-field, eq (2.10)
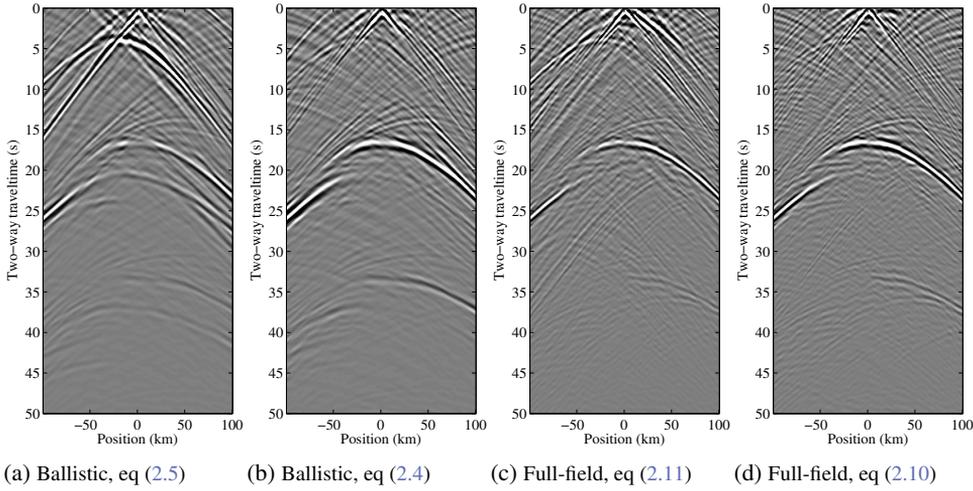
Figure 2.6: *MDD methods with and without direct-wave approximation, for the complete illumination scenario described by Figure 2.3a. (a) Vertical particle-velocity reflection response using ballistic MDD with direct-wave approximation. (b) Idem, using ballistic MDD formulation with modelled reference responses. (c) Idem, using full-field MDD with direct-wave approximation. (d) Idem, using full-field MDD formulation with modelled reference responses.*

the direct-wave approximation (equations (2.5) and (2.11)) and without using the direct-wave approximation (equations (2.4) and (2.10)).

Figures 2.6a and 2.6b show the reflection response retrieved by ballistic MDD using equations (2.5) and (2.4), respectively. In the result without approximation in Figure 2.6b, the primary is more distinct and continuous and the source ghost is less visible, compared to the result obtained using the direct-wave approximation in Figure 2.6a. The free-surface multiple is clearly more visible in Figure 2.6b, which is in accordance with the theory which states that ballistic MDD retrieves the response with free-surface interaction. Figures 2.6c and 2.6d display the results for full-field MDD with (equation (2.11)) and without using the direct-wave approximation (equation (2.10)), respectively. The free-surface multiple is suppressed in both figures (although some remnants are still visible), which agrees with the fact that full-field MDD retrieves the reflection response without free-surface interaction. Note that the two results for full-field MDD do not differ much from each other, although artifacts are less apparent in Figure 2.6d.

This comparison shows that ballistic MDD is more affected by the direct-wave approximation than full-field MDD, which could be predicted when comparing equations (2.5) and (2.11): the ballistic PSF requires the direct-wave approximation

while the full-field PSF does not.

### 2.3.5. NOISE SENSITIVITY

In order to create a more realistic scenario, we introduce noise in the modelled passive recordings. We generate random noise in the frequency-domain which is different for every shot and trace and we band-limit it between 0.01 and 2.6 Hz (see Figure 2.7c). In Figure 2.7b the effect of adding the noise can be seen in a trace at position 0 km of a passive-source recording. The primary, indicated by 'P', is easily recognizable in the trace contaminated by noise, but the first order free-surface multiple, indicated by 'M1', is below the noise level. This indicates that the ballistic field is not affected much by the noise, while the scattered events of the coda wavefield are. In the example of one of the passive-source recordings in Figure 2.7a the effect of the noise is clearly visible: the free-surface multiples of higher order are obscured.

We compare the retrieved vertical particle-velocity reflection responses, using the three SI methods for the case of limited illumination, as shown in Figure 2.4a. The retrieved response by crosscorrelation is unaffected by the introduction of noise (Figure 2.7e): the method diminishes incoherent or random events present in the input recordings. Ballistic and full-field MDD are much more affected by the noise (Figures 2.7f and 2.7g, respectively). This is because inversion is sensitive to the prevalence of noise. We partially compensated for this by increasing the stabilization parameter for full-field MDD to the same magnitude as used for ballistic MDD. Additional artifacts now contaminate the reflection response retrieved by ballistic MDD even more (Figure 2.7f). In Figure 2.7g it can be seen that the noise introduces a random pattern in the response retrieved by full-field MDD. However, the accuracy and visibility of the reflection response is not significantly affected with respect to Figure 2.4e. Moreover, the noise-related artifacts could be minimized by making use of sparsity promotion as presented by van der Neut & Herrmann (2013).

## 2.4. DISCUSSION

Earthquakes are generated by various complex mechanisms and are often sparsely distributed (Stein & Wysession, 2003). Our results show that the quality of the body-wave reflections obtained by crosscorrelation and ballistic MDD is severely affected when these realistic conditions are met (Figures 2.4c and 2.4d). In contrast, full-field MDD turns out to be significantly less sensitive to the possible adverse effects of these circumstances and yields a complete retrieval of the body-wave
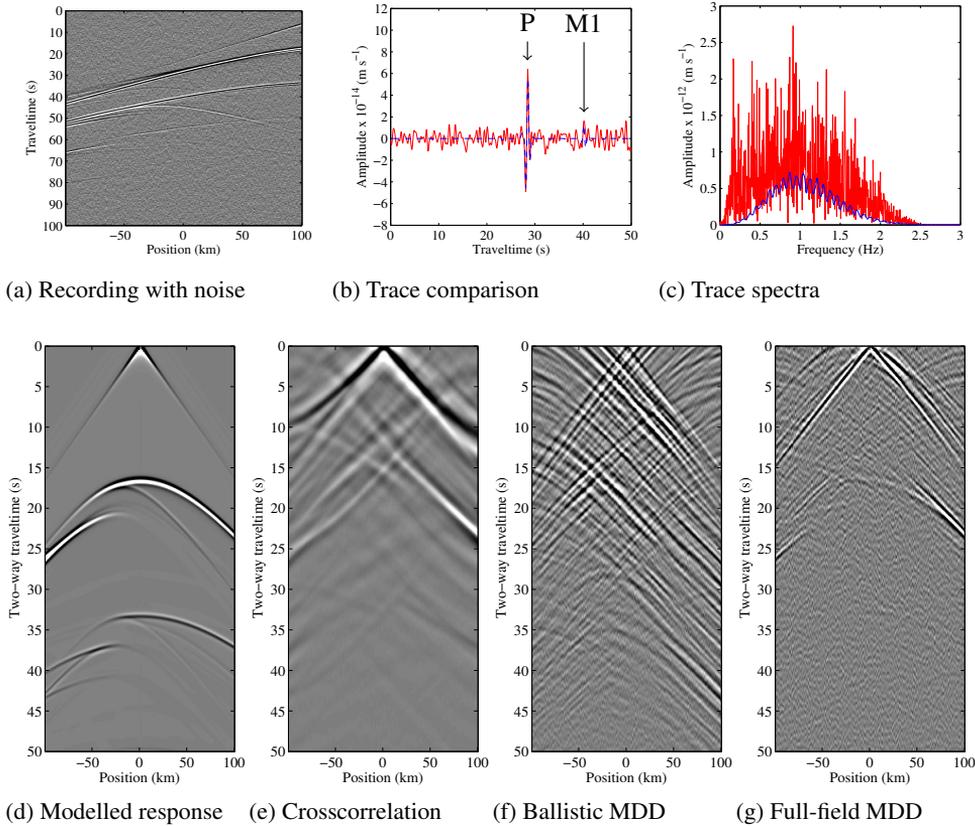
2



(a) Recording with noise

(b) Trace comparison

(c) Trace spectra



(d) Modelled response    (e) Crosscorrelation    (f) Ballistic MDD    (g) Full-field MDD

Figure 2.7: *Limited high-angle illumination scenario as described in Figure 2.4a, but with added noise. (a) Vertical particle-velocity recording of a passive source with added noise (the clipping is slightly increased). (b) Trace at position 0 km of a passive recording with (red) and without noise (dashed blue). The arrow with 'P' indicates the Moho primary and 'M1' the first order free-surface multiple. (c) Spectrum of the trace in (b) with (red) and without noise (blue) (d) Modelled vertical particle-velocity reflection response to a vertical dipole-source placed at the middle receiver.(e) Vertical particle-velocity reflection response from passive recordings with noise using crosscorrelation. (f) Idem, using ballistic MDD. (g) Idem, using full-field MDD.*

reflection (Figure 2.4e). Moreover, the addition of noise to the passive recordings does not significantly diminish the quality of the response retrieved by full-field MDD (Figure 2.7g).

The robustness of full-field MDD can be explained by the fact that its kernel equals the full passive recording (equation (2.7)). As a consequence, its PSF takes into account additional wavenumber illumination provided by the scattered events contained in the recording and thus also corrects for the irregular illumination these events may cause. Another benefit of this kernel is that it does not require any approximations, which results in a more constrained and stable inversion.

Wavefields with high-frequency content are more sensitive to the various scales of heterogeneities present in a realistic lithospheric medium: the scattering potential will effectively increase with higher frequency content (Sato et al., 2012). A medium with a stronger scattering potential has the advantage of increasing the range of wavenumbers contained in the illuminating field, which full-field MDD profits from. However, when the scattered field energy increases with respect to the ballistic field energy, the direct-wave approximation in the correlation function of full-field MDD will become less reliable. This can lead to an increase in the error in the estimate of the reflection response. This expected trade-off requires further research. Crosscorrelation does not rely on the direct-wave approximation and, in theory, would also profit from a stronger scattering potential in case this generates isotropically scattered waves at the receiver level (Snieder, 2004). However, a modelling study of coda-wave crosscorrelation interferometry showed that in case of only a slightly higher scattering potential, the reflection retrieval becomes obscured by the associated emergence of cross-talk artifacts (Hartstra & Wapenaar, 2015).

Another characteristic of strongly scattering media is that P- to S-wave conversions dominate the multiply scattered wavefield (Snieder, 2002). We derived the full-field MDD equation for elastodynamic wavefields (equation (2.A.25)), which only requires particle-velocity recordings as input and possibly does not require surface-wave removal. Using full-field MDD, we expect to retrieve an elastodynamic reflection response of a comparable quality as for the acoustic case demonstrated here.

Finally, we would like to point out that this method is not limited to lithospheric imaging applications. Depending on the characteristics of the array, full-field MDD could be used to obtain body-wave reflections on a global scale to shed light on mantle and core structures (Ruigrok, 2012). Additionally, the method could prove useful for monitoring purposes in marine ocean-bottom cable configurations by allowing the use of natural microseismic sources instead of active marine sources (Ravasi et al., 2015).

## 2.5. CONCLUSION

We derived a novel interferometric method by multidimensional deconvolution (MDD) for passive particle-velocity recordings at the free surface. The input data do not require wavefield decomposition and the retrieved reflection response does not contain free-surface multiples. In the retrieval process, the additional wavenumbers provided by the passive coda wavefield are effectively used to cover illumination gaps. Moreover, the method intrinsically corrects for any illumination irregularities caused by both the passive sources and the scattering inside the medium. The numerical experiments showed that the inversion does not become unstable in the case of having noise-contaminated recordings of sparsely distributed passive sources with strongly varying radiation patterns. When compared to conventional passive SI approaches, this novel MDD method provides a more accurate result under these circumstances.

## 2.A. DERIVATION OF FULL-FIELD MDD

Following Wapenaar & Fokkema (2006), we derive the full-field MDD relation for elastodynamic wavefields in an arbitrary inhomogeneous isotropic domain $\mathbb{D}$ with boundary $\partial\mathbb{D}$ and outward pointing normal vector $n_j$ (see Figure 2.2). We define two independent states A and B in the same domain $\mathbb{D}$ and introduce the local interaction quantity $\partial_j \left[ \hat{v}_i^A \hat{\tau}_{ij}^B - \hat{\tau}_{ij}^A \hat{v}_i^B \right]$, to relate fields in the respective states (Fokkema & van den Berg, 1993, de Hoop, 1995, Wapenaar, 1996), where 'hat' indicates the space-frequency domain. Capital superscripts denote which state the field belongs to, while lower-case subscripts indicate the component of each field, which can take up values 1, 2 and 3. The number of subscript letters designates the order of the tensor. Note that Einstein's summation convention holds here. The particle velocity is denoted by $\hat{v}_i$ and the tensorial stress field by $\hat{\tau}_{ij}$, where $i = j$ denotes normal stress and $i \neq j$ shear stress. We substitute Newton's second law and Hooke's law into the local interaction quantity and apply Gauss' theorem, yielding global reciprocity theorem:

$$\oint_{\partial\mathbb{D}} \left[ \hat{v}_i^A \hat{\tau}_{ij}^B - \hat{\tau}_{ij}^A \hat{v}_i^B \right] n_j d^2\mathbf{x} = \int_{\mathbb{D}} \left[ -\hat{\tau}_{ij}^A \hat{h}_{ij}^B - \hat{v}_i^A \hat{f}_i^B + \hat{h}_{ij}^A \hat{\tau}_{ij}^B + \hat{f}_i^A \hat{v}_i^B \right] d^3\mathbf{x}, \quad (2.A.12)$$

where $\hat{f}_i$ denotes the force density source and $\hat{h}_{ij}$ is the uniaxial shear density for $i = j$ and simple shear density source for $i \neq j$. In the following we assume that the medium parameters in $\mathbb{D}$ are the same in both states. In both states A and B, we divide the boundary of domain $\mathbb{D}$ into a horizontal acquisition surface defined by

the receiver positions, $\mathbf{x}_R \in \partial\mathbb{D}_R$, and a half-sphere in the subsurface, $\partial\mathbb{D}_M$, wich has absorbing boundary conditions in both states A and B. The boundary condition at $\partial\mathbb{D}_R$ differs between the two states: in state A it has absorbing boundary conditions, while in state B, it forms a free surface. The opposite is the case for the derivation of ballistic MDD by Wapenaar et al. (2008b) (Figure 2.1). The sources in state A are located at $\mathbf{x}_A$ just inside the domain immediately below the boundary $\partial\mathbb{D}_R$. In state B, the source locations $\mathbf{x}_B$ are located at arbitrary positions inside the domain $\mathbb{D}$. Since the final solution is independent of passive-source type, we take the liberty to neglect the $\hat{h}_{ij}$ sources. By extending boundary $\partial\mathbb{D}_M$ to infinity, the contribution of that part of the integral vanishes due to Sommerfeld's radiation condition. This results in:

$$\int_{\partial\mathbb{D}_R} \left[ \hat{v}_i^o \hat{\tau}_{ij} - \hat{\tau}_{ij}^o \hat{v}_i \right] n_j d^2\mathbf{x} = \int_{\mathbb{D}} \left[ -\hat{v}_i^o \hat{f}_i + \hat{f}_i^o \hat{v}_i \right] d^3\mathbf{x}, \tag{2.A.13}$$

where we also simplified the notation by denoting all wavefields of state A, which are without free-surface interaction, with a superscript '$o$', while wavefields in state B, which do have free-surface interaction, have no superscript. The field $\hat{\tau}_{ij} n_j$ does not contribute to the integral, because the acquisition surface $\partial\mathbb{D}_R$ coincides with the free surface of state B. Of the remaining field in the integrand, only the components perpendicular to the horizontal boundary $\partial\mathbb{D}_R$, which has an upward pointing normal vector, contribute to the integral: $\hat{\tau}_{ij}^o n_j \rightarrow -\hat{\tau}_{i3}^o$. Applying these constraints imposed by the boundary yields:

$$\int_{\partial\mathbb{D}_R} \hat{\tau}_{i3}^o \hat{v}_i d^2\mathbf{x}_R = \int_{\mathbb{D}} \left[ \hat{f}_i^o \hat{v}_i - \hat{v}_i^o \hat{f}_i \right] d^3\mathbf{x}. \tag{2.A.14}$$

We now proceed to define the source terms as impulsive functions and consequently the wavefield terms as Green's functions:

$$\hat{f}_i^o = \delta(\mathbf{x} - \mathbf{x}_A)\delta_{ik}, \tag{2.A.15}$$

$$\hat{v}_i^o = \hat{G}_{i|k}^o(\mathbf{x}, \mathbf{x}_A, \omega), \tag{2.A.16}$$

$$\hat{\tau}_{i3}^o = \hat{G}_{i3|k}^o(\mathbf{x}, \mathbf{x}_A, \omega), \tag{2.A.17}$$

$$\hat{f}_i = \delta(\mathbf{x} - \mathbf{x}_B)\delta_{iq}, \tag{2.A.18}$$

$$\hat{v}_i = \hat{G}_{i|q}(\mathbf{x}, \mathbf{x}_B, \omega), \tag{2.A.19}$$

where $\omega$ denotes the angular frequency. The lower-case subscripts, with possible values 1, 2 or 3, on the left-hand side of the vertical bar denote the receiver component of the field, while subscripts on the right-hand side denote the component

of the source mechanism. Substituting these expressions in the global reciprocity theorem (equation (2.A.14)), we solve the domain integral and apply the source-receiver reciprocity relations $\hat{G}^o_{k|i3}(\mathbf{x}_A, \mathbf{x}, \omega) = \hat{G}^o_{i3|k}(\mathbf{x}, \mathbf{x}_A, \omega)$ and $\hat{G}^o_{k|i}(\mathbf{x}_A, \mathbf{x}, \omega) = \hat{G}^o_{i|k}(\mathbf{x}, \mathbf{x}_A, \omega)$. The final result becomes:

$$\int_{\partial \mathbb{D}_R} \hat{G}^o_{k|i3}(\mathbf{x}_A, \mathbf{x}_R, \omega) \hat{G}_{i|q}(\mathbf{x}_R, \mathbf{x}_B, \omega) d^2\mathbf{x}_R = \hat{G}_{k|q}(\mathbf{x}_A, \mathbf{x}_B, \omega) - \hat{G}^o_{k|q}(\mathbf{x}_A, \mathbf{x}_B, \omega),$$
(2.A.20)

where $\hat{G}^o_{k|i3}(\mathbf{x}_A, \mathbf{x}_R, \omega)$ is the particle-velocity response at $\mathbf{x}_A$ to an impulsive shear density source at $\mathbf{x}_R$. Since $\mathbf{x}_A$ and $\mathbf{x}_R$ are immediately below and at the surface, respectively, $\hat{G}^o_{k|i3}(\mathbf{x}_A, \mathbf{x}_R, \omega)$ represents an impulsive reflection response (including the direct wave). Hence, we change its notation to:

$$\hat{R}^o_{k|i3}(\mathbf{x}_A, \mathbf{x}_R, \omega) = \hat{G}^o_{k|i3}(\mathbf{x}_A, \mathbf{x}_R, \omega).$$
(2.A.21)

We denote the particle-velocity field measured at the free surface due to an impulsive force at $\mathbf{x}_B$ with source spectrum $\hat{S}(\omega)$ as:

$$\hat{V}_{i|q}(\mathbf{x}_R, \mathbf{x}_B, \omega) = \hat{G}_{i|q}(\mathbf{x}_R, \mathbf{x}_B, \omega) \hat{S}(\omega).$$
(2.A.22)

The full response of the medium without free surface is presented as:

$$\hat{V}^o_{k|q}(\mathbf{x}_A, \mathbf{x}_B, \omega) = \hat{G}^o_{k|q}(\mathbf{x}_A, \mathbf{x}_B, \omega) \hat{S}(\omega),$$
(2.A.23)

and the full response of the medium with free surface is:

$$\hat{V}_{k|q}(\mathbf{x}_A, \mathbf{x}_B, \omega) = \hat{G}_{k|q}(\mathbf{x}_A, \mathbf{x}_B, \omega) \hat{S}(\omega).$$
(2.A.24)

Substituting definitions (2.A.21) - (2.A.24) into equation (2.A.20) yields the final elastodynamic full-field MDD relation:

$$\int_{\partial \mathbb{D}_R} \hat{R}^o_{k|i3}(\mathbf{x}_A, \mathbf{x}_R, \omega) \hat{V}_i(\mathbf{x}_R, \mathbf{x}_B, \omega) d^2\mathbf{x}_R = \hat{V}_k(\mathbf{x}_A, \mathbf{x}_B, \omega) - \hat{V}^o_k(\mathbf{x}_A, \mathbf{x}_B, \omega),$$
(2.A.25)

where we omitted subscript '$q$', because the passive-source mechanism does not influence the left-hand side of the equation. The desired $\hat{R}^o_{k|i3}(\mathbf{x}_A, \mathbf{x}_R, \omega)$ is the

particle-velocity reflection response of the medium without free surface at $\mathbf{x}_A$ due to a uniaxial or simple shear source, depending on subscript '$i$', at position $\mathbf{x}_R$ at the horizontal surface. Note that the surface orientation defines the virtual source orientation of the reflection response retrieval. The acoustic form of the equation is:

$$\int_{\partial \mathbb{D}_R} \hat{R}^o_{k|0}(\mathbf{x}_A, \mathbf{x}_R, \omega) \hat{V}_3(\mathbf{x}_R, \mathbf{x}_B, \omega) d^2 \mathbf{x}_R = \hat{V}_k(\mathbf{x}_A, \mathbf{x}_B, \omega) - \hat{V}^o_k(\mathbf{x}_A, \mathbf{x}_B, \omega), \quad (2.A.26)$$

whereby $\hat{R}^o_{k|0}(\mathbf{x}_A, \mathbf{x}_R, \omega)$ is the particle-velocity reflection response at $\mathbf{x}_A$ due to a scalar monopole source, indicated by source subscript zero '0', at $\mathbf{x}_R$. Note that $\hat{V}^o_k(\mathbf{x}_A, \mathbf{x}_B, \omega)$ can only be obtained by removing the free-surface multiples from the passive recorded field $\hat{V}_k(\mathbf{x}_A, \mathbf{x}_B, \omega)$. Since this is difficult to achieve in practice, the field can instead be approximated by selecting the direct wave of the passive recording and multiplying it by $\frac{1}{2}$ to remove the effect of the free surface. However, in the case of elastodynamic full-field MDD (equation (2.A.25)) this approximation does not suffice. Instead, wave-field decomposition is required to remove the effect of the free surface from the direct P- and S-wave.

# 3

# RETRIEVAL OF ELASTODYNAMIC REFLECTIONS FROM PASSIVE DOUBLE-COUPLE RECORDINGS

*Virtual Green's functions obtained by seismic interferometry (SI) can provide valuable reflectivity data that can complement tomographic inversion schemes. However, virtual reflections are affected by illumination irregularities that are typical of earthquake-induced wavefields recorded by the receiver array. As a consequence, irregular source distributions, scattering inside the medium and complex source mechanisms can significantly disturb the retrieval of Green's function approximations by conventional SI methods. We introduce SI by full-field multidimensional deconvolution (MDD) for elastodynamic wavefields as an alternative method to obtain body-wave Green's functions under those typical circumstances. The advantage of this method compared to other MDD methods is that the kernel of its governing equation is exact. This alternative formulation of the kernel pertains several advantages: the solution is less sensitive to artefacts and utilizes the free-surface multiples in the data to estimate primary reflections. Moreover, the point-spread function (PSF) of the full-field MDD method corrects more affectively for irregular illumination because it also addresses irregularities caused by scattering inside the medium. In order to compare full-field MDD to existing SI methods, we*

---

*model synthetic earthquake recordings in a subduction-zone setting using an elasto-dynamic finite-difference scheme with double-couples of different orientations and peak frequencies. Our results show that SI by crosscorrelation suffers most under these circumstances. Higher quality reflections are obtained by the MDD methods, of which full-field MDD involves the most stable inversion and its results are least contaminated by artefacts.*

**3**

## 3.1. Introduction

The Earth's lithosphere is continuously affected by a natural prevalent stress-field that is primarily driven by the motion of tectonic plates over the relatively ductile astenoshpere (Fowler, 2005). Ultimately, natural earthquakes can be triggered when accumulated stress gets released by the collapse of shear (Aki & Richards, 2002). When estimates of the locations and timings of earthquakes are available, the travel times of the induced seismic waves can be used to calculate the propagation velocity of the subsurface structure. Correspondingly, a smooth velocity model of the subsurface is obtained from the tomographic inversion of travel times of all earthquake-receiver pairs (Kennett, 1998, Nolet, 2008). The accuracy of tomographic models relies on the quality of earthquake timing estimates, which can pose a challenge.

Claerbout (1968) showed that autocorrelation of the recording of the transmission response by a single receiver yields the estimation of the seismic reflection response as if there were a source at the position of this same receiver. The application of reciprocity theorems (de Hoop, 1995), made it possible to extend this 1D concept to seismic recordings in higher dimensions (Wapenaar, 2004). Obtaining complete virtual reflection surveys by crosscorrelating earthquake body-wave recordings is a subclass of seismic interferometry (SI) (Schuster, 2001, Wapenaar, 2004, Snieder, 2004, Larose et al., 2006). The methodology is analogous to surface-wave Green's function retrieval (Campillo & Paul, 2003, Sabra et al., 2005), except that body-waves instead of surface-waves are crosscorrelated. Seismic interferometry with body-waves can provide valuable complementary information of the subsurface structure. It exploits the scattered field from the earthquake recordings to retrieve reflection surveys analogous to those in exploration geophysics. These virtual reflection surveys obtained with SI can yield impedance contrasts with superior vertical resolution and are independent of earthquake timing. Several approaches to body-wave interferometry exist, of which the crosscorrelation method is the most widely used (Wapenaar & Fokkema, 2006, Schuster, 2009).

Green's functions obtained by crosscorrelation have a well-defined virtual-source location and timing, and make effective use of the higher wavenumber content of

the seismic wavefield. Therefore, they have the potential to approximate reflections of the subsurface structure, which can be used to determine valuable parameters such as the depth of a subduction slab or the Moho. In the past, body-wave SI by crosscorrelation has been validated numerically with acoustic models (Draganov et al., 2006) and has found numerous field applications (Draganov et al., 2007, Tonegawa et al., 2009, Zhan et al., 2010, Lin et al., 2013, Nishida, 2013, Boué et al., 2014). However, its sensitivity to inhomogeneous illumination conditions in the recorded wavefield can result in spurious events and inaccurate amplitudes that affect the accuracy of the retrieved Green's function. Natural seismic illumination is inherently irregular, due to the uneven spatial distribution of earthquakes, but also due to scattering inside the medium and the complex source mechanisms of earthquakes. This renders it unlikely to obtain  Green's function estimates that contain accurate reflections with SI by crosscorrelation on field data.

Several approaches have been proposed that deal with one or more of these limitations. For example, by applying appropriate weighting one can effectively correct for the illumination irregularities that cause artefacts in the Green's function estimate (Curtis & Halliday, 2010, Almagro Vidal et al., 2014). Although this approach has proven successful, it is sensitive to the choice of weights. Following a different strategy, Fichtner et al. (2017) proposed a method that exploits the benefits of SI for the purpose of tomographic inversion, by circumventing the requirement to obtain an accurate Green's function between receivers. Instead of inverting for the accurate Green's function, the inverse problem is formulated for the crosscorrelation function that is actually obtained by SI, thereby taking its artefacts into account.

SI by multidimensional deconvolution (MDD) methods offer alternatives to crosscorrelation for obtaining  Green's functions from earthquake recordings (Wapenaar et al., 2008b, van der Neut et al., 2010). These methods aim to correct for any irregularities in the virtual-source radiation by inversion: a deconvolution process that involves all receivers simultaneously, hence the term 'multidimensional'. Acoustic numerical experiments using an irregular distribution of passive monopole sources showed that MDD yields a more accurate Green's function than crosscorrelation. Essential in this process is the formulation of the quantity that is inverted: the interferometric point-spread function (PSF). The PSF has encoded the spectral information of the virtual-source radiation pattern that it aims to balance, such that the spurious events and incorrect amplitudes of the retrieved reflections get minimized.

Almagro Vidal (2017) showed that, for body-wave interferometry, two main types of MDD methods can be distinguished by the manner in which they utilize the free-surface multiples from the earthquake recordings and the spectral content of the PSF: ballistic and full-field MDD. Ballistic MDD (Wapenaar et al., 2008b) approx-

**3**

imates the PSF from the directly incident (ballistic) wavefield to obtain the Green's function with free-surface multiples, while full-field MDD uses the full recorded wavefield to construct the PSF to yield the Green's function without free-surface multiples (Hartstra et al., 2017). Acoustic numerical experiments using a limited distribution of passive dipole sources with varying radiation patterns showed that full-field MDD yields a more accurate Green's function than crosscorrelation and ballistic MDD. Ballistic MDD, formulated for decomposed one-way wavefields in elastic media, has been applied to obtain virtual reflections from field data (Nakata et al., 2014). The main challenge of MDD applications is that they require an estimation of the earthquake recordings without free-surface multiples.

For the purpose of obtaining an accurate Green's function from earthquake recordings, we propose elastodynamic full-field MDD as an alternative interferometric method. We conduct numerical experiments in order to compare the quality of the Green's functions obtained by crosscorrelation, ballistic MDD (as well as an approximation of this method) and full-field MDD. These interferometric methods have been validated in previous work with acoustic models using monopole or dipole passive sources. However, the acoustic regime cannot take into account certain characteristics of a typical field setting that could have significant impact on the performance of SI methods. In a field setting, the recorded passive wavefield contains P- and S-converted waves generated by earthquake source mechanisms that radiate the seismic energy in a complex and unique manner (Stein & Wysession, 2003). In order to make a realistic comparison, we generate synthetic earthquake recordings by implementing double-couples with varying peak frequencies, magnitudes and orientations in an elastic subduction-zone model.

## 3.2. METHODS

In this section, we present the different SI methods employed for body-wave reflection retrieval at the free surface and analyze their validation for elastodynamic scenarios.

### 3.2.1. CROSSCORRELATION

There exist several ways to derive the governing equation for the crosscorrelation method. Here, a distinction can be made between the expression for closed systems (Lobkis & Weaver, 2001) and for open systems (Snieder, 2004, Claerbout, 1968, Derode et al., 2003). We apply SI by crosscorrelation based on the reciprocity theorem of the correlation type for open systems (de Hoop, 1995) and work with an approximation of the 3D elastodynamic crosscorrelation expression in the

frequency domain (equation (80) from Wapenaar & Fokkema (2006)):

$$\Re\left[\hat{R}_{k|j}(\mathbf{x}_A,\mathbf{x}_R,\omega)\right]\langle\hat{S}(\omega)\rangle \propto \int_{\partial\mathbb{D}_S}\hat{V}_k(\mathbf{x}_A,\mathbf{x}_B,\omega)\hat{V}_j^*(\mathbf{x}_R,\mathbf{x}_B,\omega)d^2\mathbf{x}_B, \qquad (3.1)$$

Note that we use a proportionality symbol, because we adjusted equation (80) from Wapenaar & Fokkema (2006) by neglecting the effects of the imprint of the passive source radiation patterns and possible variations of the medium parameters along the passive sources. We use the symbol $R$ to denote the reflection response Green's function throughout this article. The desired $\hat{R}_{k|j}(\mathbf{x}_A,\mathbf{x}_R,\omega)$ is the $k$-component of the particle-velocity reflection response of the medium with free surface, observed at $\mathbf{x}_A$ due to a virtual $j$-component traction source at $\mathbf{x}_R$, both at the free surface. $\omega$ denotes the angular frequency. The symbol $\Re$ indicates that we obtain the real part of this reflection response, which is multiplied with the average of the earthquakes' power spectra: $\hat{S}(\omega)$. $\hat{V}_k(\mathbf{x}_A,\mathbf{x}_B,\omega)$ is the particle-velocity field measured at receiver $\mathbf{x}_A$ due to an earthquake at an unknown position in the subsurface, $\mathbf{x}_B$. Note that superscript $^*$ denotes complex conjugation, which implies that the product in the integrand corresponds to crosscorrelation in the time-domain. The integral in the right-hand side of (3.1) is defined along the earthquake locations $\mathbf{x}_B \in \partial\mathbb{D}_S$ in the subsurface. This integral imposes the requirement on SI by crosscorrelation that the earthquakes must form a uniform spatial distribution along an arbitrary boundary $\partial\mathbb{D}_S$ in the subsurface. Note that we will apply equation (3.1) in 2D, which means that the earthquakes must be distributed along a continuous line boundary $\partial\mathbb{D}_S$. Since in interferometry we assume to have no prior knowledge of the source characteristics, we do not take into account the medium parameters surrounding the source nor the specifics of the source radiation pattern.

### 3.2.2. BALLISTIC MDD

SI by ballistic MDD is based on the reciprocity theorem of the convolution type. Its governing equation for elastodynamic wavefields in 3D media reads (Wapenaar et al., 2008b):

$$\int_{\partial\mathbb{D}_R}\hat{R}_{k|j}(\mathbf{x}_A,\mathbf{x}_R,\omega)\hat{\tau}_{j3}^o(\mathbf{x}_R,\mathbf{x}_B,\omega)d^2\mathbf{x}_R \approx \hat{V}_k(\mathbf{x}_A,\mathbf{x}_B,\omega) - \hat{V}_k^o(\mathbf{x}_A,\mathbf{x}_B,\omega), \qquad (3.2)$$

where the integral is along a limited array of receivers positioned at $\mathbf{x}_R$ at a horizontal acquisition surface $\partial\mathbb{D}_R$ which we choose to be a free surface. $\hat{V}_k(\mathbf{x}_A,\mathbf{x}_B,\omega)$

and $\hat{V}_k^o(\mathbf{x}_A, \mathbf{x}_B, \omega)$ are the particle-velocity recordings at receiver $\mathbf{x}_A \in \partial \mathbb{D}_R$ with and without free-surface multiples, respectively, (the latter indicated by superscript $o$) due to an earthquake at an unknown position $\mathbf{x}_B$ in the medium. Note that the source-properties of the earthquakes do not impose any conditions on the validity of this representation. $\hat{\tau}_{j3}^o(\mathbf{x}_R, \mathbf{x}_B, \omega)$ is the stress field without free-surface multiples measured at receiver $\mathbf{x}_R$ due to the same earthquake at $\mathbf{x}_B$. The integration in the left-hand side involves all the receiver locations along the acquisition surface. Contrary to from the explicit equation (3.1), equation (3.2) is an implicit relation for $\hat{R}_{k|j}$, where the product whithin the integral stands for a convolution in the time-domain.

In order to solve for the desired reflection response $\hat{R}_{k|j}$, we first approximate the kernel of the equation, $\hat{\tau}_{j3}^o$, by the particle-velocity recordings:

$$\hat{\tau}_{13}^o(\mathbf{x}_R, \mathbf{x}_B, \omega) \approx \rho c_S \hat{V}_1^o(\mathbf{x}_R, \mathbf{x}_B, \omega), \qquad (3.3)$$

$$\hat{\tau}_{23}^o(\mathbf{x}_R, \mathbf{x}_B, \omega) \approx \rho c_S \hat{V}_2^o(\mathbf{x}_R, \mathbf{x}_B, \omega), \qquad (3.4)$$

$$\hat{\tau}_{33}^o(\mathbf{x}_R, \mathbf{x}_B, \omega) \approx \rho c_P \hat{V}_3^o(\mathbf{x}_R, \mathbf{x}_B, \omega), \qquad (3.5)$$

whereby we make the pragmatic assumption that the horizontal component is dominated by S-waves and the vertical component by P-waves. Here, $c_P$ and $c_S$ are the averaged P- and S-velocity values and $\rho$ the density of the medium at the receiver level. The thickness of the layer over which must be averaged to determine these velocities at the receiver level depends on the dominant wavelength of the recordings. Note that the wavefield $\hat{V}_j^o$ includes upgoing direct arrivals and internal multiples from the earthquake recordings, but explicitly excludes any arrivals that interacted with the free surface. Since it is very difficult to remove surface-related multiples from earthquake recordings $\hat{V}_j$, we only use their upgoing direct P- and S- arrivals to approximate $\hat{V}_j^o$. We refer to these upgoing direct arrivals of earthquake recordings as the 'ballistic field' and we denote them with a superscript $D$: $\hat{V}_j^o \approx \hat{V}_j^D$. Considering that the downgoing part of the direct arrivals interacted with the free surface, we multiply the direct P-wave ($\hat{V}_j^{P,dir}$) and S-wave ($\hat{V}_j^{S,dir}$) arrivals of $\hat{V}_j$ by a factor one half in order to select only the upgoing part. The direct-wave approximation ($\hat{V}_j^D$) of the $\hat{V}_j^o$ field thus becomes:

$$\hat{V}_j^o \approx \hat{V}_j^D = \tfrac{1}{2} \hat{V}_j^{P,dir} + \tfrac{1}{2} \hat{V}_j^{S,dir} \qquad (3.6)$$

Note that this is a crude approximation, since elastodynamic conversion at the free surface results in angle-dependent reflection coefficients. A more accurate esti-

mation of upgoing fields could be obtained by applying elastodynamic wavefield decomposition (Wapenaar et al., 2008a, Nakata et al., 2014). Since our objective is to keep processing to a minimum and to ensure the methods remain straightforward for field applications, we stick with approximation (3.6). Introducing the aforementioned approximations (3.3) - (3.6) into equation (3.2) gives:

$$\int_{\partial\mathbb{D}_R} \hat{R}_{k|j}(\mathbf{x}_A, \mathbf{x}_R, \omega) \, w \, \hat{V}_j^D(\mathbf{x}_R, \mathbf{x}_B, \omega) \, d^2\mathbf{x}_R \approx \hat{V}_k(\mathbf{x}_A, \mathbf{x}_B, \omega) - \hat{V}_k^D(\mathbf{x}_A, \mathbf{x}_B, \omega), \quad (3.7)$$

**3**

with weights:

$$w = \begin{cases} \rho c_S, & \text{if } j = 1, 2 \\ \rho c_P, & \text{if } j = 3 \end{cases}$$

Equation (3.7) represents a Fredholm integral of the first kind (Arfken & Weber, 2005) with a kernel that is approximated by the ballistic field of each respective earthquake recording. We formulate this problem in 2D ($j = 1, 3$) and employ a matrix notation (Berkhout, 1982):

$$\begin{bmatrix} \hat{\mathbf{R}}_{1|1} & \hat{\mathbf{R}}_{1|3} \\ \hat{\mathbf{R}}_{3|1} & \hat{\mathbf{R}}_{3|3} \end{bmatrix} \begin{bmatrix} \rho c_S \hat{\mathbf{V}}_1^D \\ \rho c_P \hat{\mathbf{V}}_3^D \end{bmatrix} \approx \begin{bmatrix} \hat{\mathbf{V}}_1 - \hat{\mathbf{V}}_1^D \\ \hat{\mathbf{V}}_3 - \hat{\mathbf{V}}_3^D \end{bmatrix}. \tag{3.8}$$

The field matrices $\hat{\mathbf{V}}_k$ and $\hat{\mathbf{V}}_k^D$, respectively, contain the independent non-overlapping recordings of earthquakes and their direct arrivals, whereby each row represents a receiver position and each column an earthquake. The reflection responses $\hat{\mathbf{R}}_{k|j}$ are square matrices with rows representing receivers and columns corresponding to independent virtual sources (whose positions coincide with the receivers). The normal form of equation (3.8) can be obtained by multiplying both sides with the transposed complex conjugated form of the kernel matrix:

$$\begin{bmatrix} \hat{\mathbf{R}}_{1|1} & \hat{\mathbf{R}}_{1|3} \\ \hat{\mathbf{R}}_{3|1} & \hat{\mathbf{R}}_{3|3} \end{bmatrix} \rho \begin{bmatrix} c_S^2 \hat{\mathbf{V}}_1^D \hat{\mathbf{V}}_1^{D\dagger} & c_S c_P \hat{\mathbf{V}}_1^D \hat{\mathbf{V}}_3^{D\dagger} \\ c_P c_S \hat{\mathbf{V}}_3^D \hat{\mathbf{V}}_1^{D\dagger} & c_P^2 \hat{\mathbf{V}}_3^D \hat{\mathbf{V}}_3^{D\dagger} \end{bmatrix} \approx$$
$$\begin{bmatrix} (\hat{\mathbf{V}}_1 - \hat{\mathbf{V}}_1^D) c_S \hat{\mathbf{V}}_1^{D\dagger} & (\hat{\mathbf{V}}_1 - \hat{\mathbf{V}}_1^D) c_P \hat{\mathbf{V}}_3^{D\dagger} \\ (\hat{\mathbf{V}}_3 - \hat{\mathbf{V}}_3^D) c_S \hat{\mathbf{V}}_1^{D\dagger} & (\hat{\mathbf{V}}_3 - \hat{\mathbf{V}}_3^D) c_P \hat{\mathbf{V}}_3^{D\dagger} \end{bmatrix}, \tag{3.9}$$

where superscript † indicates transposition and complex conjugation. We can solve for the reflection responses by applying a regularized least-squares inversion scheme, yielding the following approximate solution:

$$
\begin{bmatrix} \hat{\mathbf{R}}_{1|1} & \hat{\mathbf{R}}_{1|3} \\ \hat{\mathbf{R}}_{3|1} & \hat{\mathbf{R}}_{3|3} \end{bmatrix} \approx
$$

$$
\begin{bmatrix} (\hat{\mathbf{V}}_1 - \hat{\mathbf{V}}_1^D)\, c_S \hat{\mathbf{V}}_1^{D\dagger} & (\hat{\mathbf{V}}_1 - \hat{\mathbf{V}}_1^D)\, c_P \hat{\mathbf{V}}_3^{D\dagger} \\ (\hat{\mathbf{V}}_3 - \hat{\mathbf{V}}_3^D)\, c_S \hat{\mathbf{V}}_1^{D\dagger} & (\hat{\mathbf{V}}_3 - \hat{\mathbf{V}}_3^D)\, c_P \hat{\mathbf{V}}_3^{D\dagger} \end{bmatrix} \left( \rho \begin{bmatrix} c_S^2 \hat{\mathbf{V}}_1^D \hat{\mathbf{V}}_1^{D\dagger} & c_S c_P \hat{\mathbf{V}}_1^D \hat{\mathbf{V}}_3^{D\dagger} \\ c_P c_S \hat{\mathbf{V}}_3^D \hat{\mathbf{V}}_1^{D\dagger} & c_P^2 \hat{\mathbf{V}}_3^D \hat{\mathbf{V}}_3^{D\dagger} \end{bmatrix} + \epsilon^2 \mathbf{I} \right)^{-1},
$$

$$(3.10)$$

where $\epsilon^2$ is the stabilization parameter and $\mathbf{I}$ is the identity matrix (Arfken & Weber, 2005). By including more recordings of independent earthquake events, the extra illumination information they provide can serve to better constrain the estimation of the reflection responses. Note that the right-hand side of equation (3.10) represents the process of constructing a correlation function (first term in square brackets) that is subsequently 'deblurred' by a PSF (second term in square brackets). However, since it is constructed by the inexact kernel of the original equation (3.7), this PSF will not be exact: it is approximated by the direct arrivals, the ballistic field, of the earthquake recordings.

The ballistic PSF has two disadvantages. The first is caused by the fact that the input wavefield is obtained from the earthquake recordings by a time-windowing procedure, which requires a taper and is user-dependent. During its inversion (equation (3.10)) this will inevitably contaminate the solution. Secondly, since only direct waves are used to construct it, the PSF will not be able to balance illumination irregularities caused by scattering inside the medium. Just like SI by crosscorrelation, also ballistic MDD relies strongly on the natural illumination. Nevertheless, it is capable of correcting for the irregularities in the ballistic field which are due to the effects of nonuniform source distributions and complex varying source mechanisms.

In the case of ambient-noise recordings, the direct arrival overlaps with the subsequent arrivals because the source-function is too long: this makes it impossible to select the direct arrival by time-windowing. Naturally, this does not pose any problems for the application of the crosscorrelation method (Roux et al., 2005, Stehly et al., 2006, Poli et al., 2012, Lin et al., 2013). In the case of ballistic MDD, an adaptation is required to deal with the ambient-noise scenario: this method involves constructing the PSF by applying time windows after crosscorrelation (van der Neut et al., 2010, Wapenaar et al., 2011). Acoustic synthetic experiments have shown that

the PSF constructed in this way successfully corrects for irregular passive source distributions. Since this method was specifically developed for ambient-noise seismic interferometry (ANSI) applications, we refer to it here as ANSI-MDD. The elastodynamic form of ANSI-MDD is formulated with matrix notation in the frequency domain as:

$$
\begin{bmatrix} \hat{\mathbf{R}}_{1|1} & \hat{\mathbf{R}}_{1|3} \\ \hat{\mathbf{R}}_{3|1} & \hat{\mathbf{R}}_{3|3} \end{bmatrix} \approx \begin{bmatrix} \hat{\mathbf{V}}_1\hat{\mathbf{V}}_1^\dagger - \hat{\Gamma}_{11} & \hat{\mathbf{V}}_1\hat{\mathbf{V}}_3^\dagger - \hat{\Gamma}_{13} \\ \hat{\mathbf{V}}_3\hat{\mathbf{V}}_1^\dagger - \hat{\Gamma}_{31} & \hat{\mathbf{V}}_3\hat{\mathbf{V}}_3^\dagger - \hat{\Gamma}_{33} \end{bmatrix} \left( \begin{bmatrix} \hat{\Gamma}_{11} & \hat{\Gamma}_{13} \\ \hat{\Gamma}_{31} & \hat{\Gamma}_{33} \end{bmatrix} + \epsilon^2\mathbf{I} \right)^{-1}, \qquad (3.11)
$$

where the virtual ballistic PSF, $\hat{\Gamma}_{kj}$, contains the virtual source radiation pattern which is selected with time windows around $t = 0$ from the inverse Fourier transform of $\hat{\mathbf{V}}_k\hat{\mathbf{V}}_j^\dagger$. The limits of this time window are defined by the virtual direct P-wave arrival and its time-reversal. However, we emphasize that the stability of the solution is very sensitive to the selection of the time-window for this PSF, which is particularly difficult to calibrate correctly in the case of field data.

### 3.2.3. FULL-FIELD MDD

SI by full-field MDD is based on the reciprocity theorem of the convolution type. The 3D elastodynamic form of full-field MDD for two-way wavefields (Hartstra et al., 2017) reads:

$$
\int_{\partial\mathbb{D}_R} \hat{R}^o_{k|i3}(\mathbf{x}_A,\mathbf{x}_R,\omega)\,\hat{V}_i(\mathbf{x}_R,\mathbf{x}_B,\omega)\,d^2\mathbf{x}_R \approx \hat{V}_k(\mathbf{x}_A,\mathbf{x}_B,\omega) - \hat{V}^o_k(\mathbf{x}_A,\mathbf{x}_B,\omega), \qquad (3.12)
$$

where the integral is along a limited array of receivers positioned at $\mathbf{x}_R$ at a horizontal acquisition surface $\partial\mathbb{D}_R$ which we choose to be at the free surface. Like equation (3.7), this equation presents a Fredholm integral of the first kind, but with a kernel, $\hat{V}_i(\mathbf{x}_R,\mathbf{x}_B,\omega)$, that does not require approximations: it is the observed particle-velocity recording of an earthquake including free-surface multiples. The solution $\hat{R}^o_{k|i3}(\mathbf{x}_A,\mathbf{x}_R,\omega)$ is the $k$-component particle-velocity response at $\mathbf{x}_A$ due to an uniaxial or a simple-shear stress point-source, depending on subscript $i$, at position $\mathbf{x}_R$, without free-surface multiples. Note that, because of the different source type, $\hat{R}^o_{k|i3}$ in equation (3.12) has a different dimension than $\hat{R}_{k|j}$ in equation (3.2). The right-hand side of equation (3.12) is exactly the same as in equation (3.2). Therefore, we apply the same approximation as used there: $\hat{V}^o_k(\mathbf{x}_A,\mathbf{x}_B,\omega)$ is estimated by selecting the direct P- and S- arrivals from the earthquake recordings, $\hat{V}_k(\mathbf{x}_A,\mathbf{x}_B,\omega)$, and multiplying both by a factor one half (this approximation is again denoted as $\hat{V}^D$).

The regularized least-squares solution of equation (3.12) using the matrix notation becomes in 2D:

$$
\begin{bmatrix} \hat{\mathbf{R}}^o_{1|13} & \hat{\mathbf{R}}^o_{1|33} \\ \hat{\mathbf{R}}^o_{3|13} & \hat{\mathbf{R}}^o_{3|33} \end{bmatrix} \approx \begin{bmatrix} (\hat{\mathbf{V}}_1 - \hat{\mathbf{V}}^D_1)\hat{\mathbf{V}}^\dagger_1 & (\hat{\mathbf{V}}_1 - \hat{\mathbf{V}}^D_1)\hat{\mathbf{V}}^\dagger_3 \\ (\hat{\mathbf{V}}_3 - \hat{\mathbf{V}}^D_3)\hat{\mathbf{V}}^\dagger_1 & (\hat{\mathbf{V}}_3 - \hat{\mathbf{V}}^D_3)\hat{\mathbf{V}}^\dagger_3 \end{bmatrix} \left( \begin{bmatrix} \hat{\mathbf{V}}_1\hat{\mathbf{V}}^\dagger_1 & \hat{\mathbf{V}}_1\hat{\mathbf{V}}^\dagger_3 \\ \hat{\mathbf{V}}_3\hat{\mathbf{V}}^\dagger_1 & \hat{\mathbf{V}}_3\hat{\mathbf{V}}^\dagger_3 \end{bmatrix} + \epsilon^2 \mathbf{I} \right)^{-1}. \quad (3.13)
$$

Different from the ballistic PSF of equation (3.10), the full-field PSF (i.e., the inverted matrix on the right-hand side) does not require approximations nor is affected by time-windowing procedures. However, its main advantage over the ballistic PSF is that it contains the maximum spectral information as provided by the full earthquake recording. Therefore, full-field MDD is less dependent on obtaining the required spectral information from the ballistic field of the earthquakes, since it additionally exploits the spectral information contained in the earthquake's scattering coda and thus also corrects for illumination irregularities caused by scattering (Almagro Vidal, 2017, Hartstra et al., 2017).

## 3.3. NUMERICAL EXPERIMENTS

We analyse the performance of the different SI methods using an elastodynamic finite-difference code to simulate independent, nonoverlapping earthquake recordings in 2D media (Thorbecke & Draganov, 2011). Figure 3.1 depicts our model design, inspired by the Cascadia subduction zone (Chen et al., 2015). The lithospheric crust has P- and S-wave velocities of 6 and 3.5 km s$^{-1}$, respectively, and the Moho is at a depth of 35 km. The mantle material below has P- and S-wave velocities of 8 and 4 km s$^{-1}$, and the subducting oceanic slab has velocities of 8.5 and 4.25 km s$^{-1}$, respectively. The densities of the crust, mantle and slab are 2700, 3000 and 3500 kg m$^{-3}$, respectively.

In order to simulate recordings of realistic earthquake sources, we implement shear-stress sources with a typical double-couple radiation pattern. Besides some exceptions, e.g. volcanic eruptions, earthquakes are generally triggered by a release of accumulated shear-stress, accommodated by the sudden movement of rock masses along a fault plane. The geometry of the fault and the petrophysical parameters of the surrounding rock masses determine the initial radiation characteristics of the source mechanism of the earthquake, such as magnitude, frequency content and the directional radiation of seismic waves. The fault-slip motion radiates both P- and S-waves in a complex manner and can be approximated using the double-couple model (Aki & Richards, 2002, Stein & Wysession, 2003). The double-couple describes the radiation of P- and S-waves whose quadrupole radiation patterns are
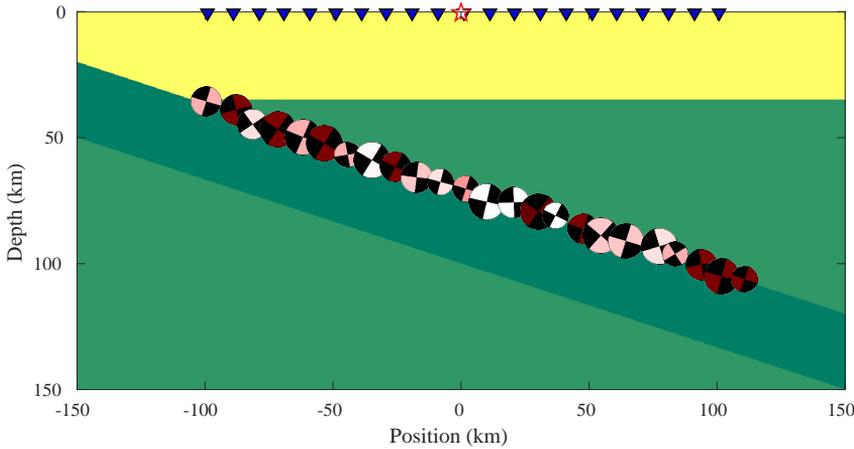
Figure 3.1: *Elastic subduction-zone model based on results from Chen et al. (2015): Yellow indicates the crust, green the mantle and darkgreen the subduction slab. Sources are indicated by beachballs (see Figure 3.2), receivers as blue inverted triangles and the virtual source position we show results for is indicated by the red star.*
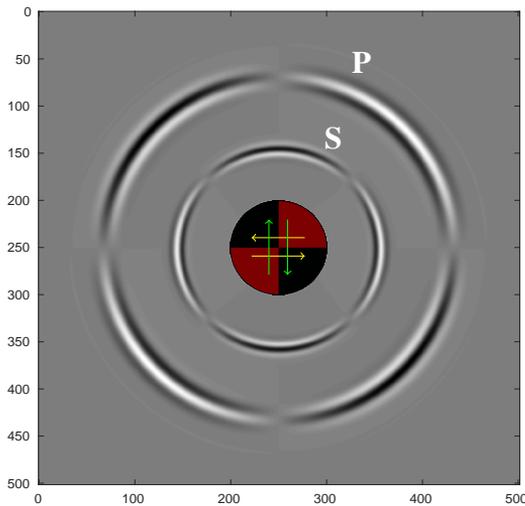


Figure 3.2: *2D snapshot of P- and S-wave radiation from the double-couple model we implemented to obtain the synthetic recordings. The horizontal and vertical axes indicate the number of gridcells which have a size of 200 m.) The yellow and green arrows indicate the two possible fault-slip motions which can both generate this specific elastodynamic radiation pattern. The beachball in the middle is the symbol we use in Figure 3.1 to denote the position, orientation and peak frequency of the double-couples. We use black to denote compression, which has positive amplitude. Dilatation, which has negative amplitude, is denoted with a varying colour to indicate the peak frequency of the source wavelet, which varies from dark red (0.4 Hz) to white (1 Hz).*

rotated 45 degrees with respect to each other (Figure 3.2). We distribute a total
number of 70 shear-stress sources irregularly along the top of the subducting slab
to simulate the effect of stress-release induced by tectonic forces. The source mech-
anisms vary randomly in peak frequency (between 0.4 and 1 Hz), orientation (be-
tween 0 and 360 degrees) and an amplitude factor (3-5). We use a Ricker wavelet
as source function. The bandlimiting properties of this particular source function
prevent aliasing of the synthetic wavefields, which can be achieved for the case of
real data by applying an appropriate bandpass filter.

### 3.3.1. PROCESSING

Ballistic and full-field MDD require an estimation of the elastodynamic $\hat{V}^o$ field
that defines the earthquake recording without free-surface multiples. We obtain an
approximation of the elastodynamic $\hat{V}^o$ response of each independent earthquake
recording in the time-domain (Figure 3.3a) by selecting one half of the direct P-
and S-wave with a tapered time-window (Figure 3.3b). This wavefield is the time-
domain representation of $\hat{V}^D$, which serves to approximate the $\hat{V}^o$ field (equation
(3.6)). For SI by crosscorrelation, approximate Green's functions are obtained by
a straightforward crosscorrelation of the earthquake recordings. In turn, ANSI-
MDD requires the resulting crosscorrelation functions as input (see Figure 3.3c).
In order to construct the PSF in equation (3.11), the virtual source functions are
extracted from the crosscorrelation functions by applying a time-symmetric tapered
time-window that only selects the part of the crosscorrelation function between, and
including, the causal and acausal virtual direct P-wave arrival. We do not select the
virtual direct S-wave arrival because this would inevitably include parts of virtual
primary reflections in the PSF, which would increase the appearence of artefacts
in the final result. Figure 3.3d shows an example of a PSF that was obtained by
applying the tapered time-window to the crosscorrelation function shown in Figure
3.3c.

### 3.3.2. RESULTS

For 2D media, each SI method produces four different elastodynamic responses.
Here we analyze only two types of elastodynamic responses per SI method: the
vertical and horizontal particle-velocity responses due to a horizontally oriented
point-source (positioned at the middle receiver). Note that full-field MDD retrieves
virtual responses to a simple-shear point-source (quadrupole) oriented with respect
to the acquisition surface without free-surface multiples, while the other three meth-
ods retrieve virtual responses to a horizontal force point-source (dipole) with free-
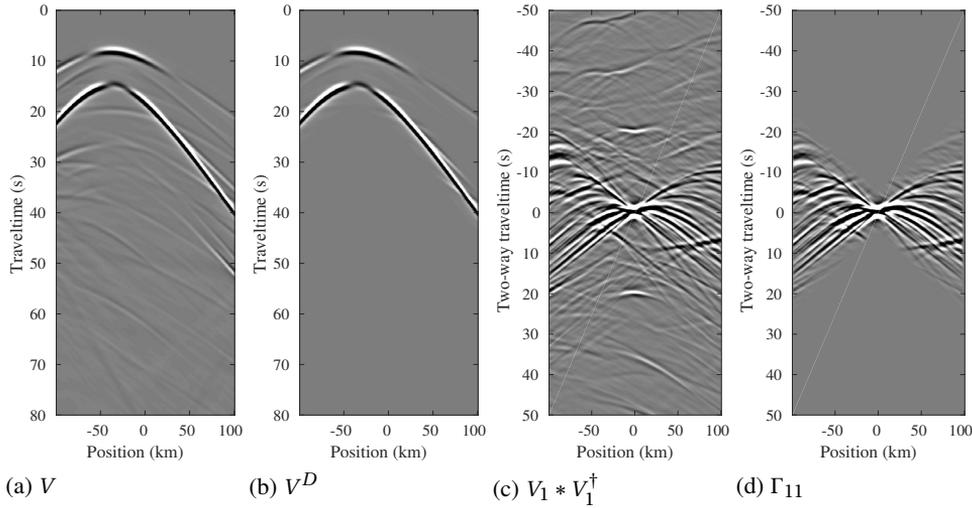surface multiples.

Figure 3.3: *SI processing.* **(a)** *Example of one of the independent synthetic earthquake recordings.* **(b)** *The $V^D$ approximation: the $V^o$ field is estimated by selecting the direct P- and S-wave, which are multiplied by one half, of the recording in Figure (a).* **(c)** *Crosscorrelation function forms the input for ANSI-MDD.* **(d)** *The PSF of equation* (3.11) *selected by a tapered time-window from the crosscorrelation function shown in Figure (c).*

Figure 3.4c shows the vertical particle-velocity reflection response and Figure 3.4h shows the horizontal particle-velocity response to a shear-stress source at the middle receiver, serving as reference responses to assess the quality of the reflection retrieval of each method. In these reference responses, the PP, SS and PS/SP reflections of the Moho are identifiable (indicated by yellow arrows). As for the reflections from the top and bottom of the subduction slab, we only focus on their respective PP, SS and PS-converted reflections (top reflections are indicated by green and bottom reflections by blue arrows).

The results from crosscorrelation (equation (3.1)) are shown in Figures 3.4a and 3.4f. In comparing these results to their corresponding reference responses, most of the arrivals are correctly retrieved, although we do observe a lower frequency content and a significant number of artefacts. In spite of this, some relevant features can still be distinguished, for example, the near-offset AVO behaviour of the Moho's PP and PS reflections in Figure 3.4a is accurately reconstructed, as well as the Moho's SS reflection in Figure 3.4f.

Figures 3.4b and 3.4f correspond to the results obtained by ANSI-MDD. The retrieval of the reflections has improved when compared to the corresponding crosscorrelation results (Figures 3.4a and 3.4f). However, the inversion proved unstable:
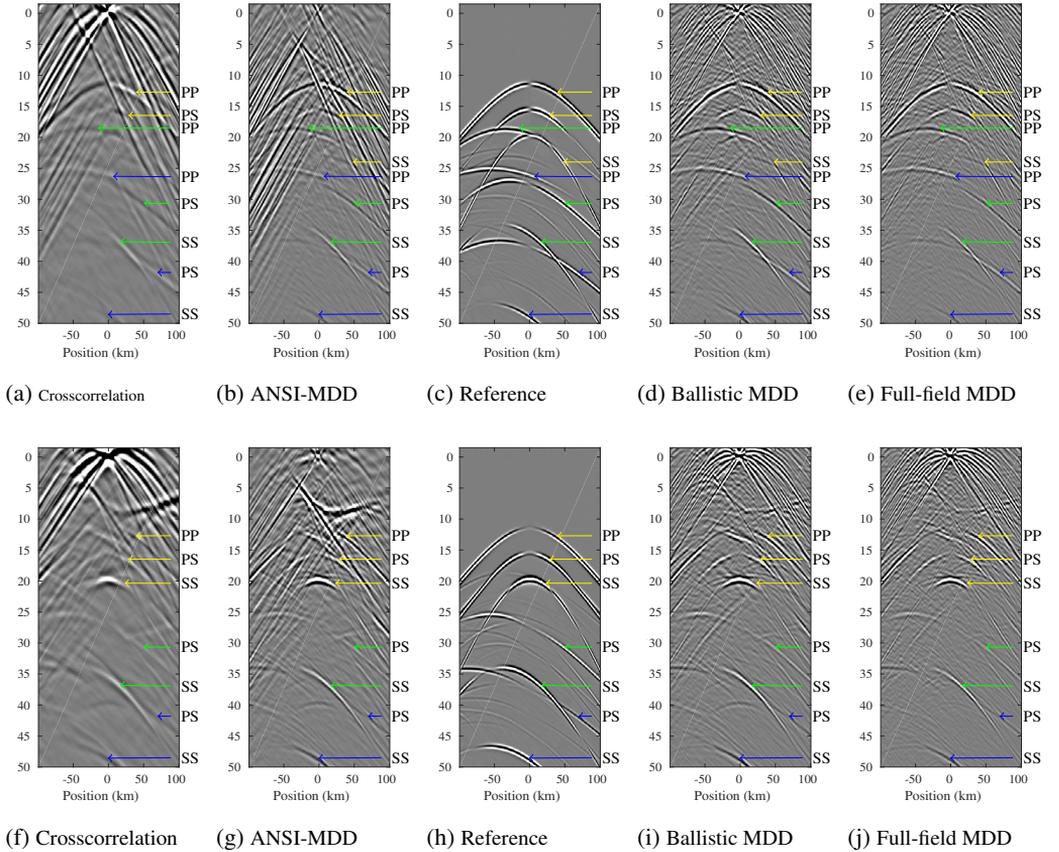
(a) Crosscorrelation    (b) ANSI-MDD    (c) Reference    (d) Ballistic MDD    (e) Full-field MDD

(f) Crosscorrelation    (g) ANSI-MDD    (h) Reference    (i) Ballistic MDD    (j) Full-field MDD

Figure 3.4: *Virtual reflection responses obtained with the SI methods from recordings of double-couples. The horizontal axis denotes two-way travel time in seconds.* **(a)** *Vertical particle-velocity response to a horizontal dipole by crosscorrelation,* $R_{3|1}$. **(b)** *Idem as (a) by ANSI-MDD.* **(c)** *Reference vertical particle-velocity reflection response to a shear-stress source,* $R_{3|13}^{o}$. **(d)** *Idem as (a) by ballistic MDD.* **(e)** *Vertical particle-velocity response to a shear-stress source by full-field MDD,* $R_{3|13}^{o}$. **(f)**-**(j)** *similar to* **(a)**-**(e)**, *but for horizontal particle-velocity.*

strong artefacts still partially obscure the reflections, while a stabilization parameter of 80% of the maximum absolute value of the corresponding PSF was required. We also observed that the results were highly sensitive to the time limits of the PSF selection window: we needed to manually adjust the limits of the time-window in order to obtain acceptable results.

For the other two methods, ballistic and full-field MDD, we employ equations (3.10) and (3.13), respectively, to obtain their reflection responses. The results of ballistic (Figures 3.4d and 3.4i) and full-field MDD (Figures 3.4e and 3.4j) are significantly better resolved and feature less artefacts than the results obtained by crosscorrelation and ANSI-MDD. These figures show that all events visible in the reference responses are also visible in both the MDD results, with the same high resolution. Most of the AVO features are accurately resolved, such as the PP Moho reflection in Figures 3.4d and 3.4e and the SS Moho reflection in Figures 3.4i and 3.4j. Both methods required little stabilization: 4% for ballistic MDD and 3% for full-field MDD.

The ballistic MDD equation (3.10) and the full-field MDD equation (3.13) contain the $\hat{\mathbf{V}}^o$ field that we estimate using the direct P- and S-arrival: $\hat{\mathbf{V}}^D$ (see Figure 3.3b). In order to better understand the sensitivity of the ballistic and full-field MDD methods to the accuracy of the $\hat{\mathbf{V}}^D$ approximation, we show additional solutions in Figure 3.5 for which we only used the direct P-wave for $\hat{\mathbf{V}}^D$. Figures 3.5a and 3.5b show that exluding the direct S-wave from $\hat{\mathbf{V}}^D$ does not strongly affect the result: only the slab reflections are more difficult to discern in Figure 3.5b. However, in case of the horizontal particle-velocity response the Moho reflections also become less clear (Figure 3.5g). The effect of omitting the direct S-wave from $\hat{\mathbf{V}}^D$ is much more severe in the case of ballistic MDD: the results shown in Figures 3.5e and 3.5j are both seriously contaminated by artefacts and do not resemble the results in Figures 3.5d and 3.5i.

## 3.4. Discussion

The crosscorrelation results in Figures 3.4a and 3.4f have a lower quality than those of full-field and ballistic MDD. This can be explained by the fact that the crosscorrelation equation (3.1) is designed for smoothly distributed passive sources with constant isotropic radiation patterns. Because of this, it cannot be expected to adequately correct for the highly anisotropic radiation patterns of double-couples with varying source characteristics (Figure 3.2). Moreover, equation (3.1) shows that crosscorrelation will yield a reflection response estimate that is convolved with the average of the earthquakes' spectra, S. Therefore, the resolution of the reflection response is largely determined by the peak frequencies of the earthquakes' source
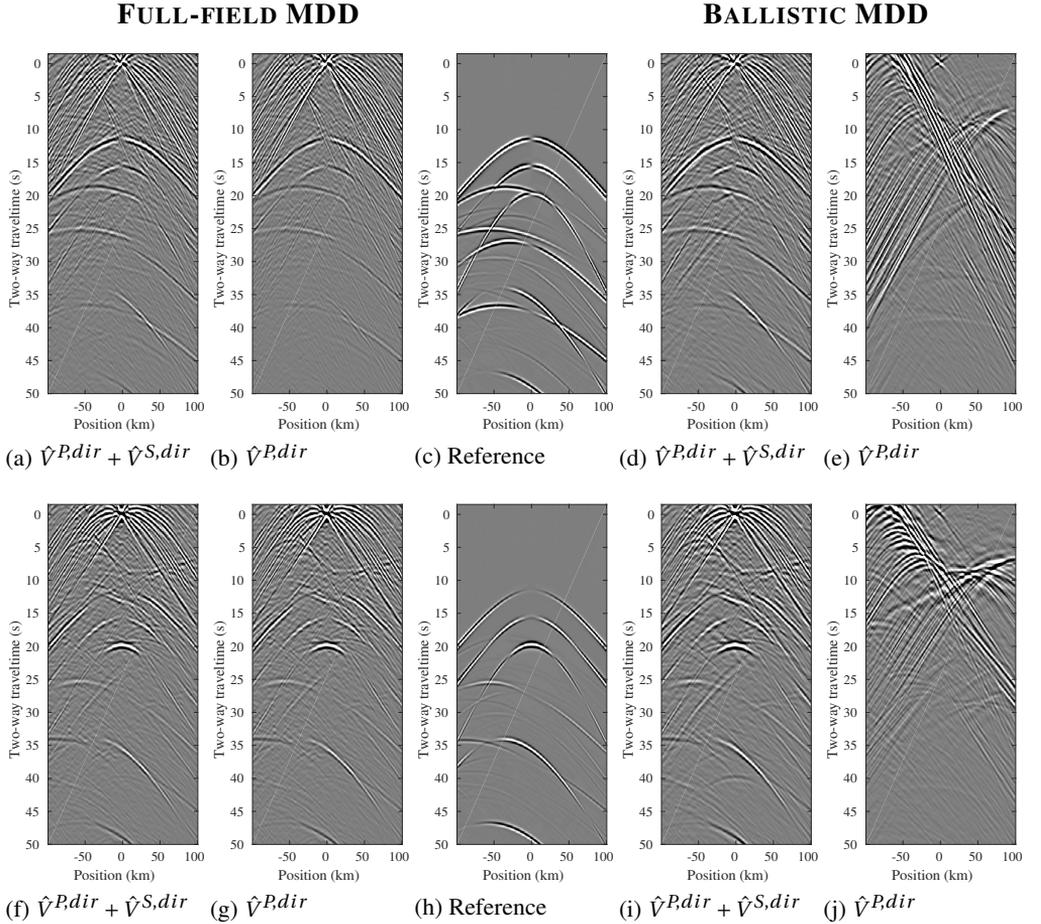
**FULL-FIELD MDD**                    **BALLISTIC MDD**



Figure 3.5: *Ballistic and full-field MDD results using two different $\hat{V}^D$ approximations to estimate the $\hat{V}^o$ field. (**a**) Full-field MDD result $R^o_{3|13}$ using $\hat{V}^D = \frac{1}{2}\hat{V}^{P,dir} + \frac{1}{2}\hat{V}^{S,dir}$. (**b**) Full-field MDD result $R^o_{3|13}$ using $\hat{V}^D = \frac{1}{2}\hat{V}^{P,dir}$. (**c**) Reference vertical particle-velocity reflection response to a shear-stress source, $R^o_{3|13}$. (**d**) Ballistic MDD result $R_{3|1}$ using $\hat{V}^D = \frac{1}{2}\hat{V}^{P,dir} + \frac{1}{2}\hat{V}^{S,dir}$. (**e**) Ballistic MDD result $R_{3|1}$ using $\hat{V}^D = \frac{1}{2}\hat{V}^{P,dir}$. (**f**)-(**j**) similar to (**a**)-(**e**), but for horizontal particle-velocity.*

functions. On the other hand, the deconvolution process of the MDD methods results in a flattening of the spectrum of the final solution. Hence, these methods exploit the full frequency band as provided by the natural illumination.

Figures 3.4b and 3.4g show that the elastodynamic form of ANSI-MDD primarily improves the resolution of the crosscorrelation results. However, the use of a very high stabilization parameter of 80% did not prevent the reflections to become partially obscured by inversion-related artefacts. This shows that the inversion is unstable. Another disadvantage of the ANSI-MDD method is that the solution is highly sensitive to the user-dependent process of selecting the PSF with a time-window from the crosscorrelation functions. This will particularly cause problems in the case of field data, when it is more challenging to adjust the limits of the PSF selection window to obtain optimal results. Hence, for transient-source responses we do not recommend to use the ANSI-MDD method, but for ambient noise it is the only MDD method and hence worth to be further investigated.

The application of full-field and ballistic MDD resulted in more stable and accurate estimates of virtual body-wave reflections. However, Figures 3.5e and 3.5j show that when the direct S-wave, $\hat{V}_j^{S,dir}$, is omitted from the $\hat{\mathbf{V}}^D$ approximation, the ballistic MDD results become severely contaminated by artefacts. The full-field MDD results are considerably less affected by this (Figures 3.5b and 3.5g). The fact that the PSF of ballistic MDD is constructed by the $\hat{\mathbf{V}}^D$ field (see equation (3.10)) could explain its higher sensitivity to the accuracy of the $\hat{\mathbf{V}}^D$ approximation. By omitting $\hat{V}_j^{S,dir}$, the ballistic PSF loses its ability to correct for irregularities in the illumination provided by the directly incident S-wavefield. Moreover, this omission has as a result that the free-surface multiples in the earthquake recordings that are initiated by direct S-waves cannot be explained and therefore generate artefacts. On the other hand, changes in this approximation have no effect on the PSF of full-field MDD since it is constructed by the observed data (equation (3.13)). This implies that in cases where it is too challenging to extract the direct S-wave from field data recordings, it suffices to use only the direct P-wave for the full-field MDD method to obtain a stable result.

The elastodynamic reflections we estimate with either full-field or ballistic MDD can be used directly to estimate P- and S-wave velocities or relevant subsurface structures such as the depth of a subducting slab. The accuracy of the AVO reconstruction we observe in the MDD results indicates that it may be possible to perform an elastodynamic AVO analysis on virtual body-wave reflections in order to determine valuable petrophysical parameters such as the presence of partial melts or water. However, this would require full illumination conditions and proper spatial sampling of the recordings. Furthermore, these virtual reflections are a useful

input for a myriad of tomographic and full waveform inversion schemes, especially considering that MDD methods do not require any knowledge of earthquake source mechanisms, timings nor locations. Another possible application would be to use the complete virtual seismic surveys as input for exploration imaging techniques. These operations can yield a complete image of the subsurface with maximum vertical resolution and can additionally minimize the effect of interferometric artefacts.

## 3.5. CONCLUSION

We applied four different seismic interferometry methods to synthetic particle-velocity responses of double-couples distributed throughout a 2D elastic subduction-zone model. When compared to crosscorrelation and the approximated form of ballistic MDD (ANSI-MDD), our results indicate that both the full-field and ballistic multidimensional deconvolution (MDD) methods provide more accurate and stable solutions with the least number of artefacts under these circumstances. Essential characteristics of the retrieved reflections, such as the arrival time and amplitude-versus-offset (AVO) behaviour, resembled those of the reference responses. Moreover, further analysis revealed that the full-field MDD method is less sensitive to the required estimation of earthquake recordings without free-surface multiples ($V^o$) than ballistic MDD.

# 4

# IMPLICATIONS OF MULTIPLE SCATTERING FOR PASSIVE SEISMIC INTERFEROMETRY

*Previous research has shown that a higher scattering potential improves the Green's function estimated by crosscorrelation seismic interferometry (SI) when passive source illumination is inadequate. This clause is analyzed in this study by applying SI by crosscorrelation to simple models with an increasing scattering potential that we quantify with a scattering coda diffusion equation. Multidimensional deconvolution (MDD) methods are included in the analysis. Although it can be expected that MDD profits in a similar way from scattering as crosscorrelation, certain assumptions that MDD relies on become less valid with increasing scattering potential. The results indicate that there exists a trade-off between the quality of the virtual reflection estimate that can be obtained by SI and the scattering potential of the medium. On the one hand, scattering generates low wavenumbers that can help to improve the retrieval of the reflection response in the case of limited illumination. On the other hand, not all SI methods can equally benefit of scattering, because it also increases the complexity of the illuminating wavefield. The full-field MDD methods seems to be most effective in correcting for the observed negative effect of multiple scattering.*

## 4.1. Introduction

Earthquake hypocenters generally concentrate around active plate boundaries such
as subduction zones and orogenies. The resulting sparse distribution of earthquakes
poses a challenge for seismic interferometry (SI) to estimate virtual body-wave re-
flections. When the array is not located within the area of the epicenter, the record-
ings may be less dominated by events that are within the Fresnel zone with respect
to the array. These stationary-phase events are required to obtain a reliable Green's
function estimate (Snieder, 2004). Many studies have shown that multiple scatter-
ing positively influences the reconstruction of the Green's function by crosscorre-
lation (Derode et al., 2003, van Tiggelen, 2003, Malcolm et al., 2004). Even un-
der limited illumination conditions, sufficiently long recordings of scattering coda
can provide the required stationary-phase events (Campillo & Paul, 2003, Larose
et al., 2004a, Campillo, 2006). On the other hand, numerical acoustic results from
Hartstra & Wapenaar (2015) indicated that scattering may also increase the num-
ber of artefacts in the crosscorrelation results that obscure the retrieved reflections
considerably. This implies that multiple scattering may pose a trade-off for the per-
formance of seismic interferometry. Considering that the crustal lithosphere has a
significant scattering potential, that is especially high in tectonically active areas
(Sato et al., 2012), this trade-off is nontrivial for real data applications.

For the performance of multidimensional deconvolution (MDD) methods, multi-
ple scattering may pose a disadvantage as well, but for a different reason. MDD
methods rely on an acceptable estimation of the earthquake recordings without free-
surface multiples: the $V^o$ field (see Chapters 2 and 3 for further details). When the
medium is not known, the only plausible estimation of the $V^o$ field can be made
by approximating it by the direct wave of the passive recording, since removing
free-surface related multiples from passive data is very challenging. This approx-
imation is acceptable in case the medium has a relatively low scattering potential,
because the difference between the passive recording and the reference recording
will be minimal (Wapenaar et al., 2008b). However, with increasing scattering po-
tential, relatively more energy becomes contained in the internal multiples, which
we cannot extract from the earthquake recordings. Therefore, the direct wave ap-
proximation of the $V^o$ is expected to become less reliable with increasing scattering
potential, which has a negative effect on the stability of the inversion that underlies
MDD methods.

The effect of multiple scattering on the performance of SI methods is analyzed for
the case when passive source illumination is limited to high wavenumbers. The
case of full illumination is analyzed as well in order to isolate the effects of scatter-
ing from sparse illumination effects. The numerical simulations are conducted in

the elastic regime, because PS converted waves play a significant role in multiple scattering (Snieder, 2002). The scattering potential is effectively varied by increasing the number of scatterers in the crustal lithosphere of the model. The scattering potential of each model is determined by estimating the diffusivity from the decay of the recorded scattering coda energy.

### 4.1.1. RADIATIVE TRANSFER THEORY

The reason why interferometry can benefit of multiple scattering lies in the ability of a heterogeneity to act as a secondary source, generating a particular 'scattering radiation pattern' that is a function of its size and elastic properties. When the size of the heterogeneities is less than a tenth of the wavelength, multiple scattering is classified as 'Rayleigh scattering', while 'Mie scattering' occurs when the size is in the order of the dominant wavelength (Wu & Aki, 1985). Rayleigh scattering produces a more isotropic scattering radiation pattern, while the resonance effects associated with Mie scattering result in a considerably more complex radiation. When the incident coherent wave field impinges on heterogeneities in the medium, it will gradually transform into a diffusively propagating wavefield due to multiple scattering. This diffusive behaviour can be recognized on the macroscopic scale by the decaying coda that follows the first arrivals on a seismic recording. Because of that, it is possible to infer the scattering potential of a medium from the recordings at the surface (Sato et al., 2012). The diffusivity coefficient, $D$, that controls the energy decay of the wavefield on a macroscopic scale, is related to the scattering density on a mesoscopic scale via the scattering mean free path, $l$, as follows (Paasschens, 1997):

$$D = \frac{cl}{d},$$

(4.1)

where $d$ signifies the spatial dimensionality of the medium and $c$ the average propagation velocity of the background medium. The mean free path is a measure of the inverse scattering density of the medium: a smaller mean free path value means a higher scattering potential. While the radiative transfer equation provides the most accurate description of the decay of energy due to multiple scattering, for the larger time limit ($T \gg \frac{l}{c}$), the diffusion equation provides an accurate description as well (Wegler et al., 2006). The diffusion equation from Paasschens (1997) describes how the scattering energy decay depends on the scattering density of the medium via the diffusivity coefficient:

$$P(r,t) = \frac{1}{(4\pi Dt)^{d/2}} \exp\left(-\frac{r^2}{4Dt} - \frac{ct}{l_a}\right), \tag{4.2}$$

where $r$ is the distance between the source and receiver, and $l_a$ is the intrinsic absorption length. When we substitute equation (4.1) and apply the 2D spatial dimension ($d = 2$), this equation becomes:

$$P^{2D}(r,t) = \frac{1}{(2\pi clt)} \exp\left(-\frac{r^2}{2clt} - \frac{ct}{l_a}\right). \tag{4.3}$$

**4**

This equation shows that in case of stronger scattering, the mean free path, $l$, and diffusivity, $D$, are smaller. A smaller diffusivity means a slower decay of the wavefield energy. From a physical perspective, this can be explained by the fact that scattering causes the wavefield to remain confined to the scattering zone for a longer time. The conventional spatial energy loss by geometrical spreading is therefore slowed down by the presence of scatterers. Another physical effect that could explain the slower decay with smaller distance between scatterers is the coherent backscattering enhancement or weak localization that is a result of the constructive interference of scattered waves (Campillo & Paul, 2003, Larose et al., 2004b). However, more scattering also means a larger cumulative propagation distance, which in case of intrinsic attenuation will result in a stronger decay. Since the relation between instrinsic and scattering attenuation is complex (Haney et al., 2005), the effects of intrinsic attenuation are neglected in this study.

## 4.2. NUMERICAL RESULTS

The elastic model used for the numerical simulation consists of a simple lithospheric model containing a horizontal Moho reflector of 50 km depth separating the crust and mantle. The crust has P- and S-wave velocities of 6 km s$^{-1}$ and 3.5 km s$^{-1}$ respectively and a density of 2700 kg m$^{-3}$. The denser mantle material has P- and S-wave velocities of 9 km s$^{-1}$ and 4.5 km s$^{-1}$, respectively, and a density of 3400 kg m$^{-3}$. Different numbers of crustal scatterers with a diameter of 2 km are introduced to create models with various scattering potentials. The scatterers have a lower P- and S-wave velocity and density than the crust: 5.5 km s$^{-1}$, 3.3 km s$^{-1}$ and 1500 kg m$^{-3}$, in that order. With a dominant peak S-wavelength of 3.2 km and P-wavelength of 5.5 km, the scatterers will generate a wavefield that is expected to be dominated by Mie scattering (Wu & Aki, 1985).
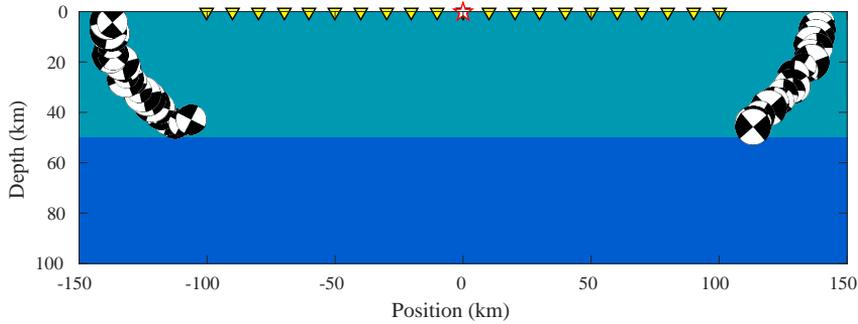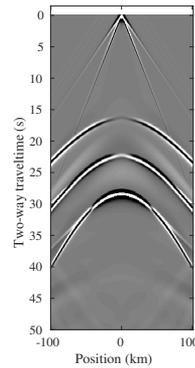
(a)
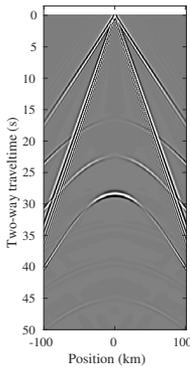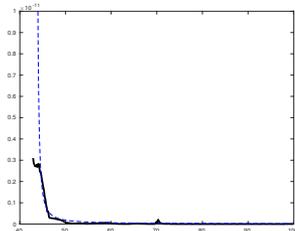


(b)                                    (c)                                    (d)

Figure 4.1: *Homogeneous lithosphere.* *(a) Velocity model. The orientation and location of the passive double-couple sources are denoted by the beachballs (see Figure 3.2), the receivers by yellow inverted triangles and the virtual source position by the red star. The position along the horizontal axis corresponds with the horizontal axis of the modelled and retrieved shot gathers. (b) Modelled horizontal particle-velocity reflection response of the medium with free surface (FS) obtained by implementing a double-couple source placed at the the position of the middle receiver. (c) Intensity averaged over all receivers due to a source placed in the middle of the model at position 10 km and depth 50 km. The curve fit of equation (4.3), denoted by the dashed line, yielded a mean free path value of 15 km. (d) Same as (b), but without free surface.*
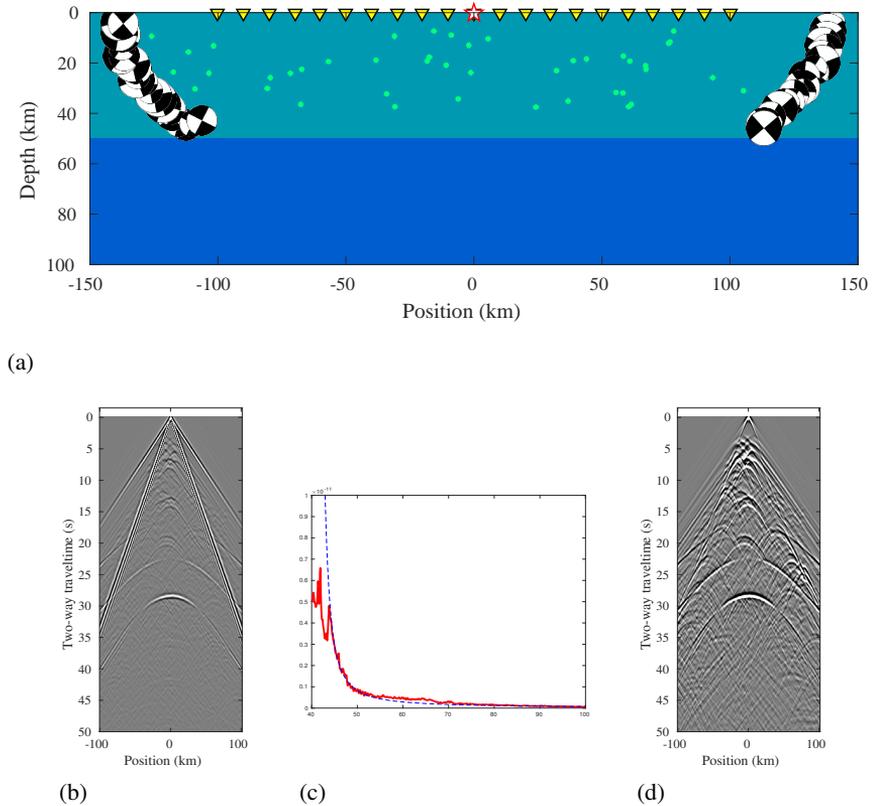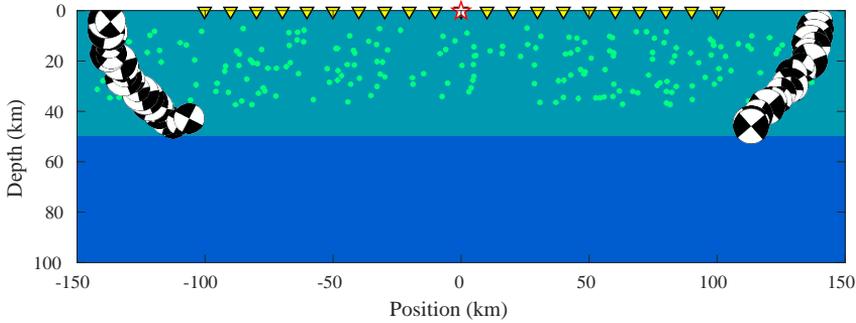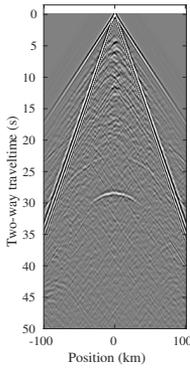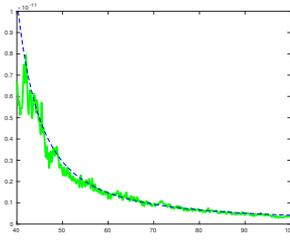
4



(a)



(b)                    (c)                    (d)

Figure 4.2: *50 crustal scatterers.* (**a**) *Same as Figure 4.1a, but with 50 crustal scatterers of 5.5 km* $s^{-1}$ *and 3.3 km* $s^{-1}$ *P-wave velocity and S-wave velocity, respectively, and 1500 kg* $m^{-3}$ *density.* (**b**) *Modelled horizontal particle-velocity reflection response of the medium with free surface obtained by implementing a double-couple source placed at the the position of the middle receiver.* (**c**) *Intensity averaged over all receivers due to a source placed in the middle of the model at depth level 50 km. The curve fit of equation (4.3), denoted by the dashed line, yielded a mean free path value of 4 km.* (**d**) *Same as (b), but without free surface.*

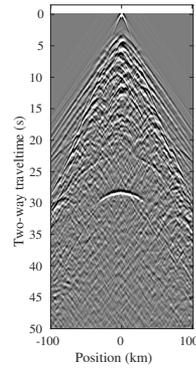(a)



(b)                                    (c)                                    (d)

Figure 4.3: *200 crustal scatterers. (**a**) Same as Figure 4.1a, but with 200 crustal scatterers of 5.5 km s$^{-1}$ and 3.3 km s$^{-1}$ P-wave velocity and S-wave velocity, respectively, and 1500 kg m$^{-3}$ density. (**b**) Modelled horizontal particle-velocity reflection response of the medium with free surface obtained by implementing a double-couple source placed at the the position of the middle receiver. (**c**) Intensity averaged over all receivers due to a source placed in the middle of the model at depth level 50 km. The curve fit of equation (4.3), denoted by the dashed line, yielded a mean free path value of 1 km. (**d**) Same as (b), but without free surface.*

The first model is defined by a homogeneous lithosphere (Figure 4.1a), the second contains 50 spherical crustal scatterers with a lower velocity (Figure 4.2a) and the final model contains 200 scatterers of the same type (Figure 4.3a). The modelling is performed in the elastodynamic regime in order to take into account the effect of P-SV conversions. This also allows for the implementation of sources that generate both P- and S-wave polarizations with the double-couple source type that represents the radiation of fault-slip movement (Figure 3.2 in Chapter 3). In order to minimize the effect of irregular source illumination, the peak frequency is a constant 1.1 Hz for all sources.   The horizontal and vertical particle-velocities are recorded by 200 receivers with a spacing of 1 km. Elastodynamic crosscorrelation, full-field MDD, ballistic MDD and ANSI-MDD are applied to estimate the reflection responses to the virtual source. Considering that these SI methods strive to estimate lower wavenumber reflections from the passive recordings, the high wavenumber dominated illumination we deal with here is particularly challenging.

The modeled response to a source implemented at the virtual source position, for both free-surface and absorbing boundary conditions at the acquisition level, serves as a reference. These reference responses show that as the scattering potential of the crust increases, the wavefield becomes more complex due to the diffractions that in turn cause the primary reflections to be less visible (Figures 4.1d, 4.2d and 4.3d). In the case of a free surface boundary condition at the receiver level, the primary reflections are in general more obscured due to the appearance of surface waves, which geometrically decay at a lower rate than body waves (Figures 4.1b, 4.2b and 4.3b).

### 4.2.1. Scattering analysis

In Figure 4.4a we analyze the single trace recording for each of the three models at receiver position −50 km of a passive double-couple source inside the medium at spatial coordinates (−2,46). Clearly, a higher scattering potential results in the development of a more complex and energetic coda. We employ the 2D diffusion equation (4.3), to estimate the scattering potential of each model. The average intensity variation as a function of time is calculated for each of the three model examples by using all trace recordings from the same passive source at coordinates (−2,46) (Figure 4.4b). Note that a single trace suffices for this calculation, but by averaging over all available receivers we can obtain a more complete spatial sampling of the scattering slab. By varying the diffusivity value $D$, equation (4.3) can be adjusted to obtain an appropriate fit of the intensity curve of each different model. A different diffusivity value is required for each modeled scattering potential (Figure 4.1c, 4.2c and 4.3c). As the theory predicts, a larger number of scatterers results
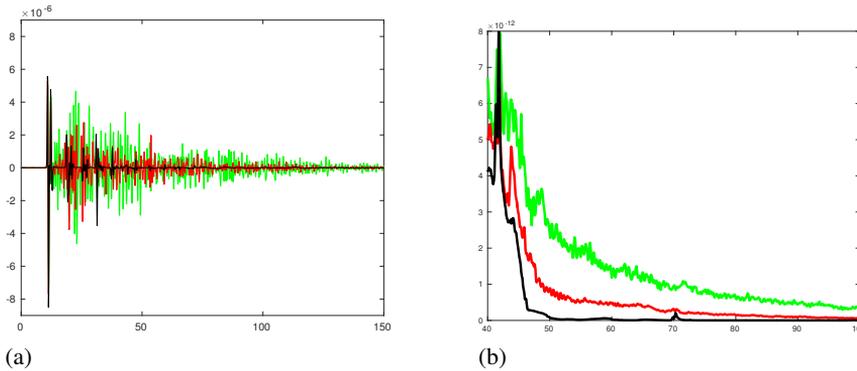
(a)  (b)

Figure 4.4: *Analysis of the scattering effects of the three different models due to a single passive source implemented at coordinate position (−2,46) km. Black curve indicates model with homogeneous crust in Figure 4.1a. Red curve indicates model with 50 crustal scatterers in Figure 4.2a. Green curve indicates model with 200 crustal scatterers in Figure 4.3a. (a) Vertical particle-velocity recording at the receiver positioned at -50 km. (b) Energy intensity as a function of time averaged over all available trace recordings.*

in a smaller mean free path and conversely, a lower diffusivity value. In case of a homogeneous crust, the best fit of equation (4.3) is obtained with $l = 15$ km and $D = 24.8$ km$^2$ s$^{-1}$. When the scattering potential is increased, the mean free path $l$ diminishes to 4 km and $D$ to 6.6 km$^2$ s$^{-1}$. The mean free path and diffusivity are 1 km and 1.65 km$^2$ s$^{-1}$, respectively, in case of the largest scattering potential. This indicates that for the type of scatterers implemented here, the $l$ is about a third of the average distance between scatterers.

### 4.2.2. LIMITED ILLUMINATION

In order to simulate the situation of sparse illumination the passive sources are restricted to the outer sides of the model as shown in Figure 4.1a. This ensures that the direct incident waves do not provide lower wavenumbers to the virtual source position that is chosen here to be in the middle of the array.

In the case of a homogeneous lithosphere, none of the methods are able to estimate the lowest wavenumbers of the primaries (Figures 4.5b - 4.5e). The result of ballistic MDD in Figure 4.5d is especially dominated by artefacts, because it attempts to obtain virtual reflections from first order free-surface multiples that are directly initiated by the ballistic field. These free-surface multiples are hardly available under these illumination conditions. For example, the PS primaries are correctly obtained for offsets larger than about 70 km absolute value, which could have been obtained from first order free-surface multiples. However, for smaller offsets the primary fol-
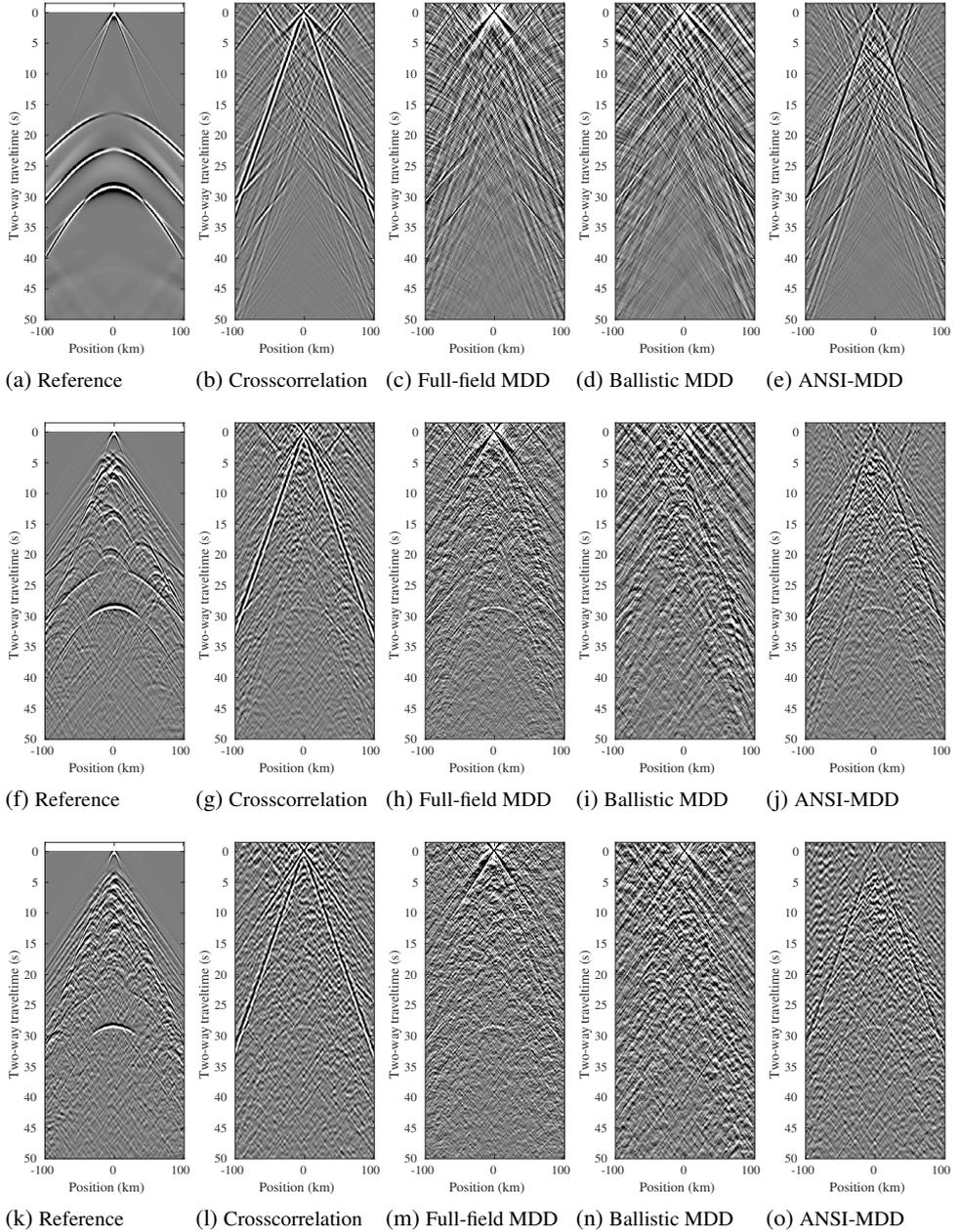
**4**



(a) Reference      (b) Crosscorrelation    (c) Full-field MDD    (d) Ballistic MDD    (e) ANSI-MDD

(f) Reference      (g) Crosscorrelation    (h) Full-field MDD    (i) Ballistic MDD    (j) ANSI-MDD

(k) Reference      (l) Crosscorrelation    (m) Full-field MDD    (n) Ballistic MDD    (o) ANSI-MDD

Figure 4.5: *Virtual reflection responses for the three different models. (**a**) Reference horizontal particle-velocity response to a horizontally oriented double-couple source located at the middle receiver position for the model without free surface in Figure 4.1a. (**b**) Horizontal particle-velocity response to a virtual horizontal source for model in Figure 4.1a estimated with crosscorrelation. (**c**) Same as (b), but with full-field MDD. (**d**) Same as (b), but with ballistic MDD. (**d**) Same as (b), but with full-field MDD. (**e**) Same as (b), but with ANSI-MDD. (**f**) - (**j**) same as (**a**) - (**e**), but for the model with 50 scatterers in Figure 4.2a. (**k**) - (**o**) same as (**a**) - (**e**), but for the model with 200 scatterers in Figure 4.2a.*

lows a straight continuous line that does not correspond to the two-way traveltime (TWT) values observed in the reference response (Figure 4.1b)), because these are artefacts. The crosscorrelation result shows sections of the SS primary reflection for offsets larger than about 40 km and the PS primary reflection for offsets larger than 70 km, but is also affected by artefacts (Figure 4.5b). Though it correctly retrieves the fundamental mode of the surface wave, this wave type does obscure the body wave reflections that are of interest. The ANSI-MDD result does not offer much improvement with respect to crosscorrelation (Figure 4.5e), but it does slightly diminish the surface wave. The virtual response estimated by full-field MDD reveals all three primary reflections in Figure 4.5c. Contrary to ballistic MDD, the primaries follow the correct TWT for offsets smaller than 70 km. In fact, the PS Moho primary is obtained for offsets as small as 40 km and the SS Moho primary for an even smaller offset of 30 km. The PP primary is more difficult to discern. This may be because PP scattering is less efficient that PS and SS scattering (Wu & Aki, 1985, Snieder, 2002). Note that the near-vertical incident reflections are not retrieved. Because full-field MDD obtains the reflections response without free surface effects, the surface wave is not retrieved. This allows the PP and PS body-waves to be more visible than in the case of the crosscorrelation.

When 50 circular scatterers are introduced in the lithosphere to mimic an intermediate scattering potential, more low wavenumbers events that are in stationary phase illuminate the array. The full-field MDD result in Figure 4.5h clearly shows that the SS Moho primary is now visible for very low offsets: even vertical incidence SV-wave reflections are retrieved. The PS Moho reflection is slightly better resolved and less obscured by artefacts than in Figure 4.5c. Figure 4.5a shows that the scattering almost completely obscures the visibility of the PP reflection. Therefore, it is no surprise that the virtual reflection response does not reveal it. Although of a slightly lower quality than the full-field MDD result, the crosscorrelation and ANSI-MDD methods also show the SS and PS Moho primaries (Figure 4.5g and 4.5j). This indicates that these methods also profit from the increased illumination provided by the crustal scattering. The ballistic MDD result in Figure 4.5i does not appear to have profited from stronger scattering, because the primaries are not visible at all.

When the scattering potential is further increased by implementing 200 crustal scatterers, the reference response in Figure 4.5k shows that the increased complexity of the overburden diminished the visibility of the Moho primaries. Full-field MDD result in Figure 4.5m still reveals the SS and PS Moho primaries, but the visibility is slightly decreased with respect to Figure 4.5h. Since this decreased visibility is also observed in the reference response (Figure 4.5k), this does not necessarily indicate a lower performance. The crosscorrelation, ballistic MDD and ANSI-MDD

methods hardly show a trace of any of the primaries (Figures 4.5l, 4.5n and 4.5o). A remnant of the near-offset section of the SS Moho primary appears to be slightly visible in Figures 4.5l and 4.5o, but this feature can be regarded too vague to discern from artefacts.
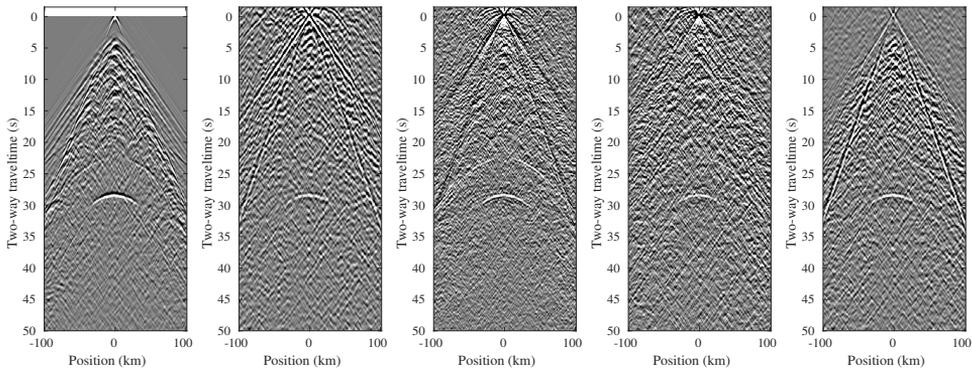
### 4.2.3. FULL ILLUMINATION

The results shown in Figure 4.5 only consider the effects of multiple scattering in the case of limited illumination. In order to establish the effect of multiple scattering without the negative impact of sparse illumination, a final numerical modeling experiment is conducted for the case of optimal illumination conditions. A total of 100 passive sources that surround the array are implemented in the model that has the maximum number of scatterers (Figure 4.6a). For this configuration, the result estimated with crosscorrelation shows a clearer SS Moho reflection (Figure 4.6c) than in the case of limited illumination (Figure 4.5l). On the other hand, the PS reflection that is clearly visible in the corresponding reference response in Figure 4.3b is not retrieved by crosscorrelation. Ballistic MDD and ANSI-MDD reveal remnants of the PS primary that are difficult to discern from the artefacts (Figures 4.6e and 4.6f, respectively). The full-field MDD result not only reveals an even clearer SS primary, it also reveals the PS primary that is as distinguished as the same reflection in the reference response in Figure 4.6b.

## 4.3. DISCUSSION

When passive illumination is limited to high wavenumbers, crustal scattering can improve SI results by complementing the limited illumination with lower wavenumbers. However, our results suggest that multiple scattering does not only benefit SI. Crosscorrelation and ANSI-MDD yielded acceptable results in the case of intermediate scattering (Figures 4.5g and 4.5j), but hardly showed a sign of primaries in the case of 200 scatterers (Figures 4.5l and 4.5o). The negative impact of scattering on the primary estimation was especially apparent for ballistic MDD (Figures 4.5i and 4.5n). This MDD method is strongly effected by the direct-wave approximation that is required to estimate $V^o$, because its PSF is constructed by this field. Therefore, ballistic MDD can only obtain primaries from free-surface multiples of the first order that are induced by waves directly incident from the source. Contrary to the other SI methods, the virtual responses estimated by the full-field MDD method did show visible primaries under all scattering conditions (Figures 4.5c, 4.5h and 4.5m). Different from ballistic MDD, the direct-wave approximation only affects the correlation function and not the full-field PSF, which is exact.
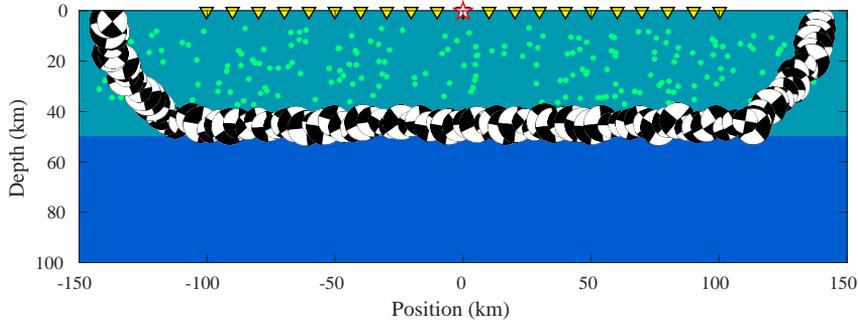
(a)

(b) Reference   (c) Crosscorrelation   (d) Full-field MDD   (e) Ballistic MDD   (f) ANSI-MDD

Figure 4.6: *Virtual reflection responses for the model with 200 scatterers and full illumination (**a**) The same model as in Figure 4.3a is used (**b**) Reference horizontal particle-velocity response to a horizontally oriented double-couple source located at the middle receiver position for the model without free surface. (**c**) Horizontal particle-velocity response to a virtual horizontal source estimated with crosscorrelation. (**d**) Same as (c), but with full-field MDD. (**e**) Same as (c), but with ballistic MDD. (**f**) Same as (c), but with ANSI-MDD.*

The results showed that an increasing scattering potential not only brought cross-correlation and ANSI-MDD more useful low wavenumber reflections to exploit, it also introduced significantly more artefacts (Figures 4.5l and 4.5o). One explanation for this increase in artefacts as a function of scattering potential, could be that the higher complexity of the medium also provides more opportunities for artefacts to be created. These additional artefacts cannot be cancelled out when we have limited passive source illumination. However, also in the case of full illumination (Figure 4.6c), the crosscorrelation results still appeared to be negatively affected by multiple scattering. The full-field MDD proved to be most effective in estimating the primaries in case of optimal illumination conditions: the results corresponded well to the reference response (Figure 4.6d). Considering that full-field MDD yields results of considerable higher quality than crosscorrelation (even in the case of optimal illumination), multiple scattering may give rise to other effects that can be corrected by full-field MDD but not by crosscorrelation or ANSI-MDD.

Artefacts may be caused by the fact that multiple scattering increases the complexity of the wavefield in several ways. For example, when a scatterer is considered that is very close to the virtual source position, this will give a high-amplitude stationary-phase event. On the other hand, a scatterer that is much deeper may also provide stationary events to the virtual-source position, though perhaps for a different angle. This latter stationary event has a lower amplitude than those provided by the scatterer closer to the virtual source position. Since the crosscorrelation method is unable to correct for the resulting anisotropic illumination, the scattering-induced anisotropy will be imprinted on the virtual source radiation pattern. Furthermore, the fact that the radiation pattern of a scatterer is similar to that of a source may also play a significant role in increasing the complexity of the scattered wavefield (Wu & Aki, 1985). In the elastic regime investigated here, scattering generates a complex elastodynamic radiation pattern that is comparable to the near-field pattern of an actual source. This scattered near-field pattern is a function of the incident wavetype, the elastic contrast and the size of the scatterer with respect to the wavelength. In the case of Rayleigh scattering, the density contrast of the scatterer generates a dipole radiation pattern, while the rigidity contrast generates a double-couple radiation pattern. Our models are dominated by Mie scattering. This type of scattering not only generates Rayleigh scattering radiation, but additionally generates phase interactions that result in an even more complex pattern characterized by features like small oscillatory side-lobes (e.g. Figure 26 in Wu & Aki (1985)). The snapshot in Figure 4.7a shows the S-potential of the radiation patterns that are generated by the interaction of the P-wave field with the scatterers. A scatterer that is close to the receivers will imprint the virtual source with its complex near-field radiation pattern, that crosscorrelation cannot correct for. Moreover, when the mean
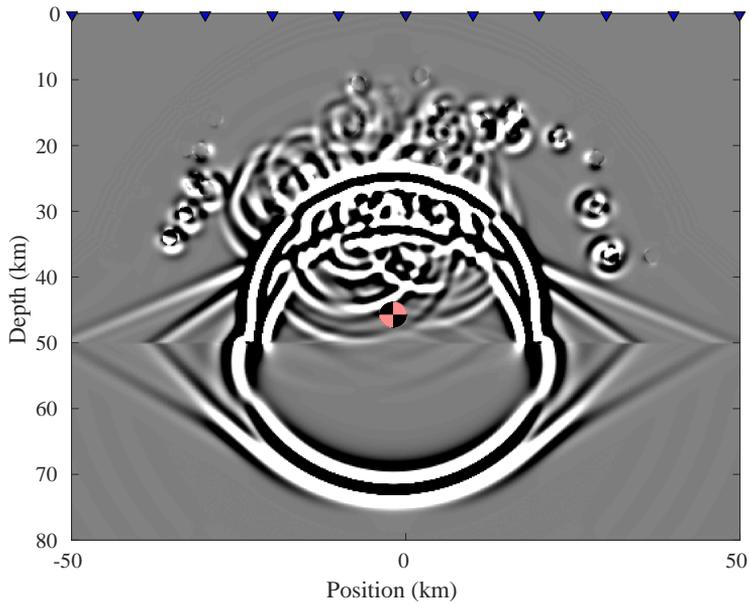
(a) 6 sec
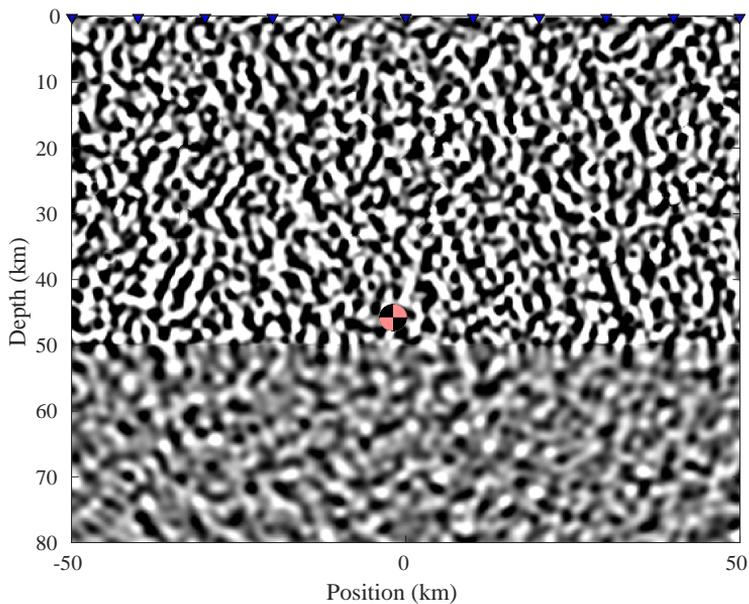


(b) 95 sec

Figure 4.7: *The S-potential response to a passive double-couple source positioned at coordinates (−2,46), that is denoted by the pink beachball, of the model with 200 scatterers (Figure 4.3a). (**a**) Snapshot after 6 seconds. (**b**) Snapshot after 95 seconds.*

free path becomes smaller, the likelihood of adjacent scatterer radiation patterns to interact becomes higher. The snapshot in Figure 4.7b shows that the complex interference effects caused by multiple scattering eventually become manifest over the entire extent of the model. The full-field PSF has the advantage that it encodes the anisotropic effects of the scattering-induced illumination as well and therefore has the potential to correct for any complex scattering effects. This may explain why the quality of Figures 4.5m and 4.6d are better than Figures 4.5l and 4.6c.

Our results imply that there exists a trade-off between the quality of the virtual reflection response that can be estimated by SI methods and the scattering potential of the medium. In turn, the diffusion equation shows that the diffusivity is directly related to the scattering potential and mean free path. This raises the question whether it may be possible to use a measure of the diffusivity to determine whether it is appropriate to apply SI methods in a certain area for a given frequency range. For example, when the mean free path has a value of 4 km at a peak frequency of 1.1 Hz (Figure 4.2a), except for ballistic MDD, all methods can be applied. While in the case of a smaller mean free path value of only 1 km (Figure 4.3a), it seems that only full-field MDD is suitable. However, 2D models are not appropriate to simulate the scattering potential that is observed in the real 3D medium (Sato et al., 2012). Equation (4.3) only describes the macroscopic behaviour as a function of the mean free path value that is inversely proportional to the scattering potential of the medium. Paasschens (1997) stressed that this equation does not entail multiple scattering interference effects that is part of the mesoscopic scale behaviour. These interference effects may play an important role for the ability of SI methods to utilize the increased illumination from scattering (Campillo, 2006). In order to use diffusivity to assess SI viability in an area, SI methods require to be tested under different scattering potentials in 3D models.

## 4.4. Conclusion

This study shows that there exists a trade-off between the scattering potential in an area and the ability of seismic interferometry (SI) methods to obtain primaries from scattering-induced illumination only. On the one hand, crustal scattering can complement limited high wavenumber illumination of the array by generating lower wavenumbers. On the other hand, the results showed that a higher scattering potential significantly decreased the quality of the primaries obtained by crosscorrelation, ballistic multidimensional deconvolution (MDD) and the MDD method adapted for ambient-noise SI (ANSI-MDD). Even in the case of full illumination, the crosscorrelation results were affected by multiple scattering. This lower performance may be for the reason that multiple scattering is also associated with the increase in arte-

facts and complex anisotropic illumination that can negatively impact SI. Since the full-field point-spread function (PSF) contains the complete spectral information of the correlation function it also has encoded the scattering-induced anisotropic illumination, which may explain why full-field MDD still revealed visible primaries under the strongest scattering conditions.

## 4.5. OUTLOOK

The numerical experiments also revealed that it is possible to quantify the scattering potential of a field setting using only a single trace recording. By performing a scattering coda decay analysis as a function of frequency, it may be possible to determine the dominant size of the heterogeneities that cause the coda to develop. Considering the differences in sensitivity of the SI method as a function of scattering, the analysis can also help to determine in which frequency range which method is most optimal for determining the desired primary reflections.

# 5

# ESTIMATING REFLECTIONS FROM SCATTERING CODA IN PELOPONNESUS, GREECE

*We demonstrate a real data example of the application of full-field multidimensional deconvolution (MDD) to obtain body-wave reflections. This method is suitable for real data because it involves the most stable inversion and it does not require wavefield decomposition However, the main strength of full-field MDD when compared to the ballistic MDD methods is that its PSF is exact: it is constructed by the full recorded wavefields. Our focus will be on obtaining reflections from the Moho or top of the crystalline basin due to their relatively high impedance contrasts. Local earthquakes are the most convenient type of source for this imaging target, due to their relatively high SNR and higher frequency content MDD can profit of. We decided to work with a dense array of broadband multicomponent receivers in the Hellenic zone, Peloponnesus, Greece. Our results show that full-field MDD provides virtual reflection responses with more distinct continuous features than the crosscorrelation methods. Especially the application of a rudimentary stacking procedure of NMO-corrected virtual responses indicates features that could be reflections of the Moho and crystalline basin.*

## 5.1. INTRODUCTION

Valuable information of the subsurface structure can be obtained from the scattered field of earthquake recordings by using seismic interferometry (SI) for body-waves.

There are many examples of body wave reflection estimation from field data using the crosscorrelation method (Wapenaar & Fokkema, 2006, Schuster, 2009): for this ambient noise measurements were used to obtain global phases (Roux et al., 2005, Nishida, 2013, Lin et al., 2013, Boué et al., 2014), scattering coda from local earthquakes (Tonegawa et al., 2009, Almagro Vidal, 2017) and many more examples (Draganov et al., 2007, Ruigrok et al., 2011). Crosscorrelation is a reliable method to estimate reflections when the passive source illumination of the array is known to be relatively isotropic and smooth. However, irregular source distributions, complex source mechanisms and scattering in the medium can cause the illumination to be irregular. The imprint of irregular illumination on the virtual source radiation pollutes the reflection estimates with artefacts.

Several methods have been developed with the purpose to balance the irregular illumination of the correlation gathers (Almagro Vidal et al., 2014, Curtis & Halliday, 2010). Multidimensional deconvolution (MDD) has the advantage that it inherently balances the irregularities during the inversion process that underlies this method (Wapenaar et al., 2008b, van der Neut, 2012). Besides, it also holds for dissipative media, while crosscorrelation does not. In spite of these advantages, there exist few examples of MDD applications to field data. The pioneering example of virtual body wave responses estimated by MDD from a field data set was conducted by Nakata et al. (2014). The authors applied ballistic MDD for decomposed one-way wavefields to estimate virtual reflections. As we discussed in detail in Chapter 3, the ballistic PSF needs to be approximated from the earthquake recordings by applying time-windowing. Here, the authors additionally applied elastodynamic wavefield decomposition to obtain a more accurate estimate, a delicate process that can be sensitive to medium parameter variations at the acquisition surface. Nishitsuji et al. (2016) applied the adapted version of ballistic MDD (referred to as ANSI-MDD in Chapter 3) from van der Neut et al. (2010) to field data, whereby the point-spread function (PSF) is selected postiori from the correlation gathers. When the PSF is selected correctly, this method can substantially improve the quality with respect to the original correlation gathers. However, the solution of ANSI-MDD is highly sensitive to the PSF selection and also requires a particularly large regularization parameter to stabilize the inversion. In the case of field data, it can be challenging to correctly callibrate the PSF selection and magnitude of the regularization parameter.

We aim to demonstrate a real data example of the application of full-field MDD (Hartstra et al., 2017, Almagro Vidal, 2017). We choose to use full-field MDD, because it involves a relatively stable inversion and it does not require wavefield decomposition, which can be affected when medium parameters change along the receiver array. However, the main strength of full-field MDD when compared to

the ballistic MDD methods is that its PSF is exact: it is constructed by the full recorded wavefields. This has the advantage that we invert a term that does not contain approximations. On top of that, a PSF that consists of the full correlation function has the potential to also correct for illumination irregularities caused by multiple scattering (see Chapter 4). The method still requires an estimation of the $V^o$ field, but the results in Chapter 3 showed that this method is not as sensitive to errors in this estimation as compared to ballistic MDD.

The quality of the final results strongly depends on the quality of the field data we use as input. For that reason, it is preferable to work with earthquake recordings that are characterized by a high signal-to-noise ratio, lower wavenumbers and a relatively high-frequency content. Although teleseismic events generate wavefields containing low wavenumbers, they lack high frequencies and sufficient signal-to-noise ratio due to dissipitation over the long propagation distances. Instead we limit ourselves to areas that are characterized by local or regional seismicity: active plate boundaries. Another important requirement for MDD is posed by the specifications of the receiver array. Considering that the integral is along the receiver positions, it is important to use an array that contains a relatively high receiver density and sufficient aperture of receivers. The spacing should be suitable to correctly sample the dominant frequency range of the selected earthquakes. Taking these considerations into account, we decided to work with a dense array of broadband multicomponent receivers in the Hellenic zone, Peloponnesus, Greece. This array was deployed as part of the MEDUSA project: Multi-disciplinary Experiments for Dynamic Understanding of Subduction under the Aegean Sea (Suckale et al., 2009). It has an acceptable interreceiver spacing in the western part of the array, where a number of 12 receivers form a 2D line with an interreceiver spacing of about 3 - 7 km.

In the case of interferometry, the best validation is provided by an active survey over the same receiver array to verify whether the estimated response to a virtual source resembles the response to a real source. Considering the fact that we do not have access to a controlled-source survey, we instead conduct a 2D elastodynamic modelling experiment with a model based on the geological setting of the Hellenic subduction zone. Finally, we use this experiment as a playground to learn whether there is room for improvement in the area of passive data acquisition for the purpose of obtaining more accurate and reliable reflection responses by MDD. The question is whether more can be gained by increasing the density of receivers or otherwise by using a higher number of passive sources to improve illumination.

## 5.2. Geological Setting

The study area as determined by the selected array is located in the east-central Mediterranean, in southern Greece. Here the convergence of the African and Eurasian plate is accommodated by a complex geological system: the Hellenic thrust belt. Between the two islands Crete and Kephalonia the thrust belt is characterized by rapid subduction of the Ionic lithosphere beneath the Aegean lithospheric plate. Gravity data has indicated that the Ionian lithosphere is of oceanic nature (Tsokas & Hansen, 1997) and is covered by thick sedimentary layers as revealed by deep seismic reflection data (Kokinou et al., 2005). The highest convergence rates of about 40 mm/year are found in the southern part at the height of the Peloponnesus island, where the array is located. The coupling between the rapidly converging Ionian slab and overriding Aegean plate manifests in active local seismicity. The shallower part of the associated Wadati-Benioff zone dips with an angle of 30 degrees from 20 km to 100 km depth (Papazachos et al., 2000). Further northward the convergence rate diminishes significantly to values of 5-10 mm/year, where the nature of the tectonic regime converts into collisional (McKenzie, 1978). These two different convergence zones are separated by an area of transtensional deformation: the Central Hellenic Shear Zone (CHSZ), which extends from northern Peloponnesus to Kephalonia. The transtensional deformation is accommodated by a rapidly extending rift system: the Corinth rift (Suckale et al., 2009).

The Wadati-Benioff zone below Peloponnesus provides earthquakes of relatively high signal-to-noise ratio and a beneficial positioning with respect to the selected array. The wavefields from these earthquakes will likely interact with the Ionian subduction slab, the Aegean Moho and the sedimentary basin below the array. However, it is also possible that the wavefields interact with the complex CHSZ even though it is further north than the array. With a 2D line it is not possible to determine with certainty whether the wavefield interacts with structures below the array or right next to it.

## 5.3. Processing

We aim to keep the processing as simple as possible: the preprocessing flow is limited to bandpassfiltering and rotation of the horizontal component. For the interferometric part of the processing, we focus on 2D P-SV converted waves. We therefore follow the same steps as we demonstrated in Chapter 3 for the application of full-field MDD and crosscorrelation.
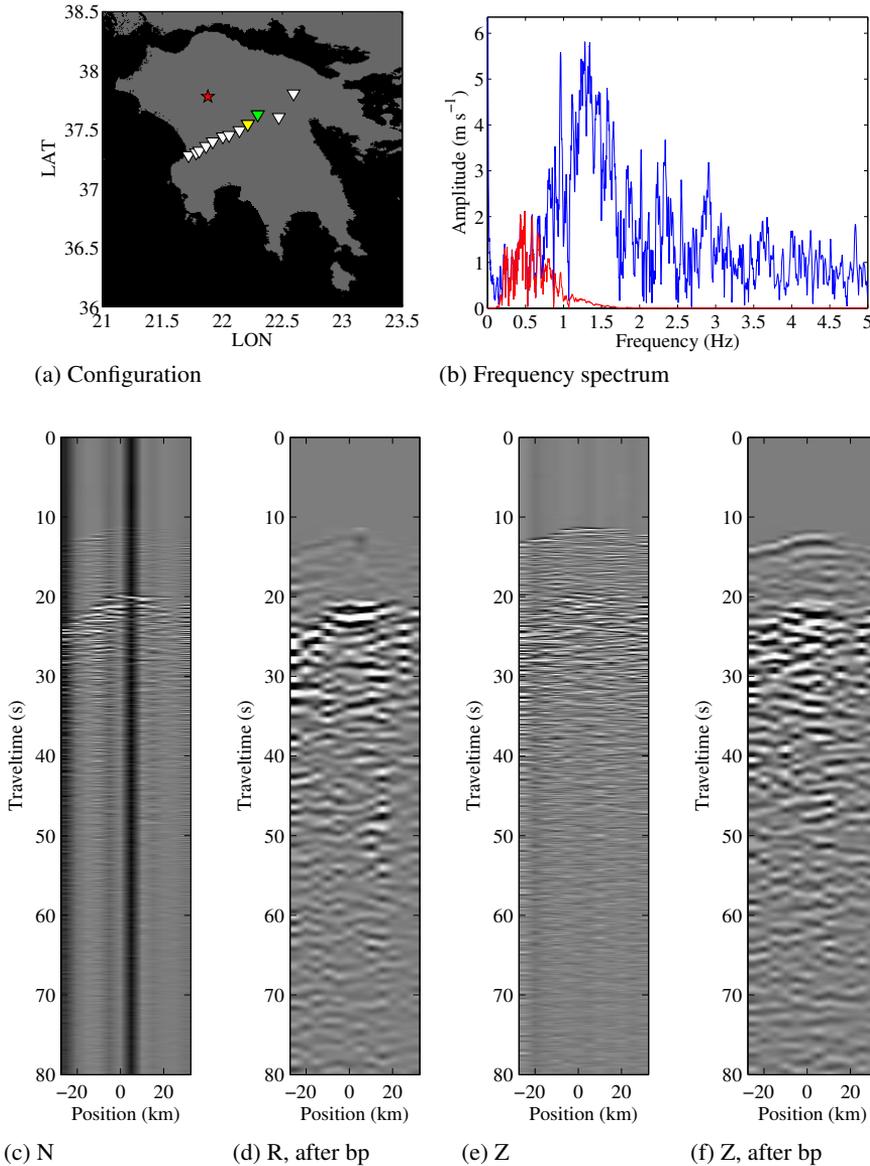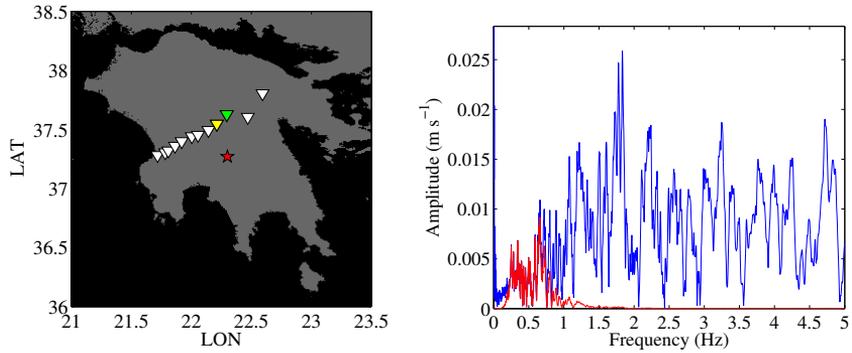
(a) Configuration

(b) Frequency spectrum

(c) N            (d) R, after bp            (e) Z            (f) Z, after bp

Figure 5.1: *Rotated earthquake recordings from the MEDUSA experiment in Peloponnesus, Greece.*
*(**a**) Receiver positions are denoted by white inverted triangles, virtual source positions S009 and S010*
*by yellow and green inverted triangles, respectively, and the epicenter of earthquake ID 2223196 by*
*the red star. (Copyright (c) 2016, Francois Beauducel, covered by BSD License). (**b**) Frequency*
*spectrum of the earthquake recording before (blue) and after application of the bandpass (bp) filter*
*(red). (**c**) North component (N). (**d**) Radial component (R) after bp filter and rotation. (**e**) Vertical*
*component (Z). (**f**) Vertical component after bp filter.*

(a) Configuration

(b) Frequency spectrum

(c) N

(d) R, after bp

(e) Z
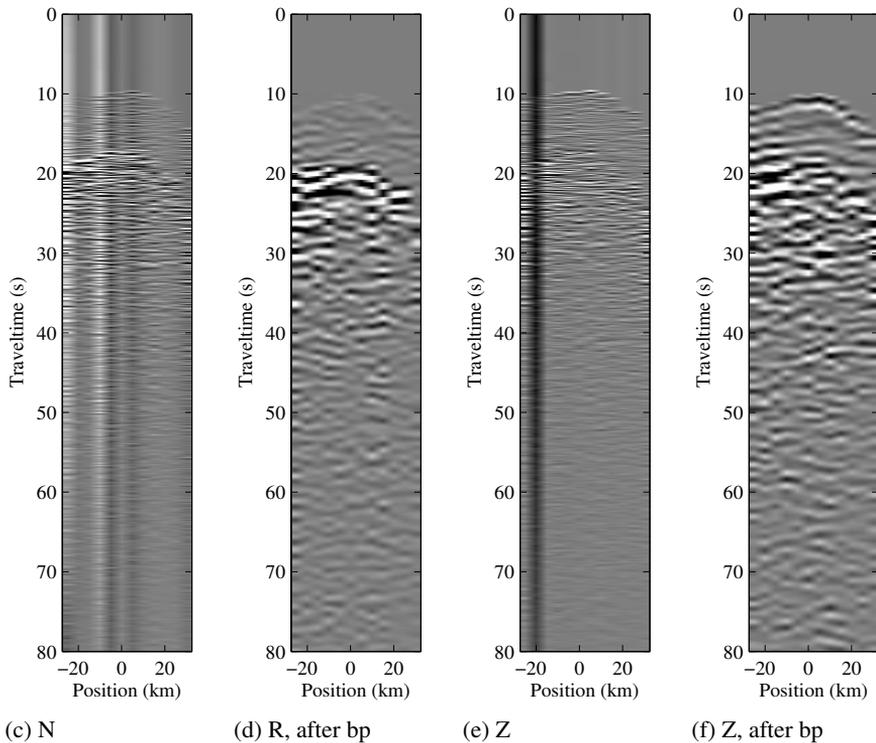
(f) Z, after bp

Figure 5.2: *As Figure 5.1, for earthquake with id 2338765.*

### 5.3.1. EARTHQUAKE RECORDINGS

We use the field data recorded by an array with multicomponent broadband sensors in southern Greece, Peloponnesus, employed as part of the MEDUSA project (Suckale et al., 2009). We limit ourselves to the denser western part of the array, which was specifically designed for imaging purposes: this part comprises of a line array of 12 receivers with an interreceiver distance that varies between 3 - 7 km. We selected two earthquake events on the basis of their high signal-to-noise ratio and large depth. Figure 5.1a shows the epicenter of earthquake with ID 2223196. The hypocenter of this 3.9 magnitude earthquake was 75 km deep. The second earthquake with ID 2338765 has a magnitude of 4.1 and is 42 km deep (Figure 5.2a). The large depth range of these earthquakes and their relative proximity to the array ensure that the array is predominantly illuminated at low wavenumbers, which are necessary to obtain stationary phases. Figures 5.1c, 5.1e, 5.2c and 5.2e show the particle-velocity components of the raw earthquake recordings, prior to bandpass filtering and rotation.

### 5.3.2. BANDPASSFILTER AND ROTATION

We rotate the horizontal components by an angle of 50 degrees such that the N-component corresponds to the x-component (radial) with respect to the array orientation. Note that in this study, we define the radial component to be parallel to the array. The 2D line is orientated approximately perpendicular to the subduction trench. From that fact we derive the crude assumption that the medium variations along the trench are negligible compared to the medium parameters along the 2D line array. This assumption permits us to apply the 2D full-field MDD equation (3.13) from Chapter 3, whereby the radial component serves as the x-component and the vertical naturally as the z-component.

In Figures 5.1b and 5.2b the spectra of the two respective earthquakes are shown in blue. We applied a Butterworth bandpassfilter with a low-cut at 0.2 Hz in order to minimize the pollution of low frequency noise. The origin of the low frequency noise could be due to wave interaction of the sea. With a maximum receiver spacing of 7 km and an average S-wave velocity of the crust of 3.7 km s$^{-1}$ (Suckale et al., 2009), we calculate the spatial Nyquist frequency at approximately 0.3 Hz. Since the positioning of the hypocenters are relatively deep below the array, the wavefields will be dominated by low wavenumbers. Therefore, we allow frequencies above the aliasing treshold by placing the high-cut of the bandpass filter at 0.7 Hz. The red curve in Figures 5.1b and 5.2b shows the spectra of the two respective earthquake recordings after filtering. Note that after we obtain the virtual response estimates by interferometry we apply the same bandpass filter again, to

remove artefacts that could possibly be introduced by interferometric processing. This is primarily necessary for the MDD method, because the time-windowing and inversion could introduce low frequency artefacts as we explain later.

### 5.3.3. Direct arrival picking

In order to estimate the earthquake recordings without free-surface interaction, we need to select the direct incident wavefields. As we demonstrated in Chapter 3, it would suffice to only select the P-wave, which is possible to accomplish with straightforward automatic procedures such as first break picking. Here, we manually select the direct S-wave in addition to the direct P-wave. The manual selection is not a problem when the dataset comprises of only a limited number of earthquakes and receivers. Next, the travel time picks of the direct P- and S-wave are used to construct a time window that extracts the direct P- and S-waves for estimating the earthquake recordings without free surface interaction, $V^o$. Theoretically, we would also need to extract the internal multiples from the recordings to complete the estimated field, but this is not possible to conduct. By neglecting the internal multiples, we make the inherent assumption that the free-surface multiples in the data set can only be initiated by directly incident fields. This will inevitably cause errors in our reflection response estimation. The good news is that this error does not affect the PSF that is inverted, as is the case in ballistic MDD methods (Nakata et al., 2014, Nishitsuji et al., 2016). A taper is applied to the time window in order to prevent higher frequency artefacts to be introduced by the Fourier transformation in the next step. We adjust the smoothness of the time window such that the low frequency artefacts it introduces do not overlap with the dominant frequency-content of the signal. That way, the artefacts can easily be diminished by applying a low-cut filter after MDD.

## 5.4. Results

We estimate virtual responses by applying SI by crosscorrelation and full-field MDD to the two earthquake recordings using the elastodynamic equations 3.1 and 3.13, respectively, from Chapter 3. Only the horizontal particle velocity response to a horizontally oriented virtual source is shown, because this response relies primarily on S-waves which are most dominant in the recording. After obtaining the virtual responses by interferometry, we apply a normal moveout correction (NMO) to each virtual shot using the crustal P- and S-wave velocities used by Suckale et al. (2009) for their background model. The subsequent stack of the NMO-corrected shots helps to minimize artefacts and enhance the desired virtual reflections by destructive and constructive interference, respectively.
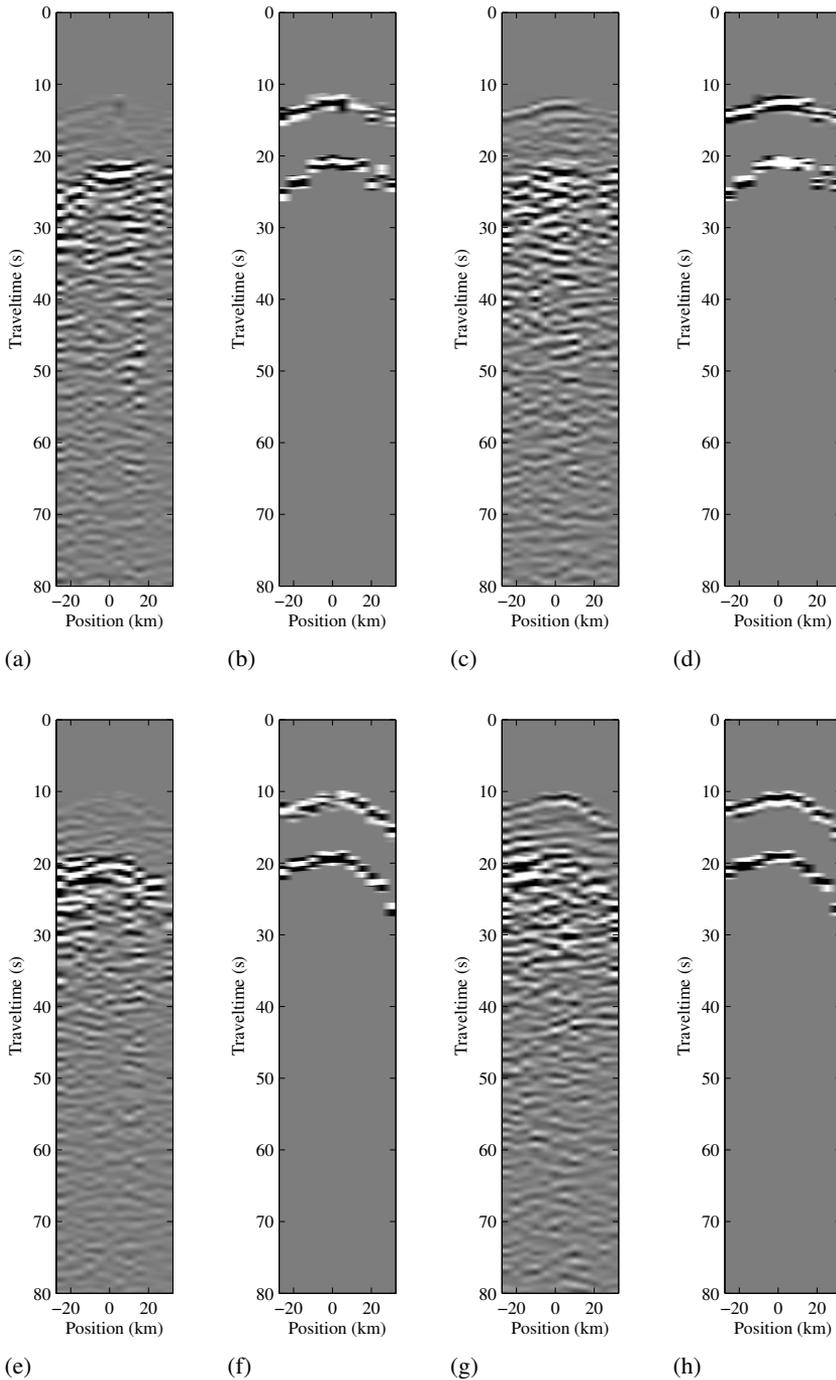
Figure 5.3: *The direct P- and S-wave are selected to estimate the $V^o$ field of the two earthquake recordings. (**a**) Recording of radial component of earthquake with ID 2223196. (**b**) Direct P- and S-wave selected from (a). (**c**) Recording of vertical component of earthquake with ID 2223196. (**d**) Direct P- and S-wave selected from (c). (**e**)-(**h**) are the same as (**b**)-(**d**) but for earthquake earthquake with ID 85.*
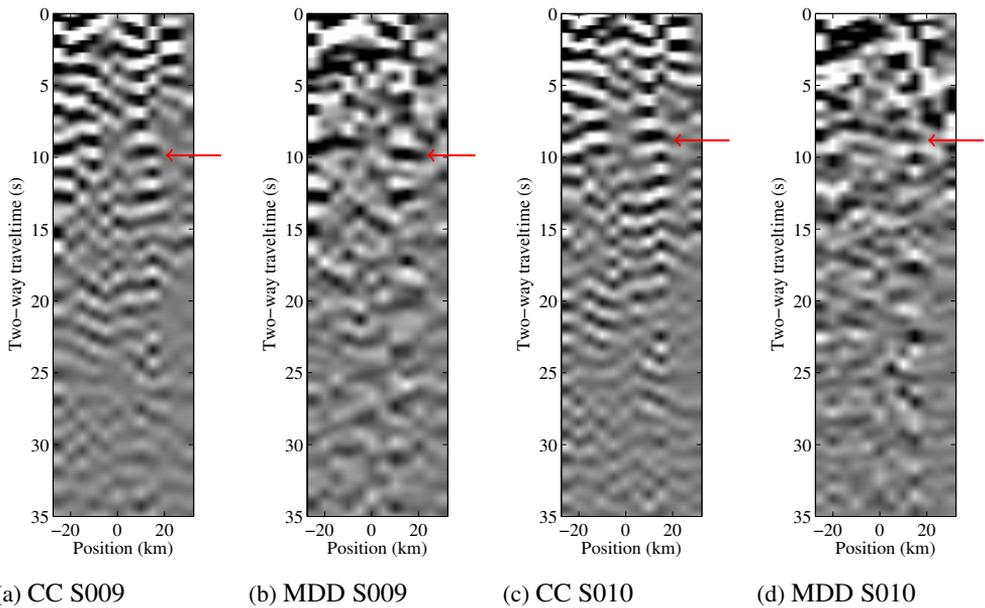
(a) CC S009          (b) MDD S009          (c) CC S010          (d) MDD S010

Figure 5.4: *Horizontal-component reflection responses to horizontally-oriented virtual sources obtained by applying crosscorrelation (CC) and full-field MDD to the field data shown in Figures 5.1 and 5.2. (a) Crosscorrelation result $R_{1|1}$ at virtual source S009 (yellow receiver in Figure 5.2a). (b) Full-field MDD result $R^o_{1|13}$ at virtual source S009. (c) Crosscorrelation result $R_{1|1}$ at virtual source S010 (green receiver in Figure 5.2a). (d) Full-field MDD result $R^o_{1|13}$ at virtual source S010.*

### 5.4.1. VIRTUAL REFLECTION RESPONSES

The estimation of the reflection response by crosscorrelation for a virtual source at receiver position S009 (yellow inverted triangle in Figures 5.1a and 5.2a) is shown in Figure 5.4a. The ringy character of the response makes it difficult to distinguish any features that resemble reflections in this result. However, at around 9 to 10 s two-way traveltime (TWT) two regions of a more distinct feature can be observed (indicated by a red arrow). When we apply full-field MDD and analyze the response to the same virtual source, at position S009, the ringy appearence disappears: in Figure 5.4b we can distinguish the feature at 9 to 10 s TWT. This feature may be part of a reflection, because it is more distinct than the other noisy features we observe in Figure 5.4b. We additionally look at the responses to the virtual source just east of receiver position S009: at receiver position S010 (green inverted triangle in Figures 5.1a and 5.2a). The virtual response we estimate with full-field MDD in Figure 5.4d again shows a feature at 9 to 10 s TWT. It is also visible in the crosscorrelation result, but more difficult to discern (Figure 5.4c).

### 5.4.2. NMO-CORRECTED STACKS

By stacking the NMO-corrected virtual shots, we aim to eliminate artefacts and enhance the possible reflections. For the case of crosscorrelation, this procedure does not reveal more coherent features (Figure 5.5a). In contrast, the NMO-corrected stacked section of the virtual responses obtained by full-field MDD does reveal more visible coherent features (Figure 5.5b). At around 9 to 10 s TWT a horizontal feature is visible that seems to continue after a downward jump at about 14 s TWT as indicated by the red dashed lines in Figure 5.5c. These TWT values could be indicative of the Moho reflection, which does show discontinuous behaviour in this area (Suckale et al., 2009). There are strong features visible at 4 to 5 s TWT that seem to dip slightly towards larger TWT values of 7 s. These features, indicated with green in Figure 5.5c, could represent reflections of the crystalline basement in the area. At larger TWT, we observe features that could correspond to the subduction slab (indicated with blue in Figure 5.5c).

### 5.4.3. SCATTERING ANALYSIS

In Chapter 4 we analyzed the relationship between the diffusion of seismic intensity in time and the scattering potential of three different 2D models. We showed that it is possible to estimate the diffusivity, $D$, of the medium with the diffusion equation (4.2) from Paasschens (1997), which we repeat here:
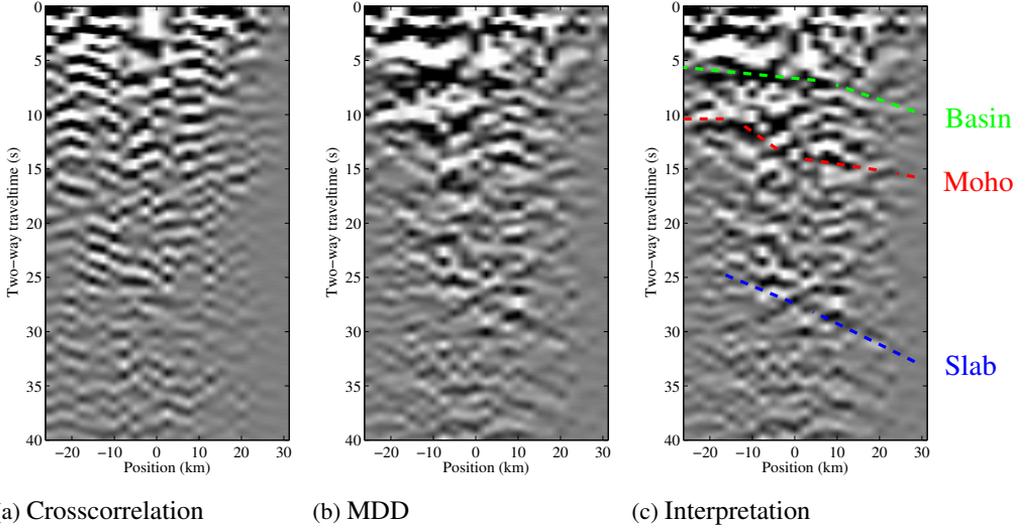
(a) Crosscorrelation    (b) MDD    (c) Interpretation

Figure 5.5: *NMO-corrected stacked sections of the virtual response estimates obtained from the field data shown in Figures 5.1 and 5.2. (**a**) NMO-corrected and subsequent stack of all virtual shot gathers $R_{1|1}$ obtained by crosscorrelation. (**b**) NMO-corrected and subsequent stack of all virtual shot gathers $R_{1|13}^o$ obtained by full-field MDD. (**c**) Interpretation of the observed dominant features in Figure 5.5b.*

$$P(r, t) = \frac{1}{(4\pi D t)^{d/2}} \exp\left(-\frac{r^2}{4Dt} - \frac{ct}{l_a}\right), \tag{5.1}$$

where $c$ signifies the average propagation velocity, $d$ the spatial dimensionality and $l_a$ the mean free path of intrinsic absorption of the medium. The distance between source and receiver is denoted by $r$. The diffusivity, $D$, is directly related to a parameter that is proportional to the average distance between scatterers, $l$, the scattering mean free path:

$$D = \frac{cl}{d} \tag{5.2}$$

For the 2D case we investigated in Chapter 4, we showed that the diffusion equation (5.1) becomes:

$$P(r, t)^{2D} = \frac{1}{(2\pi clt)} \exp\left(-\frac{r^2}{2clt} - \frac{ct}{l_a}\right) \tag{5.3}$$

(a) ID 2223196, 0.03-0.2 Hz  (b) ID 2223196, 0.2-0.7 Hz  (c) ID 2223196, 0.7-2 Hz

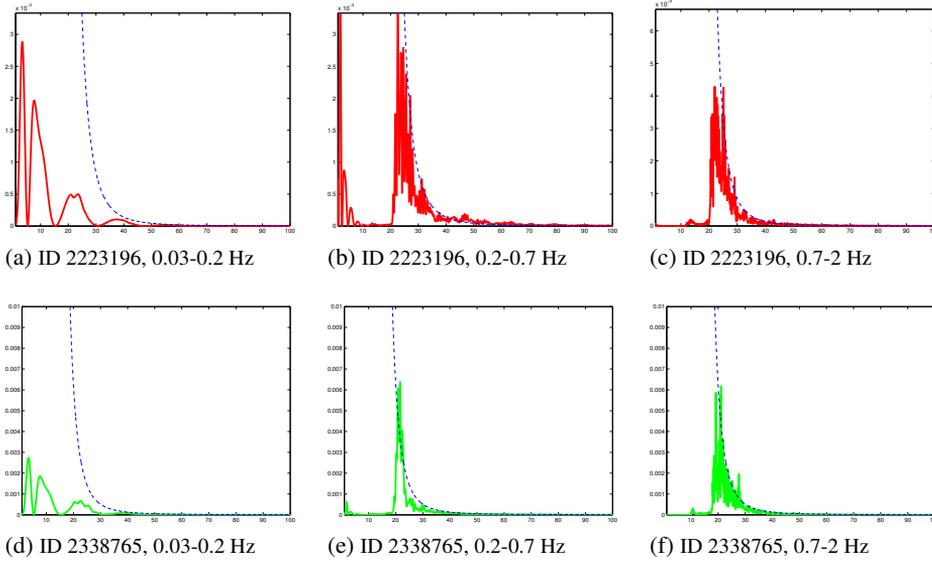(d) ID 2338765, 0.03-0.2 Hz  (e) ID 2338765, 0.2-0.7 Hz  (f) ID 2338765, 0.7-2 Hz

Figure 5.6: *Frequency-dependent scattering analysis. (**a**) 3D diffusion curve fit with equation (5.4) to the average intensity of the earthquake recording with ID 2223196 for frequency band 0.03 - 0.2 Hz. (**b**) Same as a for frequency band 0.2 - 0.7 Hz. (**c**) Same as a for frequency band 0.7 - 2 Hz. (**d**)-(**e**) same as (**a**)-(**c**), but for the earthquake recording with ID 2338765.*

We observed that as we increased the number of scatterers, the diffusivity, $D$, and therefore also the scattering mean free path, $l$, decreased accordingly (Figures 4.1c, 4.2c and 4.3c). Here, we aim to perform a similar analysis of the diffusion in time of the measured intensity of the two earthquake recordings. We substitute equation (5.2) into equation (5.1), but, different from Chapter 4, here we apply spatial dimension $d = 3$, because we expect the multiple scattering in the region to have a 3D character:

$$P(r, t)^{3D} = \frac{1}{(\frac{4}{3}\pi c l t)^{3/2}} \exp\left(-\frac{r^2}{\frac{4}{3}clt} - \frac{ct}{l_a}\right) \tag{5.4}$$

The intensity averaged over all receivers of the earthquake recording with ID 2221396 in the frequency range 0.2 - 0.7 Hz is displayed in Figure 5.6b. When we neglect intrinsic attenuation ($l_a \to \infty$), fitting equation (5.4) to the curve in Figure 5.6b yields a mean free path value of 0.2 km. Figure 5.6c shows the same as Figure 5.6b, but for the higher frequency range of 0.7 - 2 Hz. This analysis yields the same diffusivity and therefore mean free path value of 0.2 km. Figures 5.6e and 5.6f display the intensity averaged over all receivers of the recording of the earthquake with ID

2221396 for the 0.2 - 0.7 Hz frequency band and the 0.7 - 2 Hz band, respectively. For this earthquake we estimate a mean free path value of 0.1 km when we fit equation (5.4) to the intensity curve in Figure 5.6e. Note that for a lower frequency range of 0.03 - 0.2 Hz (Figures 5.6a and 5.6d), the scattering coda does not manifest itself and therefore it is not possible to fit equation (5.4). This shows that the scattering coda is generated by lithospheric heterogeneities that are sensed by wavefields with dominant frequencies above 0.2 Hz.

## 5.5. SYNTHETIC DATA

We conduct an elastodynamic modelling experiment in 2D to investigate whether it is theoretically possible to obtain reflections by crosscorrelation or full-field MDD with this data set. To construct the background velocity model and its more detailed structural features as shown in Figure 5.7a, we use the background velocities and final lithospheric imaging results from Suckale et al. (2009) and are further inspired by the PREM model (Dziewonski & Anderson, 1981). The lithospheric crust has P- and S-wave velocities of 6.5 and 3.7 km s$^{-1}$, respectively, and the Moho depth varies between 23 and 40 km. The upper and lower part of the mantle have P- and S-wave velocities of 8.3 and 4.7 km s$^{-1}$, and, 9.2 and 5.1 km s$^{-1}$, respectively. The subducting oceanic slab dips with an angle of about 21 degrees and has P- and S-wave velocities of 7.4 and 4.2 km s$^{-1}$, respectively, and a density of 2800 kg m$^{-3}$. The densities of the upper and lower mantle are 3200 and 3500 kg m$^{-3}$, respectively. A sedimentary basin is implemented in the model by creating a low density anomaly (2000 kg m$^{-3}$) between 0 and 8 km depth (see Figure 5.7b). The subducting slab is likely to be covered with a thick sedimentary layer, which results in a strong impedance contrast with the surrounding mantle material. Although results in Figure 5.6 indicate there is significant scattering in the area, we expect the 2D effects of scattering on SI methods to be different from those in 3D. Therefore, we do not introduce extra scattering in the 2D model.

The Wadati-Benioff zone is is responsible for the majority of the earthquakes occurring in the Hellenic subduction zone. We model this zone by implementing 50 double-couples which are located approximately in the area along the subducting slab (see Figure 5.7a). The orientation of the source mechanisms varies randomly and the peak frequency of the source functions varies between 0.3 and 1.1 Hz. As we move more to the right in the model the source locations become deeper. This resembles the actual hypocenter distribution in the area.

We place 81 receivers with a 1 km spacing at a distance of 30 km from the left side of the model to a distance of 110 km. This dense regular spacing allows us to select the direct P- and S-waves by constructing hyperbolic curves that resemble
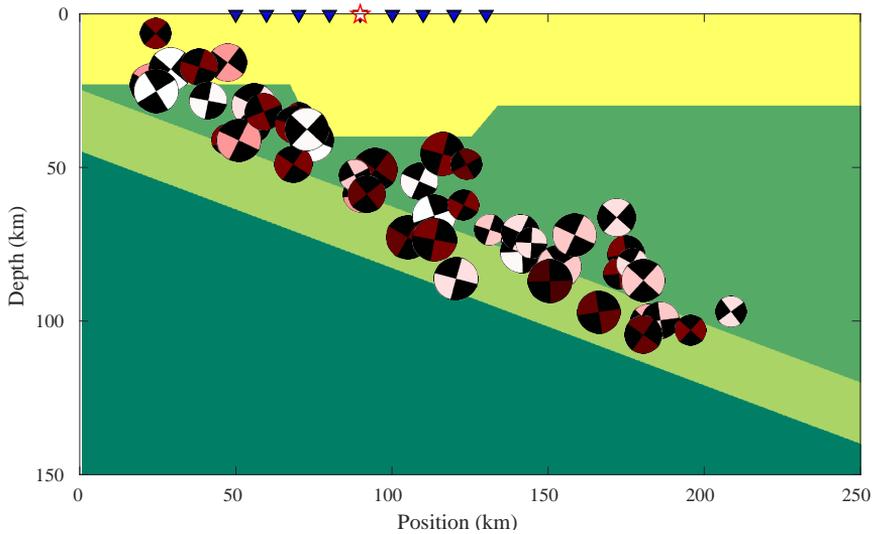
(a)
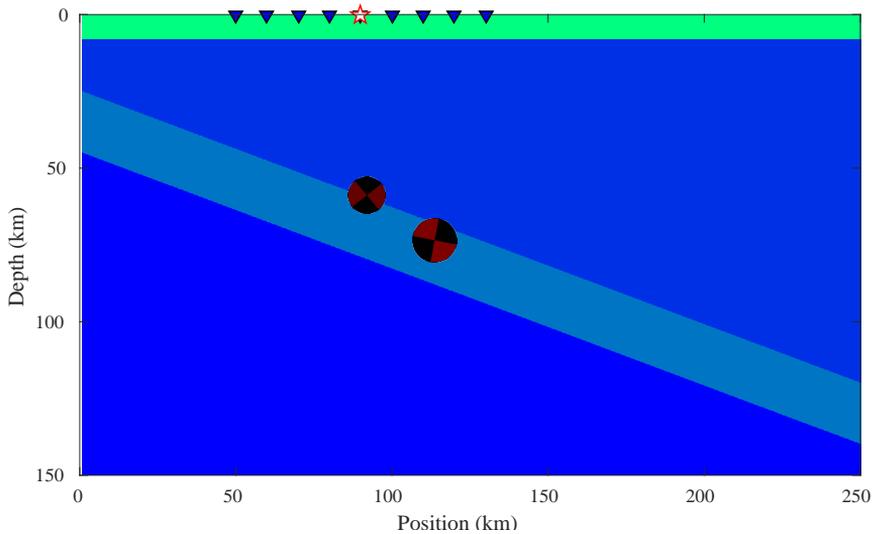


(b)

Figure 5.7: *Synthetic velocity model.* (**a**) *P-wave velocity model for the case of full illumination. The earthquakes are modelled with double-couple radiation patterns of different orientations and peak frequencies varying between 0.3 Hz (dark red) and 1.1 Hz (white). We show only a portion of the receiver array, denoted by the blue triangles. The virtual source position is denoted by the red star.* (**b**) *Same as (a) but for the density and for the case of limited illumination. This model shows we implemented a sedimentary basin by using a lower density.*
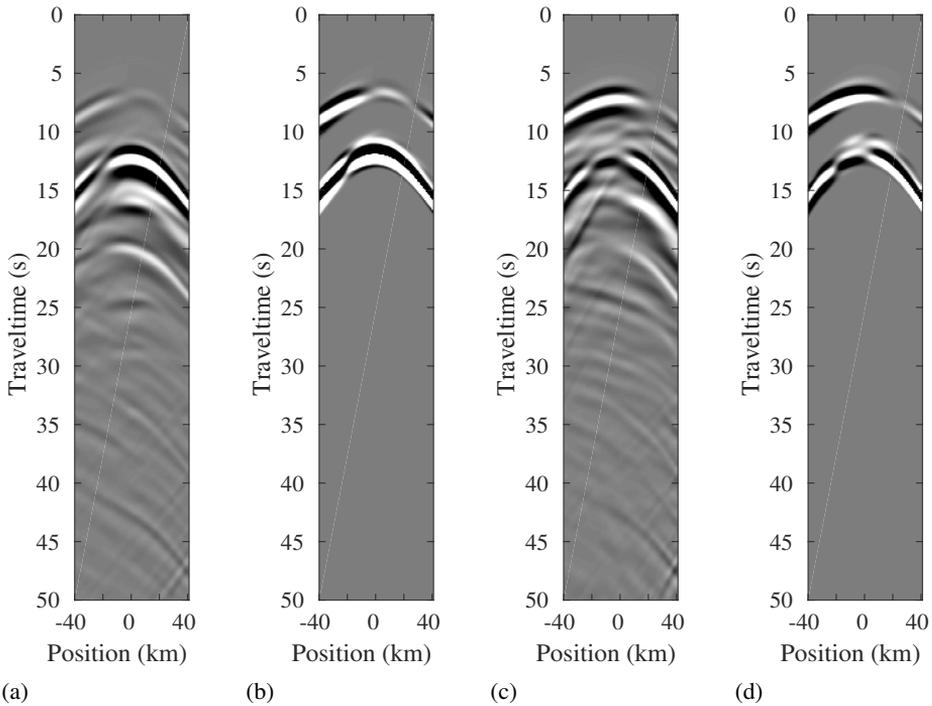
Figure 5.8: *We select the direct P- and S-wave to estimate the $V^o$ field of the synthetic earthquakes by applying a hyperbolically shaped time-window. Here we show an example of this procedure for one synthetic earthquake. (**a**) Recording of horizontal component. (**b**) Direct P- and S-wave selected from (a). (**c**) Recording of vertical component. (**d**) Direct P- and S-wave selected from (c).*

the respective direct arrivals. For this procedure we only need to select the apex and a second data point of the direct arrival, instead of picking trace by trace. Although the direct wave arrivals are only approximated by this type of curve, it serves as a suitable tool to make the selection procedure more efficient. See Figure 5.8 for an example of this procedure for one of the synthetic earthquakes.

During the experiments, we observed that in some cases the full-field MDD results can be affected by low frequency artefacts. This is the result of the taper we applied to the time-window, since this smooth taper is composed of low frequencies. We remove this low frequency effect by applying a low-cut filter after inversion.

We show interferometric results for four different scenarios. The first represents the ideal scenario: all 50 earthquake recordings sampled by all the 81 receivers are used as input. The second shows the effect of sampling the 50 recordings with only 12 receivers with an interreceiver spacing of 7 km. This shows us what we

could theoretically obtain in case of having the receiver configuration given to us by the MEDUSA experiment, but with maximum earthquake illumination. The third and fourth scenarios deal with limited illumination by just two earthquakes for the case of 81 receivers and just the 12 receivers with an interreceiver spacing of 7 km, respectively. This fourth scenario represents the closest resemblance to our field data set and will help us to determine whether the continuous features we see in Figure 5.4 are likely to be reflections or artefacts. All the other configurations serve to show us what we could gain by either increasing the density of receivers to improve wavefield sampling conditions, or otherwise by using more passive sources to improve illumination.

### 5.5.1. FULL ILLUMINATION

When we compare crosscorrelation results to the full-field MDD results, we observe that artefacts are more pronounced in Figure 5.10a than in Figure 5.9a. However, looking at only one virtual source does not suffice to draw final conclusions. NMO-corrected stack sections incorporate all virtual responses and serve to estimate the imaging potential of the methods. Both the crosscorrelation (Figure 5.10c) and MDD result (Figure 5.9c) retrieve the important structural features, being the sedimentary basin, Moho and subduction slab. However, in Figure 5.10c there are two dominant artefacts visible. One is located just above the real Moho reflection stack and the second is located in between the top and bottom slab reflections. This type of artefacts could lead to misinterpretation of the geological structure.

When we decrease the receiver sampling in this case of full passive source illumination, the biggest problem that arises is that of spatial sampling aliasing. Both methods are affected by this (see Figures 5.10b and 5.9b). Figures 5.10d and 5.9d show that the NMO-correction and stacking does not improve the problem of aliasing. Moreover, these figures also show that having lower receiver sampling decreases the quality significantly when compared to Figures 5.10c and 5.9c.

### 5.5.2. LIMITED ILLUMINATION

We simulate the situation of limited illumination by using only two synthetic earthquake recordings that are relatively close to each other. However, we do ensure that the two earthquakes are in stationary phase with respect to the array. This corresponds to the situation we have with the field data set, where we also have two earthquakes that are within the Fresnel zone up to a certain frequency.

When we have full coverage by the 81 receivers, the virtual reflection response obtained by MDD in Figure 5.11a resembles the result in case of full illumination
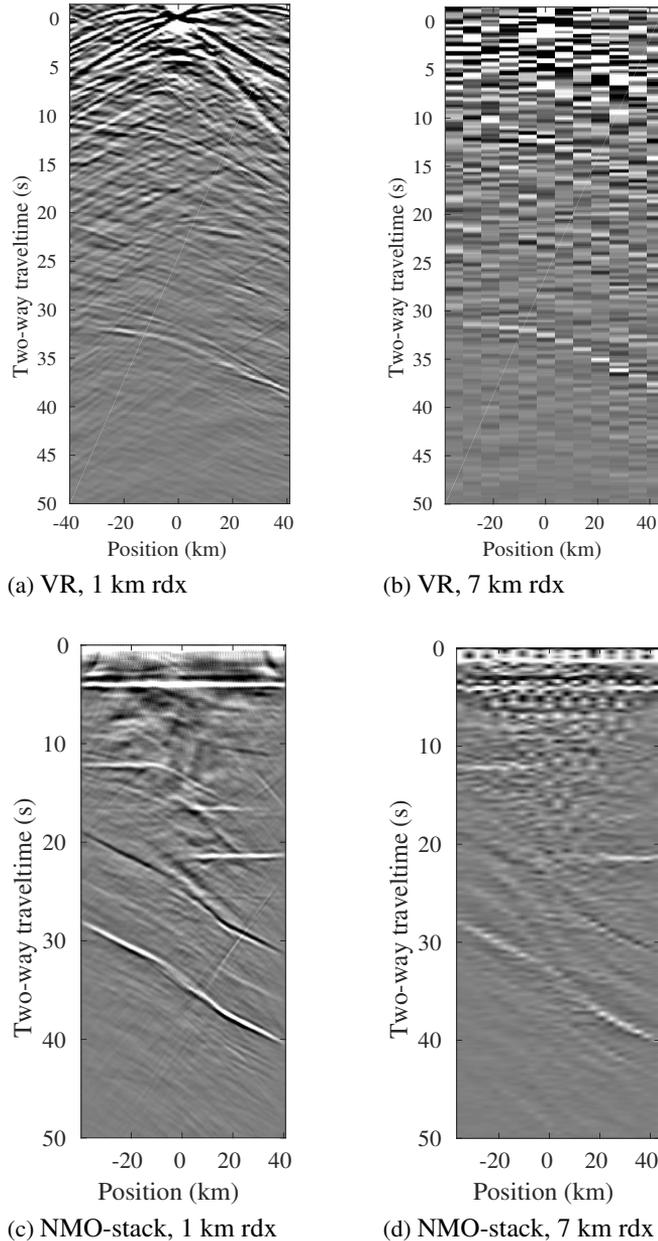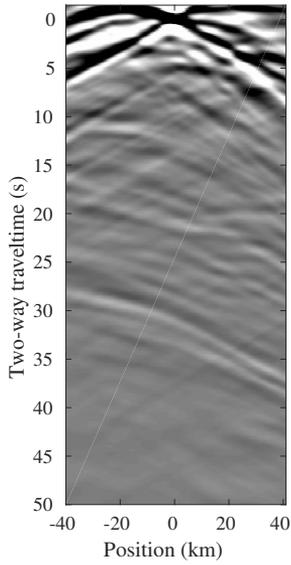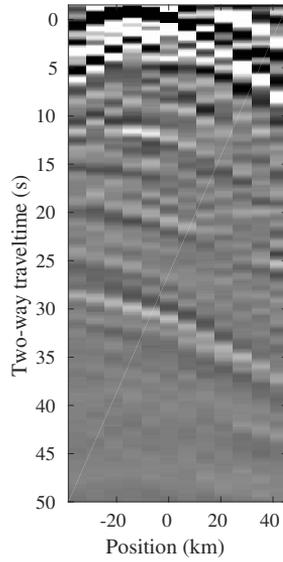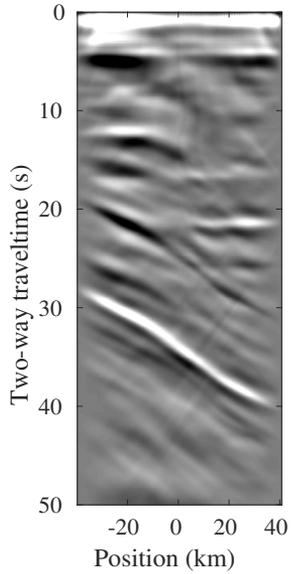
5



(a) VR, 1 km rdx

(b) VR, 7 km rdx



(c) NMO-stack, 1 km rdx

(d) NMO-stack, 7 km rdx

Figure 5.9: *Full-field MDD applied to synthetic elastodynamic data of all 50 earthquake recordings of the Wadati-Benioff zone. (a) $R^o_{1|13}$ virtual reflection response (VR) obtained from the data sampled at an interreceiver spacing (rdx) of 1 km. (b) $R^o_{1|13}$ virtual reflection response obtained obtained from the data at rdx of 7 km. (c) NMO-corrected stack of virtual responses obtained from data sampled at rdx of 1 km. (d) NMO-corrected stack of virtual responses obtained from data sampled at rdx of 7 km.*
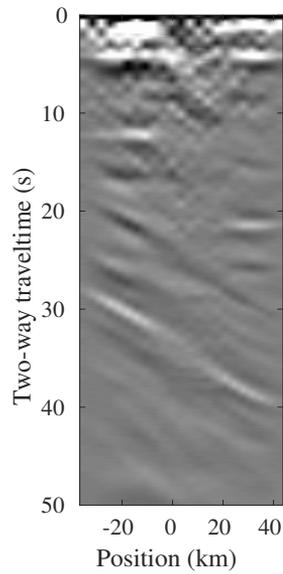
(a) VR, 1 km rdx

(b) VR, 7 km rdx

(c) NMO-stack, 1 km rdx

(d) NMO-stack, 7 km rdx

Figure 5.10: *Same as Figure 5.9, but for crosscorrelation.*

(a) VR, 1 km rdx

(b) VR, 7 km rdx

(c) NMO-stack, 1 km rdx
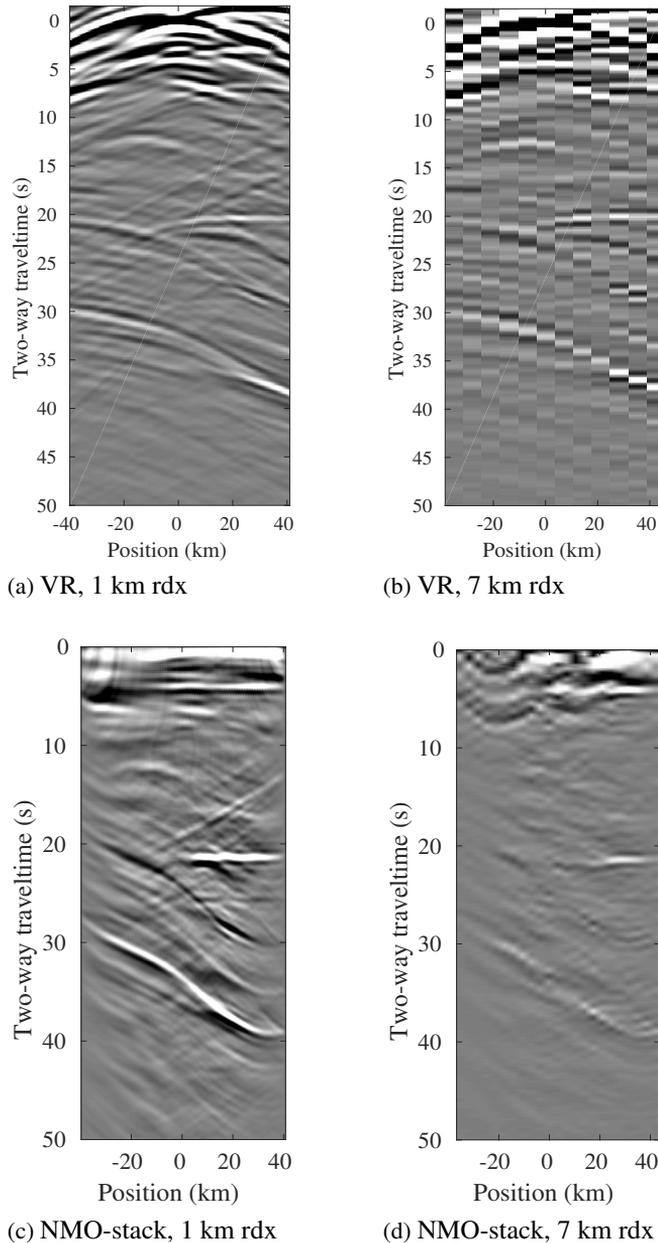
(d) NMO-stack, 7 km rdx

Figure 5.11: *Full-field MDD applied to synthetic elastodynamic data of just two hypocenters from the Wadati-Benioff zone as shown in Figure 5.7b. (a) $R^o_{1|13}$ virtual reflection response (VR) obtained from the data sampled at an interreceiver spacing (rdx) of 1 km. (b) $R^o_{1|13}$ virtual reflection response obtained obtained from the data at rdx of 7 km. (c) NMO-corrected stack of virtual responses obtained from data sampled at rdx of 1 km.(d) NMO-corrected stack of virtual responses obtained from data sampled at rdx of 7 km.*
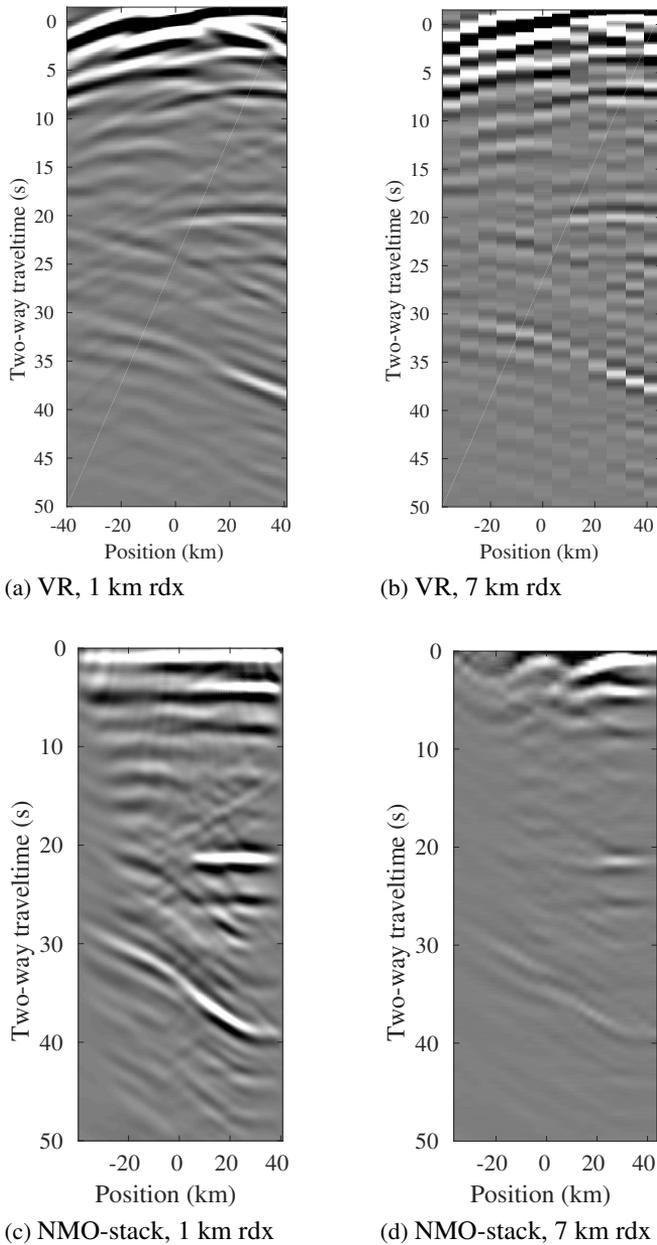
(a) VR, 1 km rdx

(b) VR, 7 km rdx

(c) NMO-stack, 1 km rdx

(d) NMO-stack, 7 km rdx

Figure 5.12: *Same as Figure 5.11, but for crosscorrelation.*

in Figure 5.9a. Especially the NMO-corrected stack results shown in Figure 5.11c are of surprising good quality: the sedimentary basin bottom, the discontinuity of the Moho and almost the full subduction slab are visible. The main difference with the results in Figure 5.9c are that more artefacts are visible. The crosscorrelation results under these limited illumination conditions in Figure 5.12a show that it is more difficult to distinguish reflections from artefacts. For instance, the subduction slab reflections and the reflection of the shallow part of the Moho appear less clear. For example, in the NMO stack result in Figure 5.12c the artefact at 25 s TWT just below the deepest Moho reflector is relatively dominant. The same holds for the artefact at 17 s just below the sedimentary basin reflector

When we have only 12 receivers available to capture the limited stationary phases, the results diminish in quality. Nevertheless, the virtual source response obtained with full-field MDD does still allow for an interpretation of the subduction slab reflections (Figure 5.11b). In the NMO stack result in Figure 5.11d we can distinguish remnants of the reflections of the sedimentary basin, the Moho and subduction slab. The NMO stack reveals that the reflections of the sedimentary basin are particularly obscured by artefacts. Compared to the results obtained with crosscorrelation in Figures 5.12b and 5.12d, the full-field MDD result show reflections that are easier to distinguish from artefacts and also display a better resolution.

### 5.5.3. PRESTACK DEPTH MIGRATION

Finally, we apply prestack depth migration (PSDM) to the $R_{1|13}^{o}$ and $R_{3|33}^{o}$ virtual reflection cubes we obtained using full-field MDD and the $R_{1|1}$ and $R_{3|3}$ virtual reflection cubes we obtained by crosscorrelation. For this experiment, we again consider the limited illumination case displayed in Figure 5.7b. However, this time we increase the number of receivers to 300 in order to cover the entire width of the model.

The P-wave velocity model is used for the PSDM of the $R_{3|33}^{o}$ and $R_{3|3}$ results obtained by full-field MDD and crosscorrelation, respectively, because this type of response is typically dominated by P-wave energy. Figures 5.13a and 5.13b show the results of applying PSDM to those virtual responses. In spite of the limited illumination, the depth image obtained with MDD in Figure 5.13a clearly maps the larger parts of the Moho and subduction slab in the correct place. However, because of the rightward dipping orientation of the subduction slab, the receivers on the right side record very few stationary events. This explains why the right side of the model is not imaged as well as the left side. The PSDM image in Figure 5.13b obtained using the $R_{3|3}$ crosscorrelation virtual reflection cube, shows part of the slab bottom. However, the top of the slab and the Moho depression are obscured by

artefacts.

For the PSDM of the $R_{1|13}^o$ virtual reflection cube we use the S-wave velocity model, because this type of response is dominated by S-wave energy. The full-field MDD result in Figure 5.14a shows that the sedimentary basin, Moho discontinuity and the subduction slab are clearly imaged. Note that the shorter wavelength of S-waves results in a considerably higher resolution than is observed in Figure 5.13a, which is dominated by P-waves. Although both images display artefacts, we note that the artefacts are very different when comparing Figures 5.13a and 5.14a. The PSDM result of the $R_{1|1}$ virtual reflection cube obtained by crosscorrelation (Figure 5.14b) shows a similar image as its MDD equivalent (Figure 5.14a), but with a lower resolution. Moreover, where we see the Moho imaged at the correct depth between positions 180 and 250 km in Figure 5.14a, this feature is not imaged in the case of the crosscorrelation PSDM result (Figure 5.14b). This may be because MDD makes a better use of the additional illumination provided by higher order free-surface multiples.

## 5.6. DISCUSSION

Some continuous features were observed in the virtual reflection responses we estimated with full-field MDD from the field data (Figures 5.4b and Figures 5.4d). The crosscorrelation results of the same virtual source positions also indicated these features, but they were slighly harder to discern (Figures 5.4a and Figures 5.4c). The application of a NMO correction and subsequent stack did not help to improve the visibility of these continuous features in the case of crosscorrelation (Figure 5.5a). On the other hand, the NMO-stack results for full-field MDD in Figure 5.5b did reveal three distinct continuous features that could correspond to realistic timings of the primaries of the basin, Moho and the subduction slab. For example, Suckale et al. (2009) showed the Moho is shallow in the western part of the area and becomes deeper towards the East, as we show in the model we constructed on the basis of their findings (Figure 5.7a). Figure 5.5c indicates a Moho depth with a similar trend.

In Chapter 4 we learned that full-field MDD is well suited to obtain primary reflections from scattering-induced passive illumination only. Although crosscorrelation is also able to obtain primaries in this way, the anisotropy of the scattering field does significantly affect the virtual source radiation. Besides the general rule that tectonically active regions are characterized by a strong scattering (Sato et al., 2012), several observations in the field recordings also confirm this.

First of all, the earthquake recordings in Figures 5.1 and 5.2 show that scattered
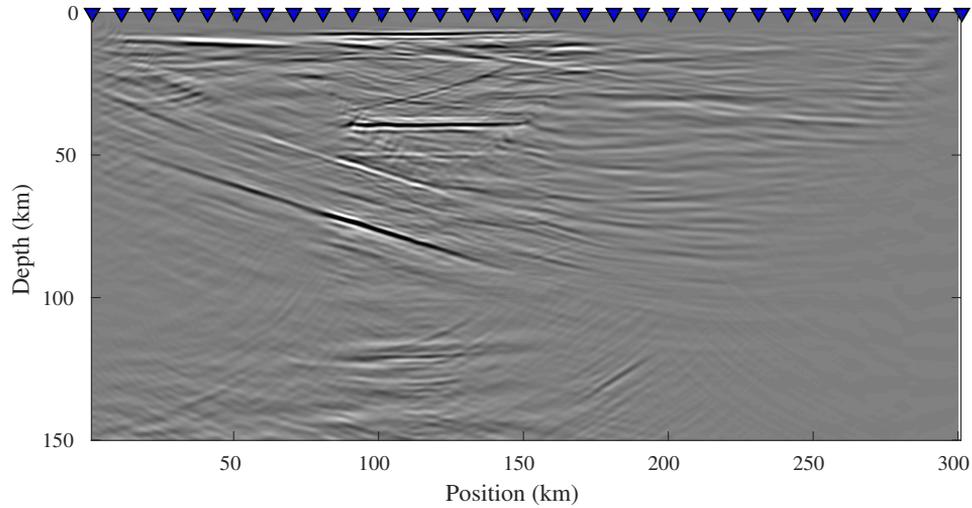
5
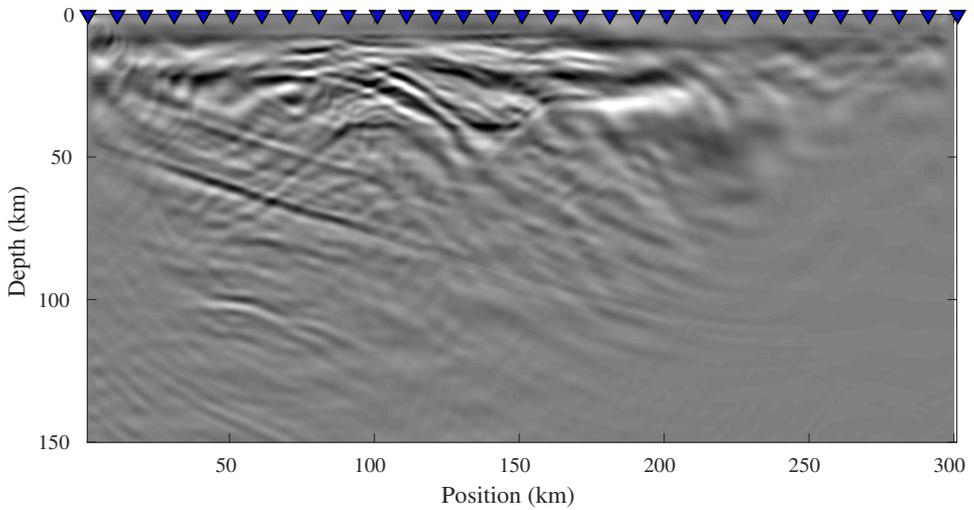


(a) Full-field MDD, P-wave velocity model
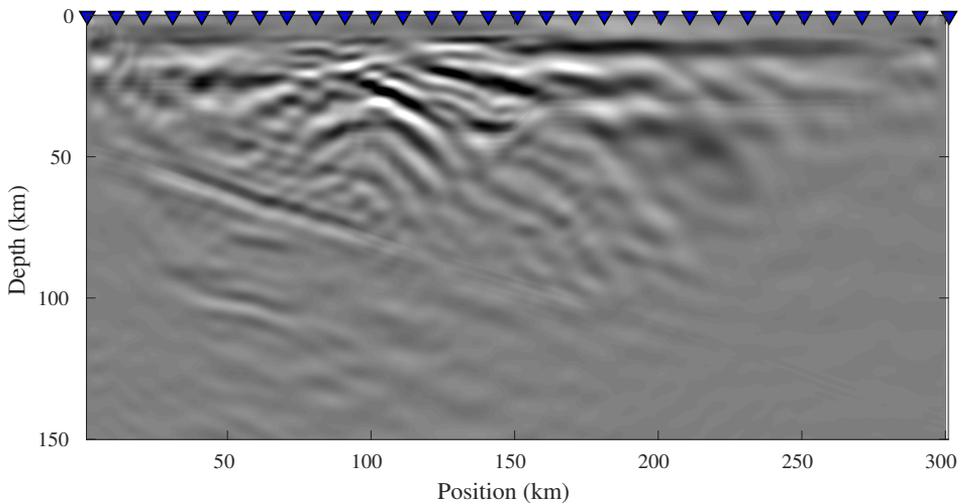


(b) Crosscorrelation, P-wave velocity model

Figure 5.13: *PSDM results of the P-wave dominated virtual reflection cubes for the case of limited illumination (see Figure 5.7b) and complete receiver coverage. (**a**) PSDM result using the P-wave velocity model for the $R^o_{3|33}$ virtual reflection cube obtained with full-field MDD. (**b**) PSDM result using the P-wave velocity model for the $R_{3|3}$ virtual reflection cube obtained with crosscorrelation.*
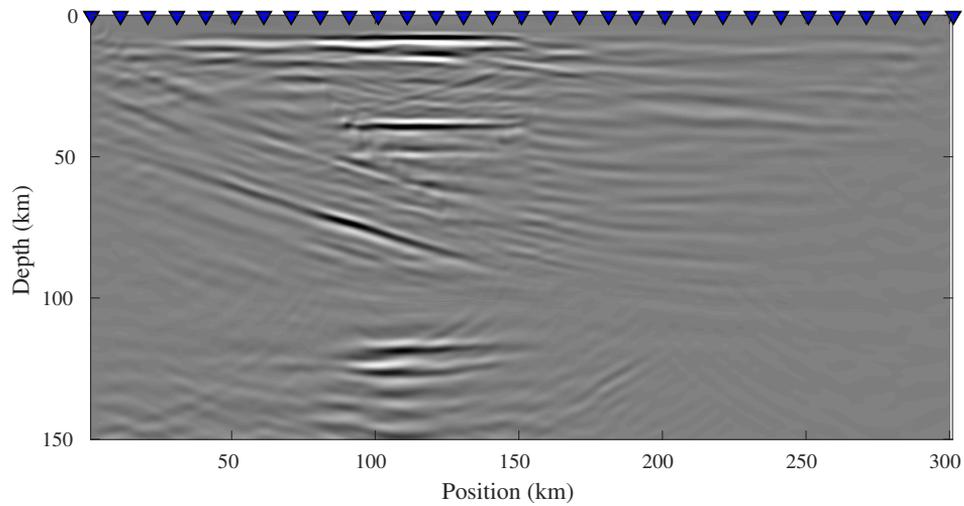
(a) Full-field MDD, S-wave velocity model



(b) Crosscorrelation, S-wave velocity model

Figure 5.14: *PSDM results of the S-wave dominated virtual reflection cubes for the case of limited illumination (see Figure 5.7b) and complete receiver coverage. (**a**) PSDM result using the S-wave velocity model for the $R^o_{1|13}$ virtual reflection cube obtained with full-field MDD. (**b**) PSDM result using the P-wave velocity model for the $R_{1|1}$ virtual reflection cube obtained with crosscorrelation.*

events continue to be clearly visible for long recording times. Moreover, the frequency-dependent scattering analysis showed that the curvatures did not change when a higher frequency range of 0.7 - 2 Hz was selected with the bandpass filter and that scattering coda did not develop in the lower frequency range of 0.03 - 0.2 Hz (see Figure 5.6) . This indicates that multiple scattering is primarily generated by structures that are not smaller than about half of the dominant wavelength of the lower central frequency (0.5 Hz). For a crustal S velocity of 3.7 km s$^{-1}$ this corresponds to a minimum size defined by about 4 km. The mean free path value was in the range of 0.1 - 0.2 km, which is a value proportionate to the distance between the heterogeneities. However, this cannot be used to determine the absolute distance value, because the mean free path is also a function of the elastic properties (Sato et al., 2012). These observations strongly suggest that higher order free-surface multiples or internal scattering play an important role in this particular field setting. This may explain why full-field MDD appears to be more effective in estimating primary reflections than crosscorrelation.

One of the elastodynamic modeling experiments we conducted served to resemble the field data recording: this configuration entailed only two earthquakes and an interreceiver spacing of 7 km. The result we obtained by full-field MDD from this synthetic data set showed that it is possible to obtain reflections of prime features of the model (Figure 5.11b), although they are difficult to discern from artefacts. The other synthetic experiments served to discover which strategy is most effective to improve the MDD results. This revealed that having a dense receiver array with an interreceiver spacing of 1 km can give acceptable results even when we have only two earthquake recordings. In fact, having more earthquake recordings available did not improve the results as much as we expected. The synthetic result in Figure 5.11a tells us that a denser array could have resulted in substantial improvements of the field data results we showed in Figure 5.4. This is because more receivers simply record a larger number of the limited stationary phases. Besides, as the spectrum plots in Figures 5.1b and 5.2b show, a smaller receiver spacing would also have allowed us to work with a considerable larger portion of frequencies provided by the data set.

Regularity of the receiver positioning is very important for the processing of the data. For instance, when selecting the direct P- and S-waves, a regular spacing would have obviated the need to select trace by trace. Instead, it would be possible to select the direct waves by constructing a hyperbola which requires only the selection of the apex and a second random data point of the direct wave. Regular spacing also ensures that the virtual reflection responses form a suitable input for exploration scale imaging algorithms such as PSDM as we demonstrated with the synthetic example in Figures 5.13 and 5.14.

Another possible way to improve SI results with real data concerns the dimensionality of the array. This array formed a 2D line and therefore imposes the assumption that the variations in the medium perpendicular to the line are negligible with respect to the medium variations along the line. Considering the complex geology of this area, this is a very strong assumption. Therefore, it is likely that out of plane reflections get retrieved, which are impossible to migrate to the correct location. When a regular 3D surface array would be employed, the 2D assumption on the structure can be relieved. This would respect the 3D nature of any geological setting and allow for 3D migration of the reflections. Moreover, it would ensure that significanly more stationary phases can be correctly sampled and that a larger number of hypocenters are in stationary phase with the array.

## 5.7. CONCLUSION

We applied crosscorrelation and full-field multidimensional deconvolution (MDD) to the recordings of two earthquakes from the array in Peloponnesus, Greece of the MEDUSA experiment. The NMO-corrected stacked section of the full-field MDD results indicated continuous features that could be estimated reflections of structures in the subsurface. These features were hardly visible in the crosscorrelation result, that appeared to be more affected by artefacts. Our elastodynamic experiments indicate that a denser array could significantly improve the visibility and reliability of reflections obtained with both the full-field MDD and crosscorrelation method.

**5**

# 6

## CONCLUSION

The aim of this work was to make more optimal use of scattering coda from local earthquakes to obtain a detailed and reliable reflectivity image of the lithosphere. Classic seismic interferometry (SI) methods are negatively affected by conditions such as sparse source illumination, complex varying source mechanisms and multiple scattering inside the medium. Since these conditions are typical of field data settings, I propose an alternative SI method by multidimensional deconvolution (MDD) that proves to be more resilient under these conditions: full-field MDD for two-way wavefields. The main advantage of this method over other MDD methods is that the kernel of its governing Fredholm integral is exact. This characteristic makes this method ideal for effectively utilizing the spectral information encoded in scattering coda without being negatively affected by the complexities induced by multiple scattering.

Similar to other MDD methods, full-field MDD proves insensitive to variations in the source mechanisms or irregular source distributions. However, where ballistic MDD only uses first-order free-surface multiples that are induced by the ballistic field to construct primaries, full-field MDD utilizes free-surface multiples of all available orders to obtain a wider range of reflection angles of the primaries. This is a direct result of the fact that the kernel of the govering Fredholm equation is exact in the case of full-field MDD, while it requires to be approximated by the ballistic field in the case of ballistic MDD. The numerical simulation showed that full-field MDD is more resilient in the case of limited illumination conditions, because it makes effective use of the scattering coda. This also makes it possible for the method to correct for illumination irregularities that characterize the scattered wavefield.

The elastodynamic numerical experiments yielded input recordings that contained surface waves. The formulation for two-way wavefields obviates the necessity to remove surface waves and decompose into up- and down-components prior to application. The numerical results showed that full-field MDD for two-way wavefields removes surface waves inherently and yields a reflection response that only contains body-wave primaries. This is in accordance with the full-field MDD theory that shows the reflection response is obtained of the reference medium that has absorbing boundary conditions where the actual medium has a free surface.

This work revealed that there exists a trade-off between the scattering potential of the medium and the efficiency of SI methods to obtain virtual reflections from scattering-induced illumination only. Multiple scattering has a general positive effect on SI methods under limited illumination conditions. The scatterers act as secondary sources that compensate the illumination gaps. However, for the MDD methods multiple scattering has a negative implication: the direct wavefield estimation of the recording without free-surface multiples becomes less reliable with increasing scattering potential. This proved to be especially problematic for ballistic MDD.

**6**

Furthermore, the results showed that scattering leads to the increase in artefacts that affected one SI method more than the other. Scatterers generate complex radiation patterns that interact with each other to produce an even more complex wavefield that imprints the radiation patterns of the virtual sources. Crosscorrelation cannot correct for this scattering-induced imprint. Ballistic MDD only corrects for irregular illumination that originates from the passive sources. Though ANSI-MDD (the MDD method adapted for ambient-noise SI) is theoretically able to correct for scattering-induced irregularities, the results did not show a significant improvement with respect to crosscorrelation The negative impact of scattering was considerably less visible in the full-field MDD results, because the full-field point-spread function (PSF) effectively balances the scattering-induced anisotropic illumination. This makes full-field MDD more appropriate for high-resolution lithospheric imaging, because the Earth's lithosphere is a strongly scattering medium.

In the light of the complex relation between multiple scattering and the performance of SI methods, I proposed to apply a prior frequency-dependent scattering analysis of the data. By varying the frequency band of the recording it is possible to estimate the average dimension of the heterogeneities that generate the scattering coda. Moreover, by fitting the diffusion equation an estimate of the scattering mean free path of the medium can be estimated as well. This information not only sheds more light on the average scattering properties of the medium, it may also serve as a quality control to determine which SI method is appropriate for the imaging target.

The numerical tests proved the suitability of full-field MDD for real data applications. Therefore, I finalized this work by comparing the performance of full-field MDD to that of crosscorrelation using field data. For this I used the recordings from two earthquakes from a line-array in Peloponnesus, Greece, that was acquired during the Multi-disciplinary Experiments for Dynamic Understanding of Subduction under the Aegean Sea (MEDUSA). The virtual reflection estimates and the NMO-corrected stacked section obtained by full-field MDD indicated continuous features that were barely visible in the corresponding crosscorrelation results. This field data experiment confirms the resilience of the full-field MDD method under realistic field data conditions.

Full-field MDD is resilient under many realistic and challenging conditions. However, I want to emphasize that the governing equation does still pose an ill-posed inverse problem, considering Fredholm integrals of the first kind are per definition ill-posed. The fact that the kernel is exact in the case of full-field MDD is very important, however the term outside of the integral is not exact because it requires the wavefield recording without free-surface multiples. There are ways to improve the inversion. I expect that this is one of the possibilities to improve the performance of full-field MDD. Moreover, in this work I purposefully avoided the application of wavefield decomposition to ensure the methods suitability for application using sparse arrays. However, when receiver spacing is regular and dense, elastodynamic wavefield decomposition can improve the elastodynamic estimate of the earthquake recording without free-surface multiples considerably.

**6**

# ACKNOWLEDGEMENTS

This thesis would not have been possible if I hadn't been surrounded by some inspiring people.

First of all, I want to thank my promotor Kees Wapenaar for welcoming me into his research group. From the beginning onwards, you gave me a lot of freedom in defining my research direction, which allowed me the necessary space to develop a helicopter view of geophysical imaging and motivated me to become independent. I am very grateful that you always kept an open mind with respect to the research directions I chose, while at the same time your prompt and thorough feedback and our in-depth discussions helped me substantiate those choices by the academic standard.

I am very grateful to Carlos Almagro Vidal for helping me improve my understanding of the physics, mathematics and implementation of multidimensional deconvolution and the many other geophysical subjects we thoroughly discussed. Moreover, you helped me get started with the practical use of reciprocity theorems to develop new methods customized for the problem at hand. Without it, I would not have been able to experience the thrill of developing the full-field MDD method for two-way wavefields.

Once again united with Niels Grobbe and Evert Slob, we embarked on the exciting and fulfilling challenge of developing an online course with the purpose to prepare upcoming Applied Geophysics master students. I very much enjoyed working together with you again, and with the efforts and enthusiasm of Myrna Staring, Ranjani Shamasundar and Christian Reinicke Urruticoechea, we managed to bring the course up and running.

Jan Thorbecke, thank you for helping me use your code `fdelmodc` independently. My research would not have been possible without it. I was very happy to see it was possible to implement the double-couples. Moreover, the snapshot function allows us to contemplate the beauty of this science, which is necessary once in a while.

I express my gratitude to Kasper van Wijk for taking the time and effort to help me with the real data application while he was visiting our group in Delft. Not only did I learn how to efficiently obtain and process seismic data from all over the world, I also learned a great deal about the complex geophysical challenges that New Zealand is faced with.

I am grateful for the many golden tips from and insightful discussions with Boris

101

# LIST OF PUBLICATIONS

1. **I. E. Hartstra, C. Almagro Vidal and K. Wapenaar**, *Full-field multidimensional deconvolution to retrieve body-wave reflections from sparse passive sources*, Geophysical Journal International, **210**, 2 (2017).

2. **I. E. Hartstra, C. Almagro Vidal and K. Wapenaar**, *Retrieval of elastodynamic reflections from passive double-couple recordings*, Journal of Geophysical Research: Solid Earth, **123**, 4 (2018).

# BIBLIOGRAPHY

Aki, K. & Richards, P. G., 2002. *Quantative Seismology*, University Science Books, 2nd edn.

Almagro Vidal, C., 2017. *Passive seismic interferometry for reflection imaging and monitoring*, Ph.D. thesis, Delft University of Technology.

Almagro Vidal, C., Draganov, D., van der Neut, J., Drijkoningen, G., & Wapenaar, K., 2014. Retrieval of reflections from ambient noise using illumination diagnosis, *Geophysical Journal International*, **198**(3), 1572–1584.

Arfken, G. B. & Weber, H. J., 2005. *Mathematical Methods for Physicists*, Elsevier, 6th edn.

Baskir, E. & Weller, C. E., 1975. Sourceless reflection seismic exploration, *Geophysics*, **40**, 158–159.

Berkhout, A. J., 1982. *Seismic migration: Imaging of acoustic energy by wave field extrapolation*, Elsevier.

Bostock, M., Rondenay, S., & Shragge, J., 2001. Multiparameter two-dimensional inversion of scattered teleseismic body waves 1. Theory for oblique incidence, *Journal of Geophysical Research: Solid Earth*, **106**(B12), 30771–30782.

Boué, P., Poli, P., Campillo, M., & Roux, P., 2014. Reverberations, coda waves and ambient noise: Correlations at the global scale and retrieval of the deep phases, *Earth and Planetary Science Letters*, **391**, 137–145.

Campillo, M., 2006. Phase and correlation in random seismic fields and the reconstruction of the Green function, *Pure and Applied Geophysics*, **163**, 475–502.

Campillo, M. & Paul, A., 2003. Long-range correlations in the diffuse seismic coda, *Science*, **299**(5606), 547–549.

Chen, C., Zhao, D., & Wu, S., 2015. Tomographic imaging of the Cascadia subduction zone: Constraints on the Juan de Fuca slab, *Tectonophysics*, **647**, 73–88.

Claerbout, J. F., 1968. Synthesis of a layered medium from its acoustic transmission response, *Geophysics*, **33**(2), 264–269.

Curtis, A. & Halliday, D., 2010. Directional balancing for seismic and general wavefield interferometry, *Geophysics*, **75**(1), SA1–SA14.

Curtis, A., Nicolson, H., Halliday, D., Trampert, J., & Baptie, B., 2009. Virtual seismometers in the subsurface of the Earth from seismic interferometry, *Nature Geoscience*, **2**, 700–704.

de Hoop, A. T., 1995. *Handbook of radiation and scattering of waves*, Academic Press, 1st edn.

Derode, A., Larose, E., Tanter, M., De Rosny, J., Tourin, A., Campillo, M., & Fink, M., 2003. Recovering the Green's function from field-field correlations in an open scattering medium (L), *The Journal of the Acoustical Society of America*, **113**(6), 2973–2976.

Draganov, D., Wapenaar, K., & Thorbecke, J., 2006. Seismic interferometry: reconstructing the Earth's reflection response, *Geophysics*, **71**(4), SI61–SI70.

Draganov, D., Wapenaar, K., Mulder, W., Singer, J., & Verdel, A., 2007. Retrieval of reflections from seismic background-noise measurements, *Geophysical Research Letters*, **34**(4).

Dziewonski, A. M. & Anderson, D. L., 1981. Preliminary reference earth model, *Physics of the Earth and Planetary Interiors*, **25**(4), 297 – 356.

Fichtner, A., Kennett, B. L., Igel, H., & Bunge, H.-P., 2010. Full waveform tomography for radially anisotropic structure: new insights into present and past states of the Australasian upper mantle, *Earth and Planetary Science Letters*, **290**(3-4), 270–280.

Fichtner, A., Stehly, L., Ermert, L., & Boehm, C., 2017. Generalized interferometry–i: theory for interstation correlations, *Geophysical Journal International*, **208**(2), 603–638.

Fokkema, J. T. & van den Berg, P., 1993. *Seismic applications of acoustic reciprocity*, Elsevier.

Fowler, C. M. R., 2005. *The Solid Earth: An Introduction to Global Geophysics*, Cambridge University Press, 2nd edn.

Haney, M. M., van Wijk, K., & Snieder, R., 2005. Radiative transfer in layered media and its connection to the O'Doherty-Anstey formula, *Geophysics*, **70**(1), T1–T11.

Hartstra, I. & Wapenaar, K., 2015. A method to retrieve an improved high resolution reflection response from HiCLIMB array recordings of local earthquake scattering coda, *26th IUGG General Assembly, Prague*.

Hartstra, I. E., Almagro Vidal, C., & Wapenaar, K., 2017. Full-field multidimensional deconvolution to retrieve body-wave reflections from sparse passive sources, *Geophysical Journal International*, **210**(2), 609–620.

Hartstra, I. E., Almagro Vidal, C., & Wapenaar, K., 2018. Retrieval of elastodynamic reflections from passive double-couple recordings, *Journal of Geophysical Research: Solid Earth*, **123**(4), 3197–3207.

Kennett, B. L. N., 1998. *Seismic wave propagation and seismic tomography*, Research School of Earth Sciences, Australian National University.

Kokinou, E., Kamberis, E., Vafidis, A., Monopolis, D., Ananiadis, G., & Zelilidis, A., 2005. Deep seismic reflection data from offshore western Greece: a new crustal model for the Ionian Sea, *Journal of Petroleum Geology*, **28**(2), 185–202.

Larose, E., Derode, A., Campillo, M., & Fink, M., 2004a. Imaging from one-bit correlations of wideband diffuse wave fields, *Journal of Applied Physics*, **95**(12), 8393–8399.

Larose, E., Margerin, L., van Tiggelen, B., & Campillo, M., 2004b. Weak localization of seismic waves, *Physical review letters*, **93**(4), 048501.

Larose, E., Margerin, L., van Tiggelen, B., Campillo, M., Shapiro, M., A., P., Stehly, L., & Tanter, M., 2006. Correlation of random wavefields: An interdisciplinary review, *Geophysics*, **71**, SI11–SI21.

Lin, F.-C., Tsai, V., Schmandt, B., Duputel, Z., & Zhan, Z., 2013. Extracting seismic core phases with array interferometry, *Geophysical Research Letters*, **40**, 1–5.

Lobkis, O. I. & Weaver, R. L., 2001. On the emergence of the green's function in the correlations of a diffuse field, *The Journal of the Acoustical Society of America*, **110**(6), 3011–3017.

Malcolm, A. E., Scales, J. A., & van Tiggelen, B. A., 2004. Extracting the Green function from diffuse, equipartitioned waves, *Physical Review E*, **70**, 015601(R).

McKenzie, D., 1978. Active tectonics of the Alpine—Himalayan belt: the Aegean Sea and surrounding regions, *Geophysical Journal International*, **55**(1), 217–254.

Nakata, N., Snieder, R., & Behm, M., 2014. Body-wave interferometry using regional earthquakes with multidimensional deconvolution after wavefield decomposition at free surface, *Geophysical Journal International*, **199**(2), 1125–1137.

Nishida, K., 2013. Global propagation of body waves revealed by cross-correlation analysis of seismic hum, *Geophysical Research Letters*, **40**, 1–6.

Nishitsuji, Y., Minato, S., Boullenger, B., Gomez, M., Wapenaar, K., & Draganov, D., 2016. Crustal-scale reflection imaging and interpretation by passive seismic interferometry using local earthquakes, *Interpretation*, **4**(3), SJ29–SJ53.

Nolet, G., 2008. *A Breviary of Seismic Tomography: Imaging the Interior of the Earth and Sun*, Cambridge University Press.

Paasschens, J. C. J., 1997. Solution of the time-dependent boltzmann equation, *Physical Review E*, **56**(1), 1135–1140.

Papazachos, B. C., Karakostas, V. G., Papazachos, C. B., & Scordilis, E. M., 2000. The geometry of the Wadati–Benioff zone and lithospheric kinematics in the Hellenic arc, *Tectonophysics*, **319**(4), 275–300.

Poli, P., Pedersen, H. A., & Campillo, M., 2012. Emergence of body waves from cross-correlation of short period seismic noise, *Geophysical Journal International*, **188**(2), 549–558.

Ravasi, M., Meles, G., Curtis, A., Rawlinson, Z., & Yikuo, L., 2015. Seismic interferometry by multidimensional deconvolution without wavefield separation, *Geophysical Journal International*, **202**(1), 1–16.

Roux, P., Sabra, K. G., Gerstoft, P., & Kuperman, W. A., 2005. P-waves from cross-correlation of seismic noise, *Geophysical Research Letters*, **32**(L19303), 2–4.

Ruigrok, E., 2012. *Body-wave seismic interferometry applied to earthquake- and storm-induced wavefields*, Ph.D. thesis, Delft University of Technology.

Ruigrok, E., Campman, X., & Wapenaar, K., 2011. Extraction of p-wave reflections from microseisms, *Comptes Rendus Geoscience*, **343**, 512–525.

Sabra, K. G., Gerstoft, P., Roux, P., Kuperman, W. A., & Fehler, M. C., 2005. Surface wave tomography from microseisms in southern california, *Geophysical Research Letters*, **32**(14).

Sato, H., Fehler, M. C., & Maeda, T., 2012. *Seismic wave propagation and scattering in the heterogeneous Earth*, Springer, 2nd edn.

Schuster, G. T., 2001. Theory of daylight/interferometric imaging-tutorial, in *63rd EAGE Conference & Exhibition*.

Schuster, G. T., 2009. *Seismic interferometry*, Cambridge University Press Cambridge, 1st edn.

Snieder, R., 2002. Coda wave interferometry and the equilibration of energy in elastic media, *Physical review E*, **66**(4), 046615.

Snieder, R., 2004. Extracting the Green's function from the correlation of coda waves: A derivation based on stationary phase, *Physical Review E*, **69**(4), 046610.

Stehly, L., Campillo, M., & Shapiro, N., 2006. A study of the seismic noise from its long-range correlation properties, *Journal of Geophysical Research: Solid Earth*, **111**(B10).

Stein, S. & Wysession, M., 2003. *An introduction to Seismology, Earthquakes, and Earth Structure*, Blackwell Publishing.

Suckale, J., Rondenay, S., Sachpazi, M., Charalampakis, M., Hosa, A., & Royden, L., 2009. High-resolution seismic imaging of the western hellenic subduction zone using teleseismic scattered waves, *Geophysical Journal International*, **178**(2), 775–791.

Thorbecke, J. W. & Draganov, D., 2011. Finite-difference modeling experiments for seismic interferometry, *Geophysics*, **76**, H1–H18.

Tonegawa, T., Nishida, K., Watanabe, T., & Shiomi, K., 2009. Seismic interferometry of teleseismic S-wave coda for retrieval of body waves: an application to the Philippine sea slab underneath the Japanese Islands, *Geophysical Journal International*, **178**, 1574–1586.

Tsokas, G. N. & Hansen, R. O., 1997. Study of the crustal thickness and the subducting lithosphere in Greece from gravity data, *Journal of Geophysical Research: Solid Earth*, **102**(B9), 20585–20597.

van der Neut, J., 2012. *Interferometric redatuming by multidimensional deconvolution*, Ph.D. thesis, Delft University of Technology.

van der Neut, J. & Herrmann, F. J., 2013. Interferometric redatuming by sparse inversion, *Geophysical Journal International*, **192**, 666–670.

van der Neut, J., Ruigrok, E., Draganov, D., & Wapenaar, K., 2010. Retrieving the earth's reflection response by multi-dimensional deconvolution of ambient seismic noise, in *72nd EAGE Conference and Exhibition incorporating SPE EUROPEC 2010*.

van der Neut, J., Tatanova, M., Thorbecke, J., Slob, E., & Wapenaar, K., 2011. Deghosting, demultiple, and deblurring in controlled-source seismic interferometry, *International Journal of Geophysics*, **2011**.

van Tiggelen, B., 2003. Green function retrieval and time reversal in a disordered world, *Physical Review Letters*, **91**(24), 243904.

Wapenaar, K., 1996. One-way representations of seismic data, *Geophysical Journal International*, **127**, 178–188.

Wapenaar, K., 2004. Retrieving the elastodynamic Green's function of an arbitrary inhomogeneous medium by cross correlation, *Physical Review Letters*, **93**(25), 254301.

Wapenaar, K. & Fokkema, J., 2006. Green's function representations for seismic interferometry, *Geophysics*, **71**, SI33–SI46.

Wapenaar, K., Slob, E., & Snieder, R., 2008a. Seismic and electromagnetic controlled-source interferometry in dissipative media, *Geophysical Prospecting*, **56**(3), 419–434.

Wapenaar, K., van der Neut, J., & Ruigrok, E., 2008b. Passive seismic interferometry by multidimensional deconvolution, *Geophysics*, **73**(6), A51–A56.

Wapenaar, K., van der Neut, J., Ruigrok, E., Draganov, D., Hunziker, J., Slob, E., Thorbecke, J., & Snieder, R., 2011. Seismic interferometry by crosscorrelation and by multidimensional deconvolution: a systematic comparison, *Geophysical Journal International*, **185**, 1335–1364.

Wegler, U., Korn, M., & Przybilla, J., 2006. Modeling full seismogram envelopes using radiative transfer theory with Born scattering coefficients, *Pure and Applied Geophysics*, **163**(2), 503–531.

Wu, R.-S. & Aki, K., 1985. Scattering characteristics of elastic waves by an elastic heterogeneity, *Geophysics*, **50**(4), 582–595.

Zhan, Z., Ni, S., Helmberger, D. V., & Clayton, R. W., 2010. Retrieval of moho-reflected shear wave arrivals from ambient seismic noise, *Geophysical Journal International*, **182**(1), 408–420.